Probing Biological Systems using Reflectance and Fluorescence Spectroscopy

by

Malavika Chandra

A dissertation submitted in partial fulfillment
of the requirements for the degree of
Doctor of Philosophy
(Applied Physics)
in The University of Michigan
2010

Doctoral Committee:

Professor Mary-Ann Mycek, Chair
Professor Stephen E. Feinberg
Professor Michael. D. Morris
Professor James M. Scheiman

Acknowledgements

There are many people who have provided guidance and support to me throughout my dissertation work and I would like to thank them all.

I thank my dissertation advisor Prof. Mary-Ann Mycek for all her guidance, encouragement, and understanding throughout my dissertation work. I am also grateful for the opportunity of independent thinking that she encouraged. I am a better researcher because of her.

I am thankful to Prof. Jim Scheiman for his guidance and many helpful discussions during the pancreas project. It has been a pleasure working with him and learning the ropes of working in a clinical setting. I thank Prof. Stephen Feinberg for bringing us on board to collaborate with him and for all his guidance during the EVPOME project. I would also like to thank Prof. Michael Morris for his very helpful advice during my preliminary exam and for being on my dissertation committee.

This dissertation has been the result of a truly collaborative effort. I am thankful to Dr. Diane Simeone for her help and guidance with the pancreas project and for helping with many of the logistic issues of acquiring clinical data along with Prof. Scheiman. I am also thankful to her and Dr. David Heidt for providing us with the mouse xenografts for the pancreas project. Thank you to Dr Barbara McKenna, and Dr. Julianne Purdy for their continued help and inputs in the pancreas project and for all their help and patience with the data collection during surgery. The clinical data collection would not have been

possible without the consent of the patients and I thank them sincerely. I am also thankful to Jes Pedroza, Nalina Singh, and Sheryl Korsnes who helped us get patient consent.

I am thankful to Pascal Rousseau for all his help with the instrumentation. I learned a lot from him. I would also like to thank Dr. Kenji Izumi and Wen-Liang Lo from Prof. Feinberg's lab for providing the EVPOME specimens and for the helpful discussions. Thank you to Dr. Elly Liao and Prof. Hollister for their collaboration and for providing us with articular cartilage samples.

I thank my past and present lab mates: Dr. Karthik Vishwanath, Dr. Wei Zhong, Dr. Dhruv Sud, Dr. Ching-Wei Chang, Robert Wilson, Viola Schweller, and Bill Lloyd for their help and many useful discussions over the years.

I am also thankful to the funding sources that made this dissertation work possible: the National Institutes of Health, the National Pancreas Foundation, the Wallace H. Coulter Foundation, the U of M Comprehensive Cancer Center, and the U of M Medical School Translational Research Program.

I have been fortunate to have made some great friends at Michigan that made my years here memorable and even the Michigan winters enjoyable. Cynthia McNabb and Charles Sutton in the Applied Physics office have always been very helpful and supportive. I thank them for making me feel very welcome and for making life so much simpler and easier in my graduate years. I thank my friends from Applied Physics: Dr. Kevin Haworth, Dr. Brenton Knuffman, Eric Harding, Dr. Arthur McClelland, and Erik Kim for making my first years in graduate school and in this country memorable. Many thanks to my Food Fun group and my friends from the Indian Classical Music and Dance group. A

special thank you to Dr. Shivani Ahuja and Raman Ramani Kalyan for always being there and for all their support.

Finally, I am thankful to all of my family and I dedicate this work to them. Each one of them has had a hand in helping me achieve my goals. Thank you to Amma, Nani, Mamma, Papa, and my brother for all their years of love, support, and encouragement. Thank you also to Aai and Baba for their blessings and support of my work. Last but definitely not the least; I thank my husband Aniket for his love and for his support through all my craziness during my dissertation work.

Table of Contents

List of Figures

List of Tables

Abstract

Pancreatic adenocarcinoma is a leading cause of cancer death with a five-year survival rate of only 5%. Endoscopic ultrasound-guided fine-needle aspiration (EUS-FNA), the current diagnostic standard, cannot reliably rule out malignancy and is insensitive to distinguishing adenocarcinoma from chronic pancreatitis (inflammation). To investigate the ability of multi-modal optical spectroscopy to detect signals from human pancreatic tissue, a clinically-compatible instrument was developed for rapid, quantitative reflectance and fluorescence spectroscopy in tissues, including fluorescence lifetime sensing. Reflectance and fluorescence spectra and time-resolved fluorescence decay curves were successfully measured for the first time from freshly excised human pancreatic tissues and *in vivo* human pancreatic cancer xenografts in mice.

For the first time, pancreatic tissue classification algorithms using optical spectroscopy data were developed. A total of 96 fluorescence and 96 reflectance spectra were considered from 50 sites (adenocarcinoma, chronic pancreatitis, and normal tissues) on 9 patients. The SpARC (Spectral Areas and Ratios Classifier) and PCA (principal component analysis) algorithms employed linear discriminant analysis on classification variables extracted from optical data. Maximum sensitivity, specificity, NPV, and PPV (85%, 89%, 92%, and 80%, respectively for the SpARC, and 91%, 90%, 95%, 83%, respectively for the PCA algorithm) for correctly identifying adenocarcinoma were achieved employing both reflectance and fluorescence spectra. Inclusion of time-resolved fluorescence data in the PCA algorithm further improved the distinction between

pancreatitis and normal tissues in a limited data set. Importantly, the sensitivity of both algorithms far exceeds reported EUS-FNA sensitivity (54%) at distinguishing adenocarcinoma from chronic pancreatitis. The developed algorithms show promise for rapid automated pancreatic tissue classification using multi-modal optical spectroscopy and could be employed in a clinical setting.

The possibility of applying optical spectroscopy to evaluate tissue engineered devices was also investigated. Tissue engineered constructs are functional biologic devices employed for grafting wounds or replacing diseased tissue. Non-invasive methods are required to assess the viability of these engineered constructs. Monte Carlo simulations and multi-modal optical spectroscopy were coupled to assess porcine articular cartilage and oral mucosa constructs for the first time. The developed methods would be safe for clinical human use as they employ endogenous contrast for non-invasive quantitative assessment.

Chapter 1
Introduction

1.1 Optical spectroscopy for biological sensing

The interaction of light with complex, inhomogeneous media such as biological tissue is characterized by a variety of processes that depend on the physical nature of the light and the specific morphology and composition of the tissue [1, 2]. Incident light may be scattered (elastically or inelastically) multiple times due to microscopic differences in the index of refraction within the tissue, it may be absorbed by fluorophores (e.g. cellular NAD(P)H or FAD and extracellular collagen), which may then release their excess energy by radiative decay, producing fluorescence or be non-radiatively absorbed by chromophores present in the medium [3-5]. The remitted fluorescent light may, in turn, be multiply scattered or absorbed. The, reflected and fluorescent light reaching the tissue surface is affected by scattering (e.g., from inhomogeneities including extracellular matrix and membranes and intracellular nuclei and mitochondria) and absorption (e.g., from hemoglobin and proteins) properties of the tissue.

Methods of optical spectroscopy and imaging are being developed for a variety of biomedical applications in non- or minimally-invasive tissue diagnostics, including sensing molecular concentrations of delivered pharmaceutical or contrast agents, probing tissue physiologic status, and detecting early stages of disease *in vitro* and *in vivo* [2-10]. The work in this dissertation applies reflectance and fluorescence spectroscopy for the

assessment of biological tissues without the use of contrast agents. The remaining text of this chapter introduces these modalities of optical spectroscopy, motivates the optical assessment of biological tissue studied in this dissertation, lists the specific aims of the dissertation, and concludes with an outline for the remaining thesis.

Spectral (steady-state) detection of fluorescence emission resolves the variation of fluorescence intensity with wavelength of emitted light [11]. Endogenous tissue fluorescence non-invasively provides information about the native biochemical composition and microenvironment in living tissues without the use of exogenous contrast agents [8-10]. Endogenous fluorescence spectra recorded from biological systems like cells and tissues are composed of spectral bands from multiple constituent fluorophores, including extracellular structural proteins (such as collagen and elastin) and intracellular metabolic co-factors (NAD(P)H and FAD) [9]. Fluorescence intensities are sensitive to factors including variations in excitation intensity, fluorophore concentration, photobleaching, and sources of optical loss (absorption and scattering) in biological systems [11, 12]. To gain diagnostic value, these complex spectra are analyzed chemometrically or modeled computationally [4, 7, 13-23].

Time-resolved fluorescence techniques capture the transient decay of the fluorescence intensity in time. This decay reflects the relative concentrations and the excited-state lifetimes of the endogenous fluorophores contributing to the emission [11]. Fluorophore lifetimes are sensitive to the local biochemical environment and vary with pH and oxygenation [11]. However, time-resolved measurements do not vary with fluorescence intensity because they are generally independent of artifacts influencing fluorescence steady-state measurements. This is important when applying fluorescence spectroscopy *in*

vivo, since intensity losses seen in the steady-state emission spectrum due to absorption of light by hemoglobin in tissue would not affect time-resolved measurements [24, 25].

Reflectance spectroscopy relies upon the absorption and elastic scattering of light in tissues, which depend on tissue composition (e.g., oxy- vs. deoxy-hemoglobin content) and index of refraction variations (e.g., cell nuclei size, shape, and density), respectively. Reflectance methods have been employed to distinguish neoplastic from normal epithelial tissues in the colon [26] and in studies of Barrett's esophagus [27], as well as to characterize tissues in solid organs, such as the breast [28].

These different measurement modalities (steady-state fluorescence, time-resolved fluorescence, and reflectance spectroscopy) can thus provide complimentary information about biological tissue. For example, studies in the breast, which is a solid organ like the pancreas, have demonstrated improved diagnostic discrimination of inflammatory and malignant breast tissues *ex vivo* via the use of a multi-modal approach involving both fluorescence and reflectance studies [21].

In this dissertation work, instrumentation for reflectance and fluorescence spectroscopy, including lifetime sensing, was developed and applied to non-invasively study natural pancreatic tissues, porcine articular cartilage, and engineered oral mucosa.

1.2 Motivation

1.2.1 Pancreatic Adenocarcinoma

Pancreatic adenocarcinoma has a five-year survival rate of only 5%, making it the fourth-leading cause of cancer death in the United States [29]. Current diagnostic procedures are unable to diagnose the disease in its early stages [30]. In various imaging modalities,

diagnosis is compromised due to similarities in the appearance of chronic pancreatitis (inflammation of the pancreas) and adenocarcinoma [30]. Endoscopic ultrasound-guided fine needle aspiration (EUS-FNA) is the current clinical standard for the diagnosis of pancreatic adenocarcinoma. In EUS-FNA, ultrasound is employed to guide a hollow needle through an endoscope into the suspected pancreatic mass. Cells from the suspected mass are sampled via the needle and analyzed by a cytopathologist for malignancy. Small specimen size, overlap with chronic pancreatitis in the diagnostic features seen at cytological evaluation, and EUS-FNA operator dependence make this technique inconsistent in its performance at detecting pancreatic cancer. This is apparent from the wide range of sensitivities (54 – 95%), specificities (71- 100%), and negative predictive values (NPVs) (16-92%) of adenocarcinoma detection reported for this method (Figure 1.1a) in a recent meta-analysis of 28 EUS-FNA studies [30]. In particular, EUS-FNA has only 54% sensitivity (Figure 1.1b) for adenocarcinoma in the setting of chronic pancreatitis (i.e. when the patient has both adenocarcinoma and chronic pancreatitis) [31] and the two conditions frequently coexist. The exceedingly large range (16-92%), and low median (72%) of the NPV indicated the inability of EUS-FNA to definitively rule-out malignancy, thus leading to the conclusion that "preoperative biopsy of potentially resectable pancreatic tumors is not generally advisable, as malignancy cannot be ruled out with adequate reliability" [30]. A study found that as many as 9% of patients undergo complicated pancreatic surgery, only to reveal absence of malignancy during pathological examination of the resected specimen [32]. Clearly, detection of pancreatic adenocarcinoma in its early stages and its distinction from chronic pancreatitis could greatly improve the chances of patient survival.

Multiple studies have employed optical techniques for minimally invasive detection of breast, cervical, colon, and esophageal cancers, including [3, 4, 27, 33-36].

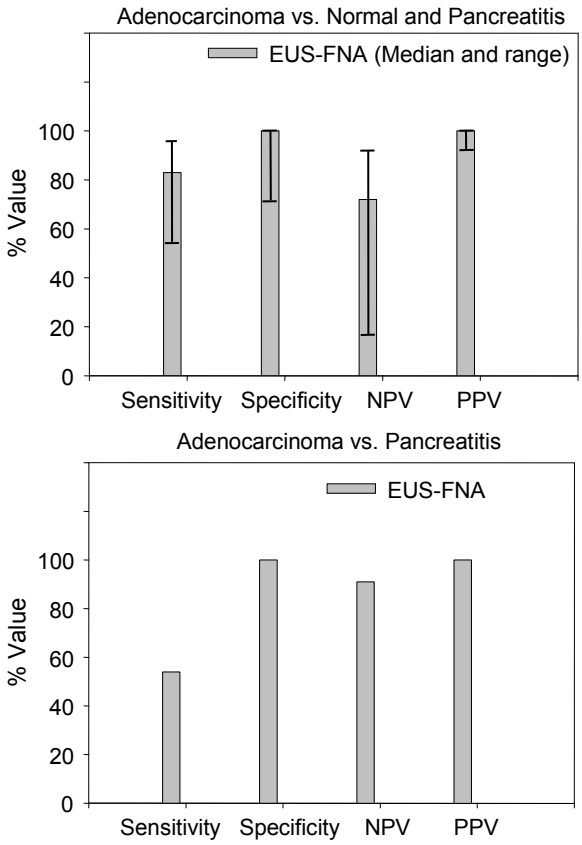

Figure 1.1 The median and range of sensitivity, specificity, NPV, and PPV for adenocarcinoma identification reported in a meta-analysis of 28 EUS-FNA studies [30]. (b) The performance of EUS-FNA for distinguishing between adenocarcinoma and chronic pancreatitis in the setting of chronic pancreatitis as reported in a study [31].

However, owing to the relative inaccessibility of the pancreas, only a handful of studies have applied optical methods for pancreatic cancer detection. Optical coherence tomography was applied to both *in vivo* and *ex vivo* detection of pancreatic cancer [37, 38] and near-infrared spectroscopy [39] was applied *ex vivo*. Pancreatic cancer cells on microscope slides were studied employing partial-wave microscopic spectroscopy [40]. A field effect hypothesis predicting changes in the duodenum owing to presence of cancer

in the pancreas [41, 42] was studied *ex vivo* using four-dimensional elastic light-scattering, and low-coherence enhanced backscattering spectroscopies.

The aim of the study reported here was to employ reflectance and fluorescence spectroscopy for differentiating between pancreatic adenocarcinoma, chronic pancreatitis, and normal pancreatic tissue. Tissue classification algorithms were developed to classify the measured optical spectroscopy data employing linear discriminant analysis and principal component analysis.

1.2.2 Non-invasive sensing of tissue engineered constructs

Tissue engineering is the process of creating functional biologic devices either for grafting wounds or for replacing diseased tissues. A significant challenge in tissue engineering is the non-invasive, quantitative assessment of the viability of these engineered tissue constructs, and how they compare to normal biologic tissue. At present, evaluation of soft tissue regeneration of engineered tissue constructs during the manufacturing process or post-implantation into patients is done mostly via histology. First, this approach is invasive and requires time-consuming sectioning of the tissue for staining to be performed. Second, histology is inherently qualitative since the stain color and intensity may not reflect the amount of matrix present in the soft tissue. Biochemical assays can also be employed to measure, for example, the level of glucose uptake from the cell culture media in which the tissue constructs are being grown [43]. While such a method could be non-invasive, quantitative, and able to assess overall cell viability, it cannot provide spatial information about the functionality of the construct. In addition, such a technique could not be employed post-implantation into patients.

Table 1.1. Methods to assess the viability of tissue engineered constructs

Histology	Biochemical Assays	Optical Methods
Destructive	Non-invasive	Non-invasive
Qualitative/ Subjective	Quantitative/ Objective	Quantitative/ Objective
Labor intensive	Real-time monitoring	Real-time monitoring
No spatial information	No spatial information	Spatial information
Invasive monitoring post-implantation into patients	No post-implantation assessment possible	Non-invasive monitoring post-implantation using endogenous contrast

An optical spectroscopy or optical imaging technique could non-invasively and quantitatively determine soft tissue composition or cellular function and would represent a significant advance in the assessment of engineered tissues. Since the method would be non-destructive, it would allow repeated assessment of a given sample over time, thereby significantly speeding up lengthy and expensive protocols requiring multiple samples. Furthermore, the method could provide spatial information about the biological viability of the construct via fiber optic probes both pre- and post- implantation into patients. Table 1.1 compares the present methods for assessing viability of tissue engineered constructs with the proposed optical methods.

In order to quantify optical measurements made in biological tissues, it is necessary to be able to describe accurately all light-tissue interactions (composed of elastic scattering of both incident and remitted light, as well as absorption of incident excitation by tissue chromophores or fluorophores). A widely used technique for quantitative simulations of light-tissue interactions involves the use of Monte Carlo (MC) models for photon transport in turbid media; an approach proven to provide accurate predictions of light

energy distribution in turbid media along with the ability to model complex tissue architectures and source-detector geometries [10, 44].

In this dissertation, reflectance and fluorescence spectroscopy and previously developed MC simulations were coupled towards the goal of assessing viability of two tissue engineered constructs namely, articular cartilage constructs, and oral mucosa constructs. A significant advantage of the methods employed in this work was the use of endogenous contrast for non-invasive quantitative assessment, thus ensuring safety for clinical human use.

1.2.2.1 Articular cartilage constructs

Hyaline articular cartilage (AC) is found in the synovial joints and is an important contributor to the functional capacities of these joints [45]. If a chondral defect or lesion occurs, it does not heal on its own. Thus methods are being developed to make tissue constructs that would mimic true AC. Pre- and post implantation non-invasive viability testing of these constructs can potentially be done by analyzing their optical signals. Here, we present a novel combination of experiment and computation to quantitatively characterize fresh porcine knee cartilage using endogenous fluorescence. Fluorescence data and simulations were used to extract a quantitative measure to monitor relative changes in concentration of the constituent fluorophores in AC tissue over time. The porcine articular cartilage (AC) tissue samples studied offered the biological variability not found in artificial tissue-simulating phantoms and will serve as a model for future optical molecular sensing studies on tissue engineered AC constructs intended for use in human therapy.

1.2.2.2 *Ex Vivo* Produced Oral Mucosa Equivalent (EVPOME) constructs

Oral surgeries or trauma in humans can result in open wounds that are susceptible to infections and require grafting by either skin or oral mucosa grafts from donor sites [43, 46]. The procedure however involves multiple surgeries and can result in donor site morbidity. In addition, non-oral mucosa grafts, such as skin, have different keratinization patterns. Tissue engineered *ex* vivo produced oral mucosa equivalent (EVPOME) constructs can be used to graft oral wounds. To manufacture these constructs, oral keratinocytes from the patient are suspended in an artificial, biologically compatible matrix at day 0 and the cell-matrix composite is grown to form the tissue construct, ready for implantation at day 11. Since the cells are obtained from the patient's own mouth, there is no risk of rejection by the patient's immune system or a difference in keratinization pattern. The EVPOME has been successfully tested in a Phase I human clinical trial.

Quantitative, non-invasive tools are required to monitor structure, composition, and function of these engineered tissues in real time. Non-invasive tools can be developed to assist in creating release criteria for the manufactured engineered tissues, *in vitro*, and for assessing tissue performance after their grafting, *in situ*.

In this dissertation work, non-invasive optical assessment of cell viability in EVPOME constructs by employing fluorescence spectroscopy via fiber optic probes was investigated. Measuring the fluorescence from the same healthy EVPOME construct under sterile conditions from day 0 to day 11 could be used for characterizing the fluorescence expected from a viable construct from day 0 to day 11. This information

could then be used to discard faulty constructs early on in the manufacturing process, thereby saving time and resources.

The use of a non-invasive quantitative optical technique could establish a release criteria of an engineered tissue in a more comprehensive fashion, i.e., viability, structure and metabolic activity, compared with presently used assay systems, such as glucose uptake. The development of release criteria in real time will improve the quality control of engineered tissues during their manufacturing process. The technique, once developed, will also allow the ability to assess tissue viability in situ, non-invasively, after grafting into animals and, eventually, into humans.

1.3 Dissertation objectives

Specific Aim 1: To design and develop instrumentation for reflectance and fluorescence spectroscopy. A clinically compatible instrument for rapid, quantitative optical sensing in biological tissues using reflectance and fluorescence spectroscopy, including fluorescence lifetime sensing will be developed.

Specific Aim 2: To assess the application of fluorescence and reflectance spectroscopy for differentiating between human pancreatic adenocarcinoma, chronic pancreatitis (inflammation of the pancreas), and normal pancreatic tissues. The developed clinical instrumentation will be employed, for the first time, to perform reflectance and fluorescence spectroscopies on human pancreatic xenografts in mice and from human pancreatic tissues. Chemometric tissue classification algorithms that employ principal component analysis (PCA) and linear discriminant analysis (LDA) will be

developed for the first time for pancreatic tissue classification using optical spectroscopy data.

Specific Aim 3: To assess the application of optical spectroscopy for non-invasive assessment of tissue engineered constructs. The developed clinical instrumentation and previously developed Monte Carlo (MC) codes of photon transport in turbid media will be employed for the first time to optically characterize porcine articular cartilage and *ex vivo* produced oral mucosa constructs (EVPOME) in a non-invasive and quantitative manner.

1.4 Dissertation overview

The dissertation has been organized as follows:

Chapter 2 introduces the theoretical concepts of fluorescence and reflectance spectroscopy and introduces Monte Carlo modeling of photon transport in turbid media.

Chapter 3 describes in detail the developed clinical instrumentation for reflectance and fluorescence spectroscopy, including lifetime sensing. The chapter includes the optical and electrical design of the instrument and describes the software developed for controlling the instrument. The chapter also describes the instrument calibration and data processing required after data acquisition.

Chapter 4 describes the application of the developed technology to the first *in vivo* measurements of fluorescence and reflectance spectra from human pancreatic cancer xenografts in NOD/SCID mice (non-obese diabetic/severe combined immunodeficiency). It also describes the first *ex vivo* measurements of fluorescence and reflectance spectra and fluorescence life-time decays from freshly excised human pancreatic tissue. A

correlation of the optical measurements with known histological features of normal, pancreatitis, and adenocarcinoma pancreatic tissues is described.

Chapter 5 describes the development of the first pancreatic tissue classification algorithms employing the measured optical data. Two tissue classification algorithms developed in this dissertation – SpARC (spectral areas and ratios classifier) algorithm and PCA (principal component analysis) algorithm - are described and their performance at classifying pancreatic tissue into normal, pancreatitis and adenocarcinoma tissue is presented.

Chapter 6 describes the application of the developed technology to the non-invasive assessment of tissue-engineered constructs. Optical spectroscopy measurements and Monte Carlo simulations are coupled for optimized non-invasive, quantitative assessment employing endogenous contrast. The first part of the chapter describes the first attempt of this kind for optical assessment of porcine articular cartilage (AC) tissue samples. These samples offer the biological variability not found in artificial tissue-simulating phantoms and serve as a model for future optical molecular sensing studies on tissue engineered AC constructs intended for use in human therapy.

The second part of the chapter describes the MC simulations and experiments undertaken to optimize the assessment of biological viability of tissue engineered *ex vivo* produced oral mucosa constructs (EVPOME). The first fluorescence spectroscopy measurements of EVPOME and its constituents are described. Also described is the first application of previously developed Monte Carlo codes to the quantitative simulation of photon transport in EVPOME constructs.

Chapter 7 summarizes and concludes the dissertation and discusses possible future work and potential applications of the work presented here.

Chapter 2
Theoretical Background

A background of the optical techniques employed in this dissertation work is presented in this chapter. Section 2.1 of this chapter introduces the theoretical concepts of reflectance and fluorescence spectroscopy, including time-resolved fluorescence spectroscopy. Section 2.2 briefly describes the previously developed Monte Carlo code of photon transport in turbid media.

2.1 Reflectance and Fluorescence spectroscopy

When photons impinge on biological tissue, they can undergo a variety of interactions [1, 2]. Incident photons could be scattered multiple times due to the mismatch of refractive indices, be absorbed by chromophores present in the medium (e.g. hemoglobin), or be absorbed by fluorophores, which may then release their excess energy by radiative decay, producing fluorescence. The remitted fluorescent light may, in turn, be scattered or absorbed multiple times.

Fluorescence and reflectance spectroscopies can provide complimentary information about biological tissue. Reflectance spectroscopy provides information primarily about tissue morphology (including the size and density of cell nuclei), while fluorescence reports mainly on tissue biochemistry (including intra- and extra-cellular endogenous fluorophores like NAD(P)H and collagen). These two spectroscopies may be performed

with thin, flexible, fiber-optic probes; the techniques are thus clinically feasible and allow access to internal organs endoscopically or during surgery [10, 25, 35, 47-49]. Fluorescence and reflectance spectroscopies have been applied in combination to detect oral cancer [50], breast cancer [3], dysplasia in Barrett's esophagus [27], and cervical cancer [22].

2.1.1 Steady-state reflectance spectroscopy

As light propagates in a turbid medium, it encounters optical in-homogeneities. Every time a refractive index mismatch occurs, light is scattered. If the scattered photon has the same energy as the incident photon then light is scattered elastically. Reflectance spectroscopy involves the detection of these elastically scattered photons. The propagation of elastically scattered (reflected) light is dependant on the characteristic features (e.g. size and density of scatterers) of the medium. Thus, reflectance spectroscopy can provide pathologically relevant information about living tissues, including tissue morphology, as well as the size, shape and, density of cells [2, 5]. Such information can help track architectural changes in tissue and has been employed to study dysplasia in living tissue [3, 4, 6, 7, 27, 51].

The instrumentation required for measuring steady-state reflectance spectra in a clinical setting typically consists of a light source that gives out white light, and optical fibers for delivering the light to the tissue specimen and collecting the scattered signal [27, 52]. A spectrograph is used to disperse the intensity spectrum into its various wavelength contributions and a charge-coupled device (CCD) camera is then used for detecting the signal. As the distance between the source and detector fibers is increased, the light scattered from deeper and deeper layers of the tissue can be detected.

Figure 2.1 plots a representative normalized reflectance spectrum measured from human pancreatic normal tissue (blue line) [6]. A reflectance spectrum is represented as a plot of intensity of reflected light, as a function of the wavelength.

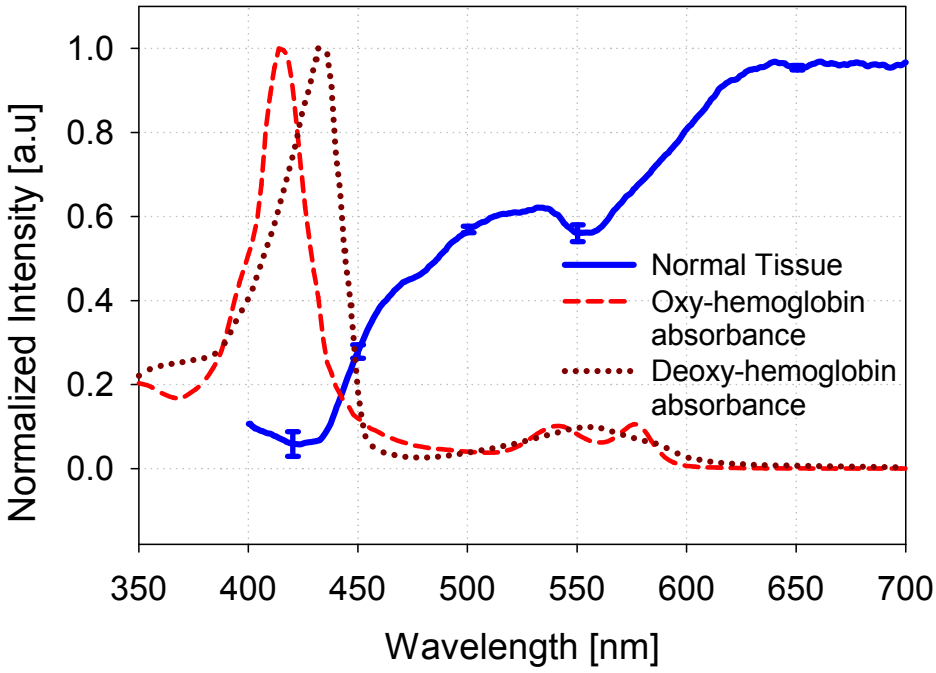

Figure 2.1 A representative normalized reflectance spectrum measured from human pancreatic normal tissue (blue, solid line) [6]. Also shown are the absorption spectra of oxy-and deoxy-hemoglobin obtained from [53]. It can be seen that the dips in the pancreatic spectrum correspond with the characteristic absorption peaks in hemoglobin at the same wavelengths.

The measured tissue spectrum is affected not only by the size and density of scatterers in the tissue but also by chromophores like hemoglobin in blood. Figure 2.1 also plots the characteristic absorption spectra of oxy-and deoxy-hemoglobin obtained from [53]. It can be seen that the dips in the pancreatic spectrum correspond with the characteristic absorption peaks in hemoglobin at the same wavelengths.

2.1.2 Steady state and time-resolved fluorescence spectroscopy

In addition to being scattered or absorbed by chromophores, the light entering tissue may be absorbed by certain molecules and excite the molecules to electronically higher states. The molecules could then lose some of their energy by non-radiative means and then re-emit a photon of lower energy. This phenomenon of light emission is called fluorescence and the molecules that fluoresce are called fluorophores [10, 11].

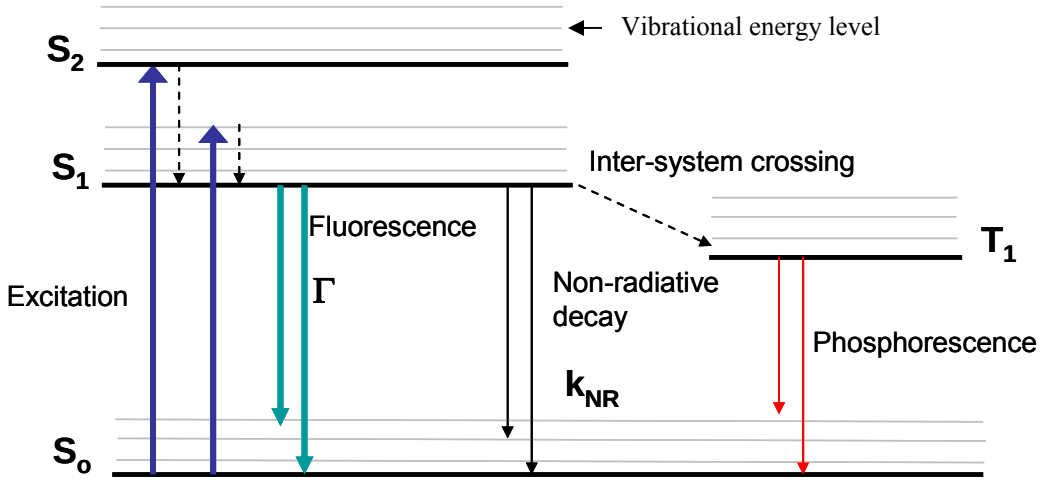

Figure 2.2 Jablonski diagram showing the energy level transitions when excitation light is incident on a molecule (adapted from [11]).

The processes involved in fluorescence are represented by an energy level diagram referred to as the Jablonski Diagram [11] (Figure 2.2). Following light absorption by fluorophore molecules, the electrons of the molecule transition from the ground state (S_0) to higher vibrational states of the first or second excited state (S_1, S_2). The molecules then relax in a time scale of ~ 10^{-12} seconds to the lowest vibrational level of S_1. At this stage, the molecules can relax to the ground state in a number of ways. They could radiatively

relax to the ground state, resulting in the emission of fluorescence photons in times typically between 10^{-9} to 10^{-8} s. The emitted fluorescence photons are typically emitted at a larger wavelength (lower energy) than the excitation photons. This change in wavelength is referred to as the Stokes shift. The molecules could also relax to the ground state by non-radiative decay processes (e.g. collisional quenching). Another possibility is the transition of the molecules to a triplet state (T_1) by spin conversion, which could then eventually relax to the ground state by emitting a phosphorescence photon. This transition termed as inter-system crossing is a forbidden transition, which implies that the decay rate for such a transition would be very short. As a result, phosphorescence photons have a longer lifetime associated with them compared to fluorescence photons.

A fluorophore is characterized by its fluorescence lifetime and quantum yield [10, 11]. If Γ and k_{NR} are the radiative and non-radiative decay rates (as shown in Figure 2.2), the measured fluorescence lifetime τ (which is the average time spent by a molecule in the excited state prior to decay to the ground state) can be calculated as,

$$\tau = 1/ (\Gamma + k_{NR}). \qquad \textbf{- 2.1}$$

The quantum yield (ϕ) is defined as the number of emitted photons relative to the number of absorbed photons and can be calculated as,

$$\phi = \Gamma/ (\Gamma + k_{NR}). \qquad \textbf{- 2.2}$$

The value for ϕ can range from 0 to 1, with a higher value implying brighter fluorescence.

There are two types of fluorescence emission measurements that can be performed - steady state (emitted fluorescence intensity as a function of wavelength) and time resolved (emitted fluorescence intensity as a function of time). Time-resolved optical

spectroscopy and imaging involves delivering a pulse of light to a sample under investigation and detecting the transient response of the medium in the time-domain. In contrast to time-resolved optical methods steady-state (or, time-integrated) fluorescence measurements integrate the signal over time, thus losing an additional dimension of information contained in the dynamics of the fluorescence decay. Fluorophore lifetimes are known to be sensitive to the local biochemical environment and to vary with pH and oxygenation in a controlled way, but are generally independent of artifacts influencing fluorescence intensity, including fluorophore concentration, photobleaching, and sources of optical loss (absorption and scattering) in biological systems [11]. This is an important issue to consider when applying fluorescence spectroscopy *in vivo*, since intensity losses attributed to hemoglobin absorption in tissue are routinely observed in the lineshape of the steady-state emission spectra when measured *in vivo* [25, 35]. In addition, since biomolecules generally have broad and overlapping fluorescence spectral bands, lifetime spectroscopy can provide an alternate means of *in situ* discrimination in multi-fluorophore systems. Despite these differences, both methods have been employed for differentiating between morphological and biochemical changes in tissue samples.

Fluorescence methods are useful in biomedical research for several reasons, including the molecular specificity of the technique, the relatively large signal strength in regions of the electromagnetic spectrum readily accessible to experimentalists, and the many bio-compatible fluorophores (endogenous and exogenous) available for study. Several endogenous bio molecules including amino acids, keratin, flavin adenine dinucleotide (FAD) and reduced nicotine amide adenine dinucleotide (NAD(P)H) and collagen are naturally fluorescent [9]. Endogenous tissue fluorescence (autofluorescence) provides

information about the native biochemical composition and microenvironment in living tissues without the use of contrast agents [5, 8-10, 25, 54-56].

2.2 Monte Carlo models for tissue photon interactions

In order to quantify optical measurements made in tissues, it is necessary to accurately describe all light-tissue interactions. Analytical treatment of light propagation in tissue is possible by considering light to be composed of neutral particles, and applying the radiative transport equation to describe photon propagation in such turbid media [57]. A common simplification to this approach has been to use the diffusion approximation to the radiative transport equation, which yields analytical solutions for the light energy distribution, both spatially and temporally, when applied to simple geometries [58-60]. The mathematical intractability and the assumptions of analytical approaches are significant and have limited the utility of the diffusion theory approximation in experiments on tissues that have multiple constituents or complex source configurations. A widely used technique for quantitative simulations of light-tissue interactions involves the use of Monte Carlo (MC) models for photon transport in turbid media, since they provide accurate predictions of light energy distribution in turbid media along with the ability to model complex tissue architectures and compositions, as well as source-detector geometries [10, 44].

Monte Carlo (MC) models for photon transport in turbid media employ tissue and fluorophore optical properties to construct photon trajectories in tissue and calculate reflectance and fluorescence photons collected at the surface of the tissues for a given source and detector fiber geometry. For a tissue with a single fluorophore in a single layer the MC code is executed as follows [61]. Excitation photons with a weight of unity are

launched from a source fiber normal to the tissue surface. The photons per unit time exiting the tissue surface are collected by annuli of detectors placed around the source fiber at increasing radii. The weight of the photon is attenuated exponentially as given by Beer's law for the absorption coefficient (μ_a) of the medium. Photon trajectories are constructed by stochastic sampling of scattering angles (specified by the anisotropy coefficient, g) and path lengths (specified by the scattering coefficient, μ_s of the medium). The flight of the photon ends either when it leaves the tissue (by crossing the tissue-air interface) or when its weight falls below a threshold minimum value (set to $1x10^{-5}$), as determined by a Russian roulette routine [62]. At the end of its travel in the tissue, the time, t, spent by the photon within the medium was given by $t = L/nc$, where L is the total path-length of the photon, c is the speed of light in vacuum, and n is the refractive index of the medium [63].

If a fluorophore is present in the medium, then the absorption of the excitation photon by the fluorophore is governed by the fluorophore absorption coefficients (μ_{afx}). Upon successful fluorescence absorption, the excitation photon is relabeled a fluorescence photon with wavelength λ_m (the emission wavelength of the fluorophore), its new direction of travel is determined by an isotropic scattering event, and its weight is multiplied by the fluorescence quantum yield ϕ. This newly created fluorescence photon then continues to propagate from the point of its spatial origin, as governed by the scattering, absorption, and anisotropy coefficients of the medium at the fluorescence emission wavelength. After each successful fluorescence absorption event, the simulation adds a decay time, to the photon's total time of flight to include the effect of a finite

fluorophore lifetime (τ). This MC code is further extendible to a tissue with multiple fluorophores and multiple layers [61].

Although the MC model requires a prior knowledge of the medium's optical transport coefficients at wavelengths of interest, it has been shown to be an accurate model for the recovery of intrinsic fluorescence from tissue for both steady-state as well as time-resolved applications [15, 36, 44, 54, 64, 65].

In this thesis, a previously developed MC transport code for photon transport in tissue media [61] was applied to model photon transport in articular cartilage tissues and to assess the fluorescence from EVPOME tissue constructs in order to select appropriate excitation wavelength, fiber diameter, and source detector geometry for optimal cellular signal detection. Details of the specific MC models used for the articular cartilage and EVPOME constructs are described in Chapter 6.

Motivated by the phenomenon discussed in this chapter, a clinically compatible instrument was designed for reflectance and fluorescence spectroscopy measurements, including lifetime sensing; the next chapter describes the details of that spectrometer.

Chapter 3

Development of clinically compatible instrumentation

This chapter describes the Reflectance and Fluorescence Lifetime Spectrometer (RFLS) [6, 56] designed and developed in this dissertation work. The RFLS is a portable, clinically compatible instrument that employs fiber optic probes for reflectance and fluorescence spectroscopy, along with time-resolved fluorescence sensing. The RFLS has been inspected for human clinical use by the Biomedical Engineering Unit affiliated with the University of Michigan Institutional Review Board (UMIRB) at the UM Hospitals and is registered as a non-hospital instrument: UMHS 318435.

Section 3.1 of this chapter describes the optical components of the RFLS and Section 3.2 explains the electrical connections. The graphical-user-interface software developed to control the RFLS and acquire data remotely is described in Section 3.3. Sections 3.4 and 3.5 describe the instrument calibration and data processing procedures. The chapter concludes with steps undertaken to monitor the performance of the instrument in Section 3.6.

3.1 Optical design

Figure 3.1 shows a schematic of the RFLS. For fluorescence excitation, the RFLS employed a pulsed, solid-state laser source (PNV001525-140, JDS Uniphase, San Jose, CA) emitting at 355 nm with a 1 KHz repetition rate (500 ps pulse width,15 μJ/pulse).

After attenuating pulse energy with a neutral density (ND) filter (ND1), laser light was delivered to the sample via an optical fiber.

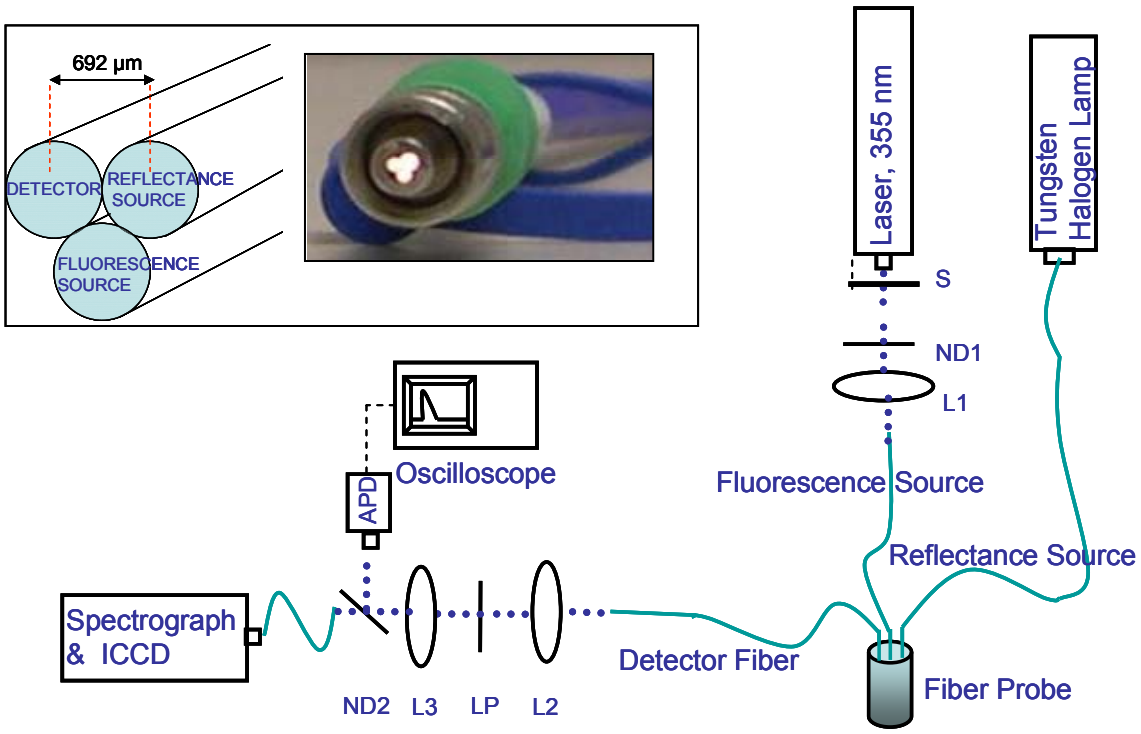

Figure 3.1 Schematic of the Reflectance and Fluorescence Lifetime Spectrometer (RFLS) (ND – neutral density filter, L – lens, LP – long-pass filter, BP- band-pass filter, APD – avalanche photo diode, ICCD – intensified charge coupled device). The inset in top left corner shows a schematic and photograph of the fiber optic probe employed during pancreatic studies.

For fluorescence spectral measurements, the emitted signal was collected by a detector fiber and focused by a series of lenses (L2 and L3) before reaching the detectors. The excitation light was eliminated at this stage by placing a long-pass (LP) filter that cut on at 387 nm (LP 57345, Spectra Physics, Mountain View, CA). A portion of the fluorescence was split off by a ND filter (ND2) and directed towards an avalanche photodiode (APD) (C5658, Hamamatsu, Bridgewater, NJ). The time-resolved signal detected by the APD was sampled at 4 MHz by a digitizing oscilloscope (TDS 784A ,

Tektronix, Beaverton, OR). The rest of the fluorescence was sent to a spectrograph (MS 125, Oriel Instruments, Stratford, CT) coupled intensified charge coupled device (ICCD) camera (ICCD 2063, Andor Technology, Belfast, Northern Ireland) for spectral data detection.

For reflectance measurements, light from a tungsten halogen lamp (HL 2000FHSA, Ocean Optics, Dunedin, FL) with continuous wave (CW) output between 360-2000 nm was delivered to the sample by a third identical optical fiber (reflectance source fiber). Reflectance measurements were made by blocking light from the laser by employing the shutter (S) and opening the shutter in front if the lamp. The scattered photons were detected by the detector fiber and directed as before to the spectrograph coupled ICCD camera for detecting the reflectance spectra.

Fluorescence and reflectance measurements were made sequentially by blocking out the light from the other source. For each spectral measurement a background signal was first collected by blocking the source lights and then that background was subtracted from the acquired data signal to give the background subtracted signal.

The light from both sources was delivered to the sample using separate optical fibers and the signal from the sample was collected and delivered to the detectors via a third identical detection optical fiber. The size and geometry of the fiber probes could be varied depending on the application [66]. For example, the distance between the source and detector fibers could be changed to probe varying depths into the sample. For the pancreatic cancer study, at the distal end, the fiber probe was comprised of the three fibers placed adjacent to each other in a triangular geometry (Figure 3.1, inset)

(customized fiber probe, Ocean Optics). The fibers had 600 µm core diameter and 0.22 numerical aperture (NA).

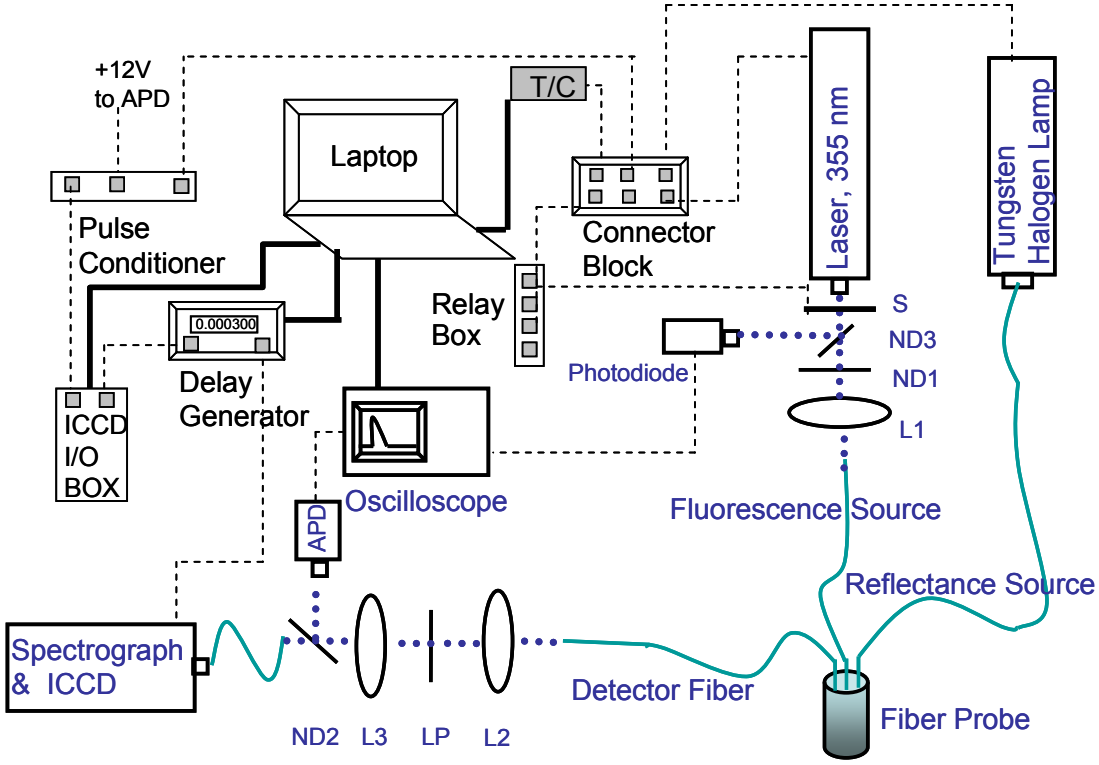

Figure 3.2 The electrical connections on the Reflectance and Fluorescence Lifetime Spectrometer (RFLS) (ND – neutral density filter, L – lens, LP – long-pass filter, BP- band-pass filter, APD – avalanche photo diode, ICCD – intensified charge coupled device).

3.2 Electronic design

Figure 3.2 is a schematic of the electrical connections employed for triggering the laser source, gating the ICCD camera, and triggering the oscilloscope during data acquisition. A medical grade isolation transformer was employed to electrically isolate the RFLS for compliance with University of Michigan IRB regulations for conducting human clinical studies. All data acquisition and instrumentation was controlled remotely via a laptop

using software written in LabVIEW (LabVIEW 7.1, National Instruments, Austin, TX) as described in Section 3.3.

3.2.1 Laser triggering and shutter control

The pulsed 355 nm laser excitation source was triggered to emit optical pulses by employing electrical pulses generated using a timer/counter (T/C) board (PCI-6602, National Instruments, Austin, TX). The T/C board was programmed to emit pulses at 1 KHz repetition rate of 55 microsecond duration. The trigger signal from the T/C board was sent via a connector block (CB-68LPR, National Instruments) to the laser.

As mentioned in Section 3.1, fluorescence and reflectance measurements were made sequentially by blocking out the light from the other source. While the lamp had an inbuilt shutter, the laser light was blocked when required by employing a home-built shutter (S). The shutter for the laser was built by attaching light blocking material to a rotatory solenoid (H-2744-032, Testco, San Jose, CA) that was controlled by the T/C board. To control the shutter, signals were sent from the T/C board via the connector block and a relay box (SC-2062, National Instruments) to the solenoid which then rotated to open or close the shutter. An appropriately light-weight material was employed for blocking light to ensure that the solenoid could rotate easily and not malfunction due to over-heating. The in-built reflectance lamp shutter was also controlled employing the T/C board by sending signals from the board via the connector block and relay box to the lamp shutter.

3.2.2 Gating of the ICCD

To minimize background signal during fluorescence spectra acquisition, the ICCD gating was synchronized with the arrival of the fluorescence signal. A portion of the trigger signal to the laser was input to a home built pulse conditioner (described previously [67]), which provided a stable TTL pulse output. The TTL pulse was then input to a delay generator (DG535, Stanford Research Systems, Sunnyvale, CA) that introduced a 175 μs gate delay and 30 μs gate width in the ICCD with respect to the triggering of the laser. These setting corresponded with the time delay between the emission of the laser excitation pulse and when the emitted fluorescence reached the ICCD camera (gate delay) and the duration of the emitted fluorescence (gate width). These settings would need to be changed if a significantly longer or shorter fiber probe is employed for data collection.

Typically, a few 100 ns at most should be an appropriate gate width to capture the transient fluorescence from endogenous fluorophores. However, the gate width had to be set to 30 μs due to an inherent temporal jitter in the output from the laser. In addition, the laser was not left on for periods longer than 2 hours at a time, as this would lead to a thermal drift in the laser pulse emission time which in turn would have required changing the gate delay parameter.

3.2.3 Triggering of the oscilloscope

The oscilloscope was externally triggered to synchronize the sampling of the time-resolved fluorescence signal acquired by the APD with the emission of the laser excitation pulse. A ND filter (ND3) of optical density 0.03 was employed to direct a

portion of the emitted laser light to a second photodiode (DET10, Thorlabs) (Figure 3.2). The signal from this photodiode was employed as an external trigger to the oscilloscope.

3.3 Software

A graphical user interface (GUI) program was developed in LabVIEW for data collection using the RFLS. The developed GUI enabled remote, fully automated acquisition and storage of fluorescence and reflectance data sequentially. The software had the following functions:

- The GUI provided easy access to instrument acquisition parameters including gate width, gate delay, number of data acquisitions to average (spectral and time-resolved), and ICCD chip exposure times for both fluorescence and reflectance acquisition.
- The GUI enabled the automated storage of fluorescence and reflectance spectral data and fluorescence life-time decays with a date and time stamp into folders chosen by the user.
- The GUI provided control of the energy of laser excitation photons reaching the sample (ND1) and the fraction of light transmitted to the ICCD for spectral detection (ND2). This was achieved by employing motorized rotating filter wheels (FW102, Thor Labs) remotely controlled via the GUI. Six ND filters of varying optical density could be positioned on each of the filter wheels thus providing a choice of 6 ND1 and 6 ND2 filter to choose from. This enabled the detection of optimized optical signals with low noise and without the risk of saturating the detectors (ICCD and APD) due to excessive signal.

- The software remotely controlled the laser and lamp shutters and enabled the acquisition of a background spectrum prior to data acquisition. The user could then choose to either store background subtracted or raw measured spectral data.
- Prior to data acquisition, the software cooled the ICCD head to -5 ^{o}C to decrease dark noise in the ICCD camera chip. After data acquisition, the software ensured a controlled increase of the ICCD temperature to avoid thermal stress in the output optical fibers on the intensifier of the ICCD.

3.4 Instrument calibration

The RFLS was calibrated for wavelength and absolute fluorescence and reflectance spectral intensity by employing procedures in [67]. These procedures are briefly described below.

Wavelength calibration was performed to assign wavelength values to each of the 1024 pixels on the ICCD camera of the RFLS. An Hg(Ar) lamp (6035, Oriel Instruments, Stratford, CT) with emission lines at known wavelengths was employed. The lamp emission was measured using the RFLS and the ICCD pixel number corresponding to each known emission line was noted. The pixel numbers and the corresponding emission wavelengths were then employed to assign a wavelength to each pixel of the ICCD camera of RFLS.

The RFLS spectral instrument response $S(\lambda)$ was calculated by measuring the emission from a National Institute of Standards and Technology traceable tungsten halogen lamp (63355 S.N. 7-1329, Oriel Instruments) and dividing it by the known theoretical spectrum provided by Oriel Instruments. Calibration for the spectral instrument response was then achieved by dividing measured spectra by $S(\lambda)$.

3.5 Data processing

For fluorescence and reflectance spectral measurements, a background spectrum was acquired with the sources blocked and was subtracted from the detected sample spectrum. Background subtracted data were then corrected to give distortion free spectra by calibrating the wavelength and correcting for the spectral instrument response of the RFLS as described in Section 3.4 and in [67].

Reflectance spectra were also corrected for the intensity spectrum of the lamp. First, the lamp spectrum was measured by placing a diffuse reflectance standard (SRS-50-010, Labsphere, North Sutton, NH) in lieu of the tissue sample. Next, the background subtracted and instrument response corrected sample reflectance spectrum (R_{sample}) was divided by the background subtracted and instrument response corrected lamp spectrum (R_0), to give the reflectance spectrum (R) (i.e. $R = R_{sample} / R_0$).

The RFLS also has a temporal instrument response due to the finite pulse width of the laser excitation pulse and response of the electronics. Measured time resolved fluorescence decays $M(t)$ were interpreted as a convolution of the intrinsic fluorescence decay, $f(t)$, and the temporal instrument response function, $I(t)$: i.e. $M(t) = f(t) \otimes I(t)$ as detailed in [67]. The instrument response function $I(t)$ was measured using the scatter of the excitation pulse by a dilute solution of silica spheres (Bangs Laboratories, Inc., Fishers, IN).The intrinsic fluorescence decay ($f(t)$) was then calculated by least-squares iterative reconvolution (Light Analysis software, Quantum Northwest, Inc., Spokane, WA), where $f(t)$ was modeled as a multi-exponential decay: $f(t) = \sum c_i \, exp\,(-t/\tau_i)$. The average decay time τ, was then calculated as $\tau = \sum c_{i*} \tau_i^2 / \sum c_{1i*} \tau_{1i}$. Section 3.6 shows an example of time-resolved fluorescence data analyzed in this manner.

3.6 Monitoring the performance of the RFLS

The RFLS is a portable device that was transported to the surgery suites for data acquisition. It was necessary to ensure that the calibration of the instrument and the alignment of the optics were not disturbed during these trips and that data from measurements made on multiple days could be relied upon. Measuring fluorophore standards along with laser output energy and the lamp spectrum R_0 as detailed in Section 3.5 helped to monitor the performance of the RFLS instrument.

Spectral measurements:

Prior to, and post data acquisition, solutions of 1 μM Rhodamine B (R6626, Sigma Aldrich, St. Louis, Missouri) in DI water and 1 μM Fluorescein (166308, Aldrich) in de-ionized (DI) water were measured to ensure the wavelength and spectral instrument response had not changed. These solutions were also measured by employing a spectrofluorometer (Fluorolog-3, Horiba Jobin Yvon) as well as the RFLS measurements The Fluorolog-3 is described in detail in Section 4.1.3. The measurements from the two instruments were compared to check the wavelength calibration and spectral instrument response of the RFLS. Figure 3.3 plots a typical measurement of Fluorescein and Rhodamine B fluorescence measured by employing the Fluorolog-3 (dotted lines) and RFLS (solid lines) instruments.

The coincidence of the location of the peaks indicated that the wavelength calibration of the RFLS was correct and the coincidence of the spectral shapes indicated that the spectral instrument response of the RFLS was correct.

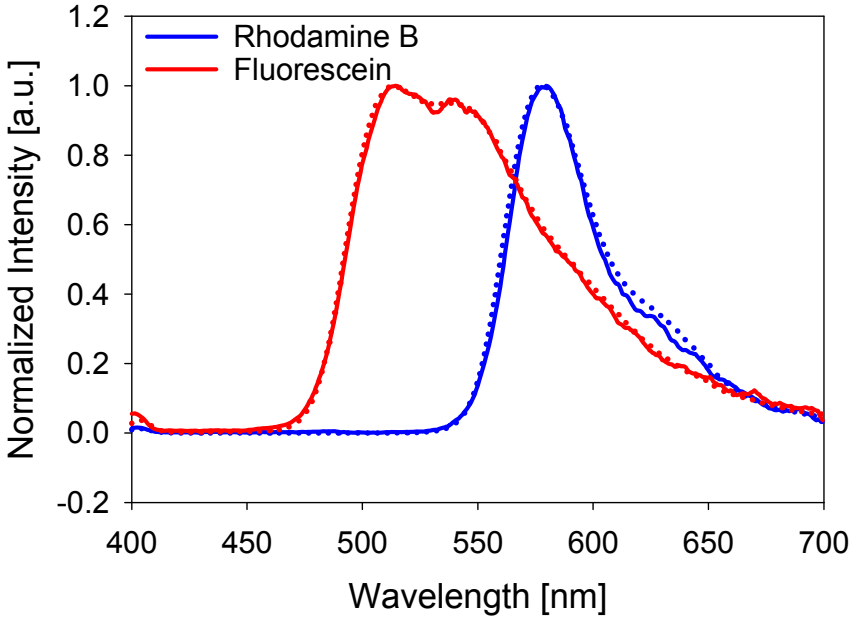

Figure 3.3 Plot of the fluorescence spectrum of solutions of 1 µM Rhodamine B in water (blue) and 1 µM Fluorescein in water (red) measured by employing the Reflectance and Fluorescence Lifetime Spectrometer (RFLS) (solid lines) and the Fluorolog-3 spectrofluorometer (dotted lines).

Time resolved fluorescence measurements:

Freshly prepared solutions of 1µM POPOP (P3754, Sigma Aldrich) in cyclohexane and 1µM Rhodamine B in DI water were measured before and after data acquisition and the extracted decay times were compared to literature values for these single exponential decay fluorophores (1.58 ± 0.08 ns, for Rhodamine B in water and 1.12 ± 0.02 ns, for POPOP in cyclohexane) [68]. Figure 3.4 plots a time-resolved fluorescence decay curve measured employing the RFLS from Rhodamine B in water (red dashed line). The instrument response of the RFLS (solid black line) is labeled ‘‘Excitation’’ and was measured with a dilute solution of silica spheres as described in Section 3.5. Data were fit to a single exponential decay [67]. The plot also shows the residual between the measured fluorescence and the simulated fit (labeled “Simulation”).

An example of the mean ± standard deviation decay times extracted from two successive fluorescence decay measurements of Rhodamine B and POPOP are: 1.49 ± 0.01 ns and 1.05 ± 0.01 ns, respectively. These extracted decay times were in good agreement with the literature values.

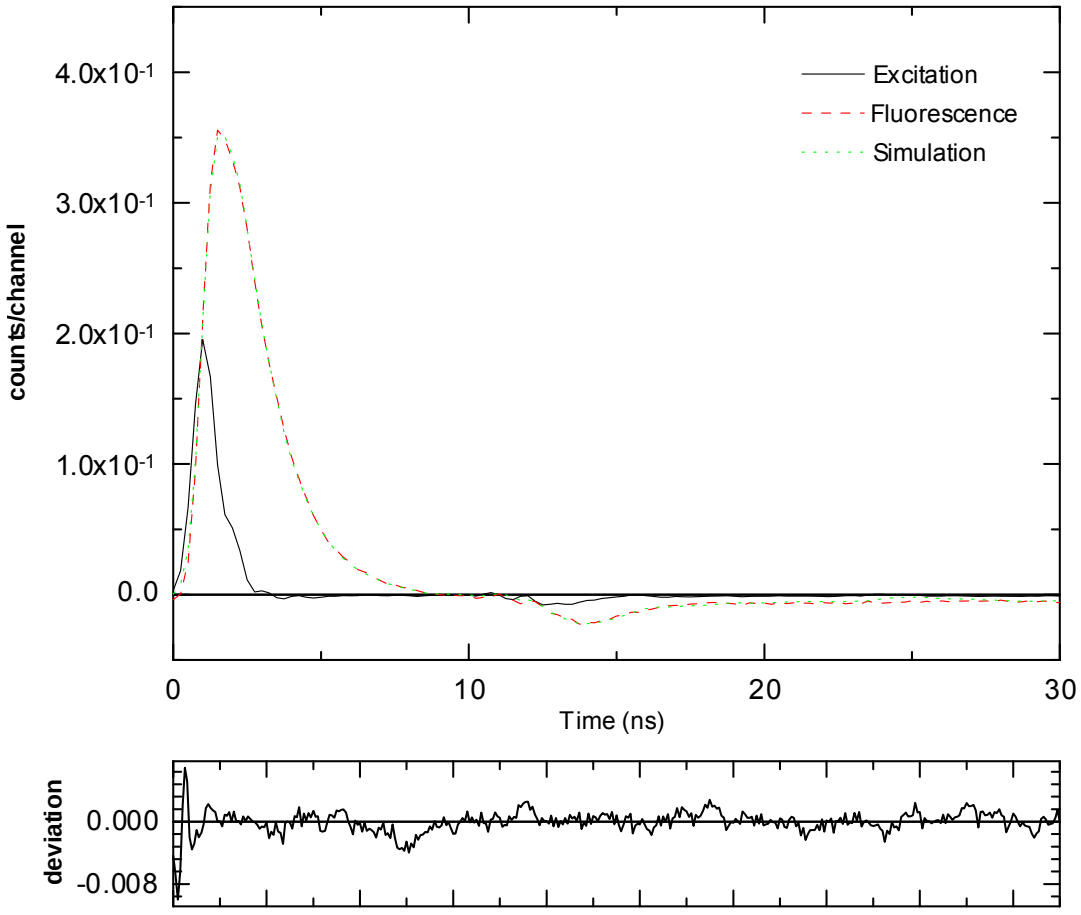

Figure 3.4 Time-resolved fluorescence of 1 μM Rhodamine B in water (red dashed line) measured employing the RFLS. Data were fit to a single exponential decay (green dotted line, labeled "simulation") with a lifetime of 1.5 ns. The instrument response of the RFLS (solid black line) is labeled ''Excitation'' and was measured with a dilute solution of silica spheres.

Thus, a clinically compatible, fiber optic coupled instrument was developed for measuring reflectance and fluorescence spectra and time-resolved fluorescence decay curves from biological tissues. This instrument was employed for multi-modal optical

measurements from human pancreatic tissues, (Chapter 4) human pancreatic xenografts in mice (Chapter 4), porcine articular cartilage (Chapter 6), and tissue engineered oral mucosa devices (Chapter 6).

Chapter 4

Optical spectroscopy for pancreatic adenocarcinoma detection

Pancreatic adenocarcinoma is a leading cause of cancer death with a five-year survival rate of only 5%. Endoscopic ultrasound-guided fine-needle aspiration (EUS-FNA), the current diagnostic standard, cannot reliably rule out malignancy, and is insensitive to distinguishing adenocarcinoma from chronic pancreatitis (inflammation). In this study, for the first time, we tested the ability of multi-modal optical spectroscopy to detect signals from pancreatic tissue by studying human pancreatic cancer xenografts in mice and freshly excised human pancreatic tissues, and correlated measured optical spectra and fluorescence decays with pathology [6, 69]. Section 4.1 describes the *in vivo* and *ex vivo* mouse studies of human pancreatic xenografts in mice and presents the results of the study. Section 4.2 describes the *ex vivo* measurements of human pancreatic cancer tissue during pancreatic surgeries. The section discusses the histopathology of the measured sites and presents the spectral data. The section also presents the time-resolved fluorescence data measured on a limited data set.

4.1 Optical spectroscopy of human pancreatic xenografts in mice

4.1.1 Pancreatic cancer xenografts in mouse models

Cultured human pancreatic cancer cells derived from mouse xenografts initiated with cells from a patient with pancreatic adenocarcinoma (AsPC-1, American Culture

Collection Type, Manassas Virginia) were cultured in RPMI 1640 medium with 2 mM L-glutamine adjusted to contain 1.5 g/L sodium bicarbonate, 4.5 g/L glucose, 10 mM HEPES, and 1.0 mM sodium pyruvate and 10% fetal bovine serum at 37^{o}C with 5% CO_2 on 100mm plates. Cells were grown to 80% confluence, harvested by trypsinization, washed with medium and 10% fetal bovine serum, and re-suspended to a final concentration of 1 x 10^6 cells/ml in sterile phosphate buffered saline.

4 week old male NOD/SCID mice (non-obese diabetic/severe combined immunodeficiency) were housed in a sterile environment. Cages, bedding, food, and water were all autoclaved. All animals were maintained on a daily 12-hr light/12-hr dark cycle. The animals were anesthetized using 100 mg/kg ketamine and 15 mg/kg of xylezene injected intraperitoneally. The abdomen was opened via a 2 cm midline incision, and the tail of the pancreas was exposed. The pancreas was then injected with 10^5 AsPC-1 cells suspended in 100 μl of sterile phosphate buffered saline solution. The midline wound was then closed in 2 layers.

For optical characterization of the tumor, 3 weeks after tumor injection, the mice were anesthetized using 100 mg/kg ketamine and 15 mg/kg of xylezene injected intraperitoneally. The abdomen was opened laterally to the previous 2 cm midline incision, and the tail of the pancreas exposed. The first mouse had a 0.4 cm mass in the pancreas. The second had a 0.7 cm mass in the tail of the pancreas. *In vivo* reflectance and fluorescence spectroscopy measurements were made on the tumors by employing the RFLS. The tumors were then resected and a spectrofluorometer was employed to obtain *ex vivo* fluorescence excitation-emission matrices. The animal study was approved by the University of Michigan Committee on Use and Care of Animals.

4.1.2 *In vivo* RFLS measurements

Reflectance and fluorescence spectral data were obtained using the Reflectance and Fluorescence Lifetime Spectrometer (RFLS) (described in Chapter 3). Briefly, for fluorescence measurements, a pulsed 355 nm excitation source was employed. A tungsten halogen lamp was employed as the reflectance source. The fluorescence and reflectance spectra were collected using a spectrograph coupled intensified charge coupled device (ICCD) camera. The light from both sources was delivered sequentially to the sample using separate optical fibers (600 micron core) (SFS600/660 Fiberguide Industries) and the signal from the sample was collected and delivered to the spectrograph via a third identical fiber. At the distal end, the three fibers were placed in a triangular geometry. Figure 4.1 shows the fiber probe placed on the pancreas of a NOD/SCID mouse during *in vivo* RFLS measurements.

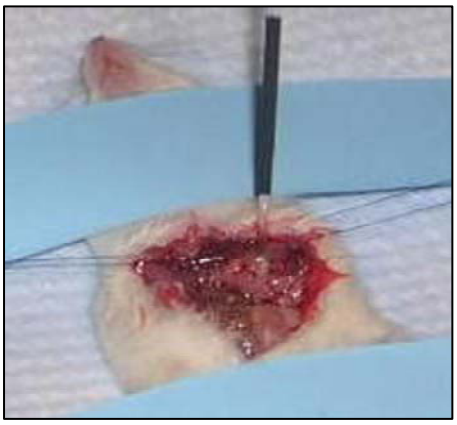

Figure 4.1 NOD/SCID (non-obese diabetic/severe combined immunodeficiency) mouse pancreas with human pancreatic cancer xenograft during *in vivo* measurement [6]. Measurements were made employing the clinically compatible reflectance and fluorescence lifetime spectrometer (RFLS).

All measured spectra were background subtracted and corrected for the spectral instrument response. The measured reflectance spectra were also scaled by the measured intensity spectrum of the lamp (R_o) to get the corrected reflectance spectra (R/R_o). Details of the calibration are described in Chapter 3. All corrected fluorescence and reflectance spectra were then normalized by scaling the peak intensity to unity.

The gray solid line in Figure 4.2 shows *in vivo* fluorescence measured from a human pancreatic cancer xenograft grown in one of the mice. The measured fluorescence peaked around 460 nm indicating predominant fluorescence from NAD(P)H [9].

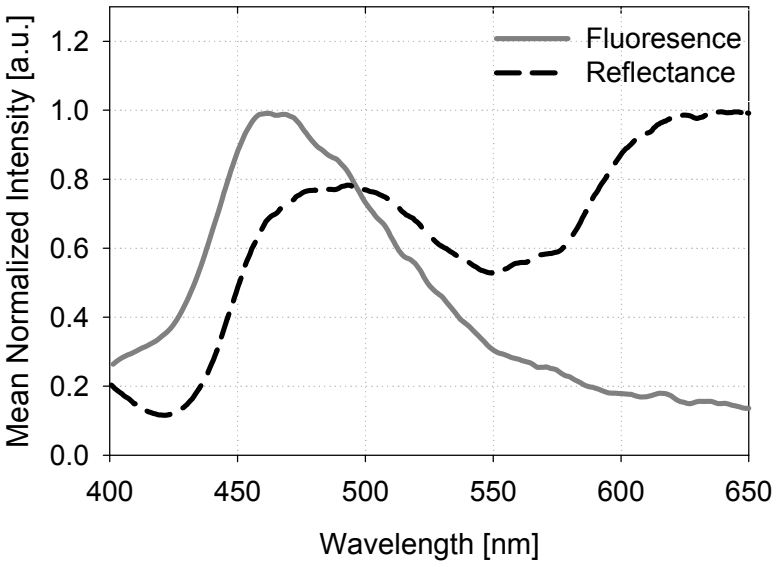

Figure 4.2 The fluorescence spectrum of *in vivo* adenocarcinoma xenograft in a mouse model (gray solid line). Reflectance spectrum of adenocarcinoma xenograft is also shown (black dashed line). Measurements were made employing the clinically compatible reflectance and fluorescence lifetime spectrometer (RFLS).

In general, pancreatic tumor tissue is expected to have excess fibrosis. Thus, predominant fluorescence emission associated with collagen might be expected. However, since SCID mice were employed, due to their immunodeficiency, the expected fibrosis associated with tumor tissue was absent. Thus, the measured xenograft fluorescence could be

associated primarily with the cellular component of the grown tumor (mainly NAD(P)H) and corresponded well with the fluorescence attributed to the cellular signal in the human study (results in Section 4.2.2). The black dashed line in Figure 4.2 shows an *in vivo* reflectance spectrum measured from the same human pancreatic xenograft. The spectrum showed characteristic hemoglobin absorption dips at approximately 400–440 and 540–580 nm as was discussed in Section 2.1.1 [28].

4.1.3 *Ex vivo* spectrofluorometer measurements

The pancreatic cancer xenografts grown in the mice were resected after the *in vivo* measurements and excitation emission matrices (EEMs) were measured using a spectrofluorometer (SPEX® FL3-22 Fluorolog-3, Jobin-Yvon Horiba, Japan). The Fluorolog-3 spectrofluorometer was equipped with a 450 W Xe short arc lamp source that was focused onto a tunable, double excitation spectrometer (Czerny-Turner 1200/mm kinematic grating blazed at 330 nm) to produce a monochromatic collimated excitation beam at the sample at any desired wavelength from 290-900 nm. Emitted fluorescence was collected perpendicular to the excitation direction, collimated, and dispersed by a tunable double emission spectrometer (Czerny-Turner 1200/mm kinematic grating blazed at 500 nm) into a multialkali photomultiplier tube detector. The system was interfaced to a computer via custom software which allowed an automated scanning of the sample via measurement of an excitation spectrum, an emission spectrum, or combined EEM spectra. The tumor samples were front illuminated at a 45^{o} angle to the excitation beam to obtain the EEM for 20 excitation wavelengths between 300 and 450 nm while monitoring the emission from 300 to 650 nm (at 2 nm increments).

Figure 4.3a shows EEM data acquired *ex vivo* from the pancreatic cancer xenograft grown in one of the mice. The EEM fluorescence intensity pattern was consistent with endogenous tissue fluorescence predominantly originating from tryptophan (peak emission about 350 nm), intracellular NAD(P)H (peak emission about 460 nm) along with some fluorescence from extracellular collagen (peak emission about 400 nm) [5, 8-10, 25, 54-56]. Figure 4.3b shows this EEM data around excitation wavelength 355 nm, which was the wavelength employed for excitation in RFLS studies. As was observed in the *in vivo* measurements, the measured fluorescence peaked around 460 nm indicating predominant fluorescence from NAD(P)H for 355 nm excitation, as was expected since the mice were immunodefficient and so the expected fibrosis usually associated with tumor tissue was absent.

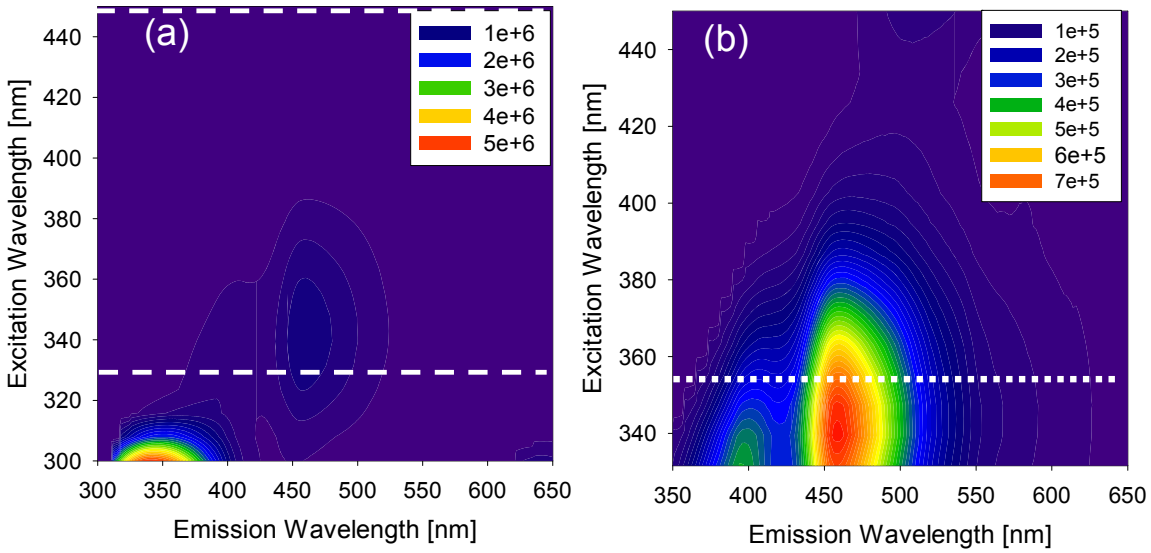

Figure 4.3 (a) Measured EEM of a pancreatic cancer xenograft grown in a NOD/SCID mouse showing fluorescence emission primarily associated with tryptophan, extracellular collagen, and intracellular NAD(P)H [69]. (b) Same EEM expanded to highlight the area between white dashed lines in (a) showing fluorescence emission primarily associated with collagen and NAD(P)H. RFLS excitation in the human studies occurred at 355 nm (white dotted line) [69]. The EEM data was measured on the Fluorolog-3 spectrofluorometer.

4.2 *Ex vivo* optical spectroscopy of human pancreatic tissues

Reflectance and fluorescence spectra and time-resolved fluorescence decays were measured from freshly excised human pancreatic tissues obtained during pancreatic surgical procedures, by employing the fiber optic coupled RFLS. Figure 4.4 shows the fiber optic probe (discussed in Section 3.1) placed on human pancreatic tissue during data acquisition. A total of 90 sites were measured on tissues obtained from 12 patients within 30 minutes of excision. Table 4.1 shows the details of the patients' age, gender, and final diagnosis of the resected specimen. Two sets of fluorescence and reflectance measurements were made on each site, excepting one site. After data acquisition from each measurement site, a tissue biopsy was immediately performed to link optical measurements with histopathologic analysis. The study was approved by the Institutional Review Board of the University of Michigan (U of M) and written patient consent was obtained prior to data acquisition.

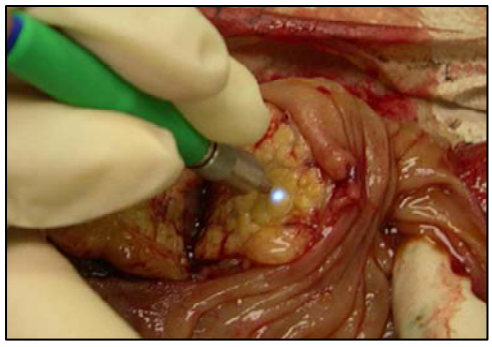

Figure 4.4 Human pancreatic tissue during *ex vivo* measurement [6]. Measurements were made employing the clinically compatible reflectance and fluorescence lifetime spectrometer (RFLS).

The acquired fluorescence spectra were corrected for spectral instrument response after background correction [67]. The reflectance spectra were also background subtracted and

then scaled by the lamp reflectance spectrum (R_o) to obtain the corrected reflectance spectra (R/R_o) [56]. All spectra were normalized by scaling the peak intensity value to unity.

Table 4.1. Patient information and final diagnosis

Patient	Age	M/F	Final Diagnosis
1	68	F	Adenocarcinoma
2	41	F	Adenocarcinoma
3	79	F	Adenocarcinoma
4	54	M	Intraductal papillary mucinous neoplasm, adenoma type. No invasive carcinoma identified. Chronic pancreatitis.
5	69	M	Serous cystadenoma
6	53	F	Lipomatous pseudohypertrophy with foci of fat necrosis. Background pancreas with mild patchy chronic pancreatitis
7	60	M	Intraductal papillary mucinous neoplasm with high grade dysplasia. No invasive carcinoma was identified. Chronic pancreatitis
8	69	F	Adenocarcinoma
9	70	M	Adenocarcinoma
10	63	F	Chronic Pancreatitis
11	65	F	Adenocarcinoma
12	76	F	Metastatic breast adenocarcinoma

4.2.1 Histopathology and inclusion criterion

Figure 4.5 shows representative histology slides of samples obtained from sites with (a) normal, (b) chronic pancreatitis, and (c) adenocarcinoma tissue after RFLS optical measurements. The images were taken at 200x magnification. Hematoxylin and eosin (H&E) were used as the staining agent. The light pink in the slides denotes the stroma or extra cellular matrix (ECM) where collagen resides while the nuclei, where NAD(P)H and FAD are found, stained dark purple.

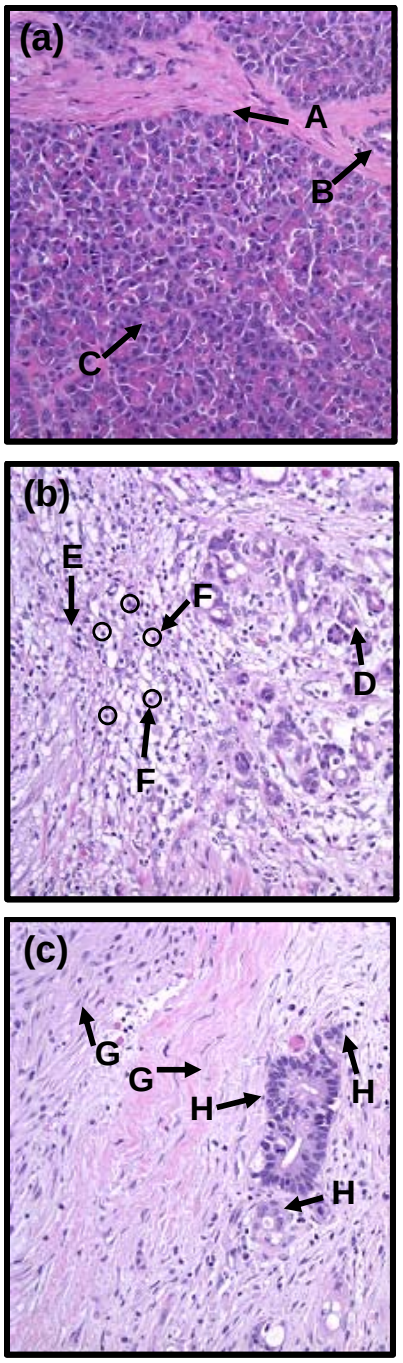

Figure 4.5. Shows representative histology slides [69] of human tissue obtained from - (a) Normal pancreatic tissue [A - normal component of fibrous stroma between pancreatic lobules; B - small interlobular pancreatic duct; C- normal pancreatic lobule with acinar cells having abundant granular cytoplasm and little intervening stroma]. (b) Chronic pancreatitis tissue [D- acinar cells separated by abundant fibrous stroma and inflammation; E- abundant interlobular inflamed fibrous tissue; F- white blood cells having small dark nuclei (shown in small circles)]. (c) Adenocarcinoma tissue [G - adenocarcinoma cell groups surrounded by abundant fibrous stroma; H - adenocarcinoma cells having enlarged dark nuclei, and arranged in duct-like structures]. (200 x magnification and H&E stain were employed).

The normal pancreatic tissue histology (Figure 4.5a) shows normal component of fibrous stroma between pancreatic lobules (A), small interlobular pancreatic duct (B), and normal pancreatic lobule with acinar cells having abundant granular cytoplasm and little intervening stroma (C).

Chronic pancreatitis is associated with an increase in fibrosis (mainly collagen) due to inflammation. This also leads to more white blood cells (lymphocytes) in the tissue. This is evident in Figure 4.5b where abundant interlobular inflamed fibrous tissue (E – light pink) can be seen along with white blood cells having small dark nuclei (F- shown in small circles). Acinar cells were now observed separated by abundant fibrous stroma and inflammation (D) unlike in the normal tissue.

Figure 4.5c shows adenocarcinoma cell groups surrounded by abundant fibrous stroma just like in the pancreatitis tissue (G). However unlike pancreatitis, adenocarcinoma cells have enlarged, dark nuclei (H). In the figure, the cells can be seen arranged in duct-like structures. This observed increase in fibrosis and excess collagen in both chronic pancreatitis and adenocarcinoma tissue, and an increase in the nuclear size in adenocarcinoma cells, was expected to affect the optical measurements made on these tissues.

Histopathology indicated that of the 90 measured sites from 12 patients, 17 were adenocarcinoma sites, 22 were chronic pancreatitis sites, and 11 were normal tissue sites. The remaining 40 sites were either malignant breast cancer that had metastasized to the pancreas (10 sites), intraductal papillary mucinous neoplasm (8 sites), pancreatic intraepithelial neoplasia (6 sites), serous cystadenoma (8 sites), scar or fat tissue or both (5 sites), or a hybrid tissue site having two or more of the above mentioned pathologies (3

sites). These 40 sites were excluded from the data set used for tissue classification algorithm development in Chapter 5. Their analysis will be considered in the future, once a larger data set is in place. Table 4.2 indicates the pathology of the measured sites, for each patient. The numbers in green indicate the sites that were included in algorithm development while red indicates the excluded data.

Table 4.2. Patient-wise histology of the sites from which data was collected
(Red: excluded data; Green: included data)

Patient	N	P	A	PanIN	IPMN	SCA	MBC	Scar/ fat/ both	P and A[a]	N and A[b]
1	2	3	-	-	-	-	-	-	-	-
2	-	-	5	-	-	-	-	-	-	-
3	-	5	-	1	-	-	-	1	1	
4	-	3	-	-	1	-	-	1	-	-
5	-	-	-	-	-	8	-	-	-	-
6	4	-	-	1	-	-	-	-	-	-
7	-	-	-	-	7	-	-	1	-	-
8	-	4	1	1	-	-	-	-	1	1
9	5	1	1	3	-	-	-	-	-	-
10	-	6	-	-	-	-	-	2	-	-
11	-	-	10	-	-	-	-	-	-	-
12	-	-	-	-	-	-	10	-	-	-

N: Normal; P: Pancreatitis; A : Adenocarcinoma; PanIN : Pancreatic Intraepithelial Neoplasia; IPMN: Intraductal papillary mucinous neoplasm; SCA : Serous Cyst Adenoma; MBC: metastatic breast carcinoma
a: A hybrid tissue site of chronic pancreatitis and adenocarcinoma;
b: A hybrid tissue site of focal adenocarcinoma at the edge of mostly normal tissue

Furthermore, fluorescence spectra with signal to noise ratio (SNR) less than 25 (two spectra) were excluded from the data set. SNR was calculated as mean signal at peak fluorescence divided by the standard deviation of noise in the data (SNR = (average intensity between 470-500 nm) / (standard deviation of intensity between 700-750 nm)). Reflectance spectra that had a ratio of reflectance at 550 nm to that at 650 nm less than

0.1 were also excluded from the data set (one spectrum). The corresponding fluorescence and reflectance spectra of these spectra were also excluded, resulting in the exclusion of 3 pairs of fluorescence and reflectance spectra.

This left data from 9 patients and 50 sites: 33 pairs of measured reflectance and fluorescence spectra from adenocarcinoma, 41 pairs of spectra from chronic pancreatitis measurements, and 22 pairs of spectra from measurements of normal pancreatic tissue. These 96 pairs of measured reflectance and fluorescence spectra were used for the development of tissue classification algorithms (discussed in Chapter 5).

The corresponding 96 time-resolved fluorescence decays were obtained by detecting either: (a) fluorescence emission from 360-750 nm (76 measurements) or, (b) fluorescence emission from 500-750 nm (20 measurements). Analysis was restricted to the 76 measurements from category (a), as all category (b) measurements were from adenocarcinoma sites only. Of these 76 measurements, 19 were excluded due to initial errors (subsequently resolved) in triggering the oscilloscope during data acquisition. This left 57 time-resolved fluorescence decay measurements, of which, 4 were made on adenocarcinoma sites, 35 were made on chronic pancreatitis sites, and 18 were made on normal pancreatic tissue sites. Considering the small number of adenocarcinoma measurements in this subset, tissue classification algorithm development was limited to the remaining 18 normal and 35 chronic pancreatitis tissue time-resolved fluorescence decays (results in Section 4.2.3).

4.2.2 Spectral data

Figure 4.6 shows the mean of normalized measured reflectance and fluorescence spectra for adenocarcinoma (red dashed line), chronic pancreatitis (green dot-dashed line), and

normal (blue solid line) pancreatic tissues along with the standard error at select wavelengths.

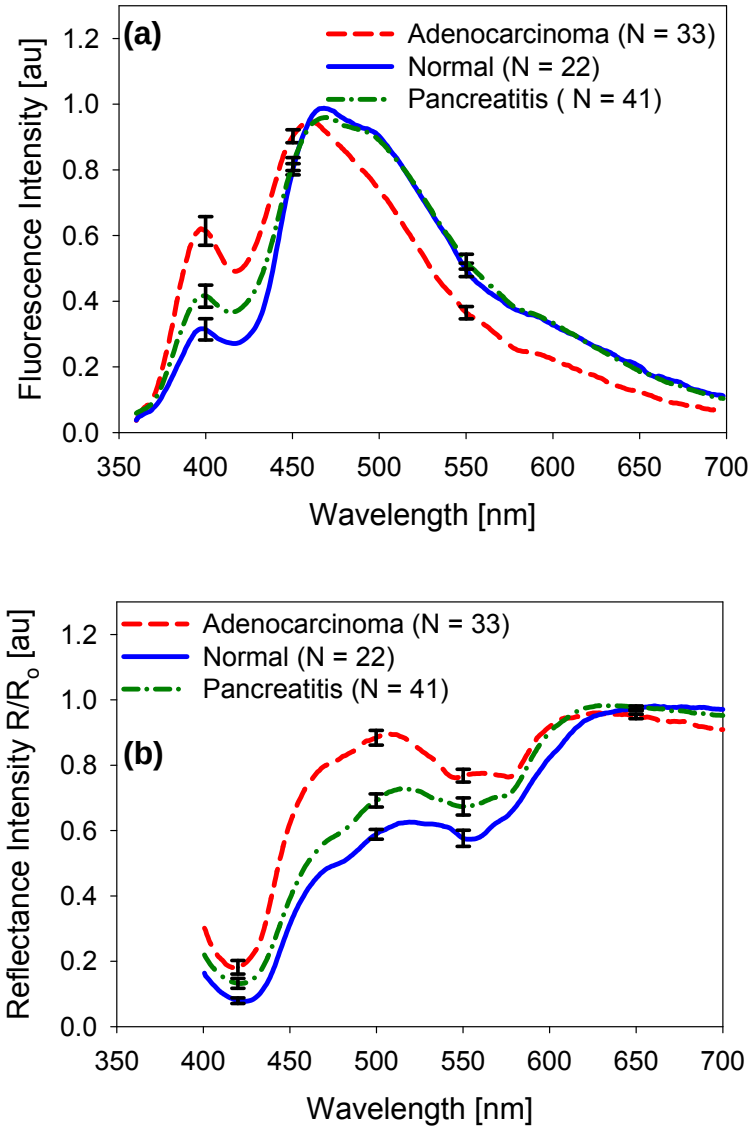

Figure 4.6 (a) Mean fluorescence spectra obtained from human pancreatic normal (blue), pancreatitis (green dot-dash), and adenocarcinoma (red dashed) tissues. (b) Mean reflectance spectra obtained from normal (blue), pancreatitis (green dot-dash) and adenocarcinoma (red dashed) tissues. *N* denotes the number of individual spectra. The standard error is shown at select wavelengths [70].

Tissue fluorescence spectra revealed cellular NAD(P)H (emission around 460 nm) and extracellular matrix collagen (emission around 400 nm) and characteristic hemoglobin

absorption dips at around 420, 540, and 575 nm in the reflectance and fluorescence spectra [55, 56]. The relative collagen emission from adenocarcinoma and chronic pancreatitis tissues was larger than that from normal tissues, as anticipated from the increase in fibrosis in the diseased tissues [71]. The cellular fluorescence corresponded well with the fluorescence attributed to the cellular signal in the mouse study ((Figure 4.2, gray solid line).

Features in the 400–440 and 540–580 nm ranges in both fluorescence and reflectance spectra could be attributed to hemoglobin absorption [28]. The adenocarcinoma sites showed a higher reflectance than chronic pancreatitis and normal tissue sites in the 430 to 500 nm range. Such tissue reflectance features have been associated with both the density and size of cellular scatterers (e.g. nuclei and organelles) [28, 72]. Indeed, this reflectance feature was observed in the data obtained from xenograft tumor in mice (Figure 4.2, black dashed line) and corresponded well with measurements made on human adenocarcinoma.

4.2.3 Time-resolved fluorescence data

As described in Section 4.2.1, analysis of the time-resolved fluorescence decay measurements was restricted to a limited data set comprising of 35 chronic pancreatitis and 18 normal tissue measurements. Figure 4.7a plots the mean of the normalized measured time-resolved fluorescence decay curves from these pancreatitis (green, dashed line) and normal (blue, solid line) tissue sites.

Figure 4.7b plots the same data on a logarithmic scale to enhance for viewing purposes the difference between the decay curves of the two tissue types.

All the measured time resolved data were interpreted as a convolution of the instrument response curve with the intrinsic fluorescence decay curve ($f(t)$) as described in Section 3.5 [67]. The instrument response was measured using the scatter of the excitation pulse by a dilute solution of silica spheres. $f(t)$ was interpreted as a triple exponential decay of the form $f(t) = \sum exp(-a_i t_i/\tau_i)$, (i = 3) with lifetimes τ_i and amplitudes a_i. The average decay time was defined as $\tau_{avg} = a_1\tau_1^2 + a_2\tau_2^2 + a_3\tau_3^2 / (a_1\tau_1 + a_2\tau_2 + a_3\tau_3)$.

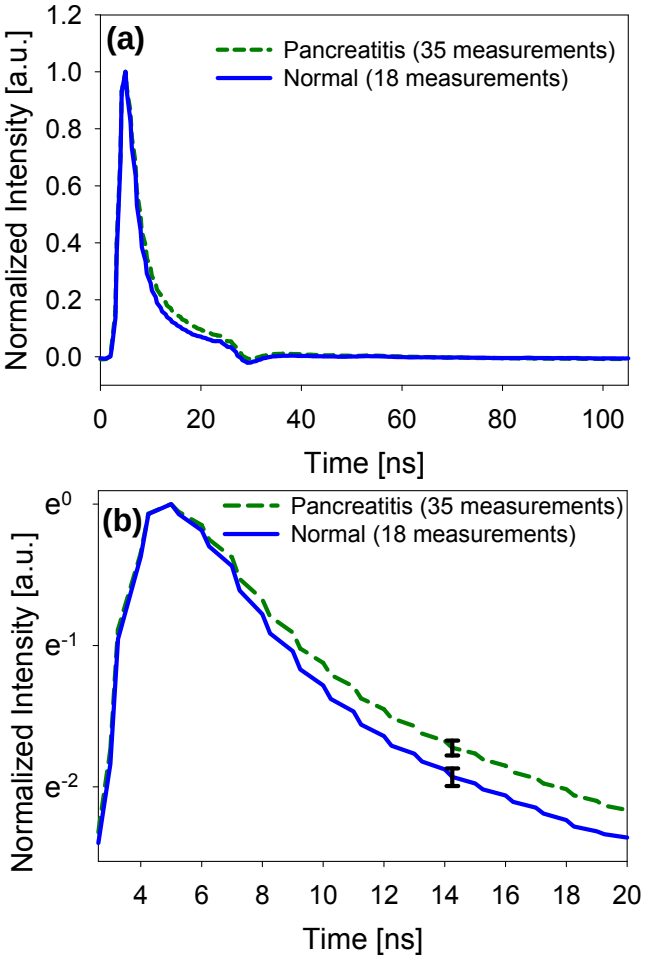

Figure 4.7 (a) Mean normalized time-resolved fluorescence decay, measured from chronic pancreatitis (green dashed line, 35 measurements) and normal (blue solid line, 18 measurements) pancreatic tissue sites. (b) The plot on a logarithmic scale zoomed with the standard error shown at a select time point.

The mean τ_{avg} was 4.5 ± 1.7 for chronic pancreatitis tissue (35 measurements), and 3.3 ± 0.9 ns for normal tissue (18 measurements). Wilcoxon rank sum test of the decay times of normal and chronic pancreatitis tissue indicated a difference in the median decay times of the tissues (p-value = 0.0078). The relative excess of collagen emission from chronic pancreatitis vs. normal tissue corresponded well with this increase in fluorescence decay time measured for all chronic pancreatitis tissues vs. all normal tissues [69], which was attributed to the longer excited-state lifetime associated with collagen compared to NAD(P)H [36].

4.3 Conclusion

The ability of multi-modal optical spectroscopy to detect signals from pancreatic tissue was demonstrated by studying human pancreatic cancer xenografts in mice and freshly excised human pancreatic tumor tissue for the first time. The EEM matrices measured from human pancreatic cancer xenografts in mice enabled a complete characterization of pancreatic adenocarcinoma tissue and indicated the expected fluorophores in the tissue. The mouse study indicated that 355 nm was an appropriate excitation wavelength to excite fluorescence from the pathologically relevant endogenous fluorophores in the pancreas. Good correspondence was observed between spectra from human pancreatic adenocarcinoma and cancer xenograft tissues. Measured optical spectra and fluorescence decays were correlated with tissue morphological and biochemical properties. The measured spectral features and decay times correlated well with expected pathological differences in human normal, pancreatitis and adenocarcinoma pancreatic tissue states. The observed differences between the fluorescence and reflectance properties of normal,

pancreatitis and adenocarcinoma tissue indicated a possible application of multi-modal optical spectroscopy for differentiating between the three tissue classifications. The next chapter describes the development of tissue classification algorithms employing the multi-modal optical data described in this chapter.

Chapter 5

Development of tissue classification algorithms for the detection of pancreatic adenocarcinoma

A number of chemometric and statistical techniques have been applied to develop tissue classification algorithms employing optical spectroscopy data. These include multiple linear regression analysis, linear discriminant analysis (LDA), neural network analysis, principal component analysis (PCA), logistic discrimination, partial least squares, multivariate linear regression, and support vector machine [4, 7, 19-23].

This chapter describes the development of the first ever algorithms for pancreatic tissue classification using multi-modal optical spectroscopy data [70, 73, 74]. In this dissertation, LDA was employed to classify pancreatic tissues using classification variables extracted from the measured optical reflectance and fluorescence data described in Chapter 4. Two different tissue classification algorithms were developed based on the classification variables [70, 73, 74]. The first was the SpARC (spectral areas and ratios classifier) algorithm that employed ratios of intensities at different wavelengths and areas under the measured spectral curves, thus using information only at specific wavelengths[70]. The second algorithm was the principal component analysis (PCA) algorithm that employed diagnostically relevant information at all wavelengths of the spectra for tissue classification [73]. The PCA algorithm was also employed on the

limited data set of time-resolved fluorescence spectra (described in Section 4.2.1). Section 5.1 of this chapter introduces LDA. Section 5.2 describes the SpARC algorithm, presents the results of the algorithm's classification performance, and compares it with that of EUS-FNA, the current accepted diagnostic standards for pancreatic adenocarcinoma (discussed in Section 1.2.1). Section 5.3 describes the development of the tissue classification algorithm employing PCA and LDA and reports the performance of the PCA algorithm for pancreatic tissue classification. Section 5.3 also discusses a framework for automated detection of pancreatic adenocarcinoma using multi-modal optical spectroscopy and the developed PCA algorithm and makes a comparison of the PCA algorithm performance with EUS-FNA.

5.1 Linear discriminant analysis

Linear discriminant analysis (LDA) [20, 75-77] is a classification technique in which a classification score (Z) is calculated based on a linear combination of the classification variables (V_i).

$$Z = b + a_1V_1 + a_2V_2 + \ldots\ldots + a_kV_k. \qquad \textbf{- 5.1}$$

Where, k is the number of classification variables, and b and a_i are the coefficients calculated such that the distance between the classification scores of the same group is minimized, while maximizing the distance between the classification scores of different groups.

An unknown specimen could then be classified into a group based on it's proximity to the centroid of the classification score of that group. For a two group problem, this proximity can either be measured by deciding a cut-off point (i.e. $Z >$ cut-off implies belongs to group 1, else group 2) or by calculating the probabilities of the unknown specimen

belonging to a group given that a score Z was obtained using the LDA model. The specimen would then be classified as belonging to the group for which the probability is highest.

The LDA model for classification can be developed either by employing all variables specified by the user (Direct LDA) or the set of variables that provide the best classification can be selected from the given variables using selection criterion (for example, Wilks' Lambda (Λ) criterion) that assess the discriminating power of the variables. The latter DA is called a stepwise DA. At each step, variables are considered for the classification algorithm only if the p-value (representing the discrimination added by the variable) satisfies the P-to-enter significance criterion (set by the user). Out of those variables, the variable that minimizes Λ is selected. At the next step, all variables that have already entered the algorithm are re-assessed to see if any of them no longer sufficiently discriminate between the classification groups (measured by a P-to-remove value). This is repeated until no variables satisfy the P-to-enter criterion. The variables retained at the end by the stepwise analysis are then employed to classify the data.

5.2 Spectral areas and ratio classifier (SpARC) algorithm

The SpARC algorithm was developed based on the differences in the fluorescence and reflectance spectra of normal, chronic pancreatitis, and adenocarcinoma human pancreatic tissue types (Figure 4.6 in Chapter 4). The adenocarcinoma sites showed markedly higher reflectance than chronic pancreatitis and normal tissue sites between 450 to 540 nm, higher fluorescence at around 400 nm, and lower fluorescence between 450 to 700 nm. Due to the *ex vivo* nature of the study, it is difficult to draw conclusions on differing hemoglobin absorption between tissue types. The observed spectral differences

are consistent with increased cellular nuclear size and collagen content in pancreatic adenocarcinoma tissues [72]. To classify the tissue spectra based on these apparent differences, the ratio $R_{ratio} = R_{470}/R_{650}$ was calculated for each reflectance spectrum, the wavelength integrated fluorescence (F_{area}) was calculated as the area under each normalized fluorescence spectrum, and the ratio $F_{ratio} = F_{400}/F_{600}$, was calculated for each normalized fluorescence spectrum.

Three different sets of these calculated spectral parameters ("classification variables") were employed to develop tissue classification algorithms for distinguishing (a) adenocarcinoma (A) from chronic pancreatitis (P) and normal (N) tissue, (b) A from P tissue, (c) A from N tissue, and (d) P from N tissue. A leave-one-out cross-validation was undertaken to test the performance of the proposed tissue classification algorithms by considering each measured spectrum as the test data and by employing the remaining spectra as training data in the classification algorithm. LDA was employed using SPSS software to classify the test data using the three different sets of classification variables. This process was repeated for each spectrum and the sensitivity, specificity, negative predictive value (NPV), and positive predictive value (PPV) of the classification algorithms were calculated.

5.2.1 Classification performance of the SpARC algorithm and comparison to EUS-FNA

The first classification algorithm, RSpARC (reflectance spectral areas and ratios classifier), employed R_{ratio} as the sole classification variable for LDA and Table 5.1 gives the algorithm's performance. The second algorithm, FSpARC (fluorescence spectral

areas and ratios classifier), employed F_{area} and F_{ratio} as the classification variables for LDA and Table 5.2 gives that algorithm's performance.

In the third algorithm, SpARC (spectral areas and ratios classifier), stepwise LDA was performed (as described in Section 5.1) using minimization of Wilks' Lambda (Λ) criterion (P-to-enter 0.085; P-to-remove 0.1) to assess the discriminating power of the variables and to select the best set of variables from R_{ratio}, F_{area}, and F_{ratio} for classification [77]. The variables retained by the stepwise analysis were employed to classify the data. Table 5.3 shows the performance of this algorithm along with the variables retained for each classification. For example, classification of A vs. (P and N) employed R_{ratio} and F_{ratio}.

Table 5.1. RSpARC algorithm - reflectance only [70]

Tissue Type	Sensitivity (%)	Specificity (%)	NPV (%)	PPV (%)
A vs. P and N	85	86	92	76
A vs. P	85	83	87	80
A vs. N	88	95	84	97
P vs. N	56	82	50	85

Table 5.2. FSpARC algorithm - fluorescence only [70]

Tissue Type	Sensitivity (%)	Specificity (%)	NPV (%)	PPV (%)
A vs. P and N	55	89	79	72
A vs. P	52	88	69	77
A vs. N	58	91	59	90
P vs. N	56	64	44	74

Table 5.3. SpARC algorithm - reflectance and fluorescence [70]

Tissue Type	Sensitivity (%)	Specificity (%)	NPV (%)	PPV (%)
A vs. P and N[a,b]	85	89	92	80
A vs. P[a]	85	83	87	80
A vs. N[a]	88	95	84	97
P vs. N[a,c]	61	73	50	81

Classification parameters a: R_{ratio} ; b: F_{ratio} ; c: F_{area}

For A vs. (P and N) and P vs. N classification, the combination of classifiers extracted from both reflectance and fluorescence (Table 5.3) performed better than using information from either just reflectance (Table 5.1) or just fluorescence (Table 5.2), indicating that for the SpARC algorithm, bi-modal optical spectroscopy with both fluorescence and reflectance is required for accurate pancreatic tissue classification. Based on the results in Table 5.3, a potential method for classifying an unknown tissue site could employ R_{ratio} and F_{ratio} to classify the data set as adenocarcinoma or not adenocarcinoma using LDA. If the data is classified as not cancer, then R_{ratio} and F_{area} could be employed to classify it as chronic pancreatitis or normal tissue types.

Hartwig *et al.* [30], conducted a meta-analysis of 28 EUS-FNA studies, and reported median (range) values of sensitivity 83% (54 -96%); specificity 100% (71-100%); NPV 72% (16-92%); and PPV 100% (92-100%) for adenocarcinoma distinction from normal tissue and chronic pancreatitis. The performance of the SpARC algorithm for adenocarcinoma distinction from normal tissue and chronic pancreatitis (Table 5.3, row 1) is comparable to that of the reported performance of EUS-FNA. Fritscher-Ravens *et al.* [31] studied patients having both adenocarcinoma and pancreatitis and reported that EUS-FNA had a 54% sensitivity, 100% specificity, 91% NPV, and 100% PPV for

distinguishing adenocarcinoma from pancreatitis in the setting of pancreatitis. All adenocarcinoma measurements in the study reported here were also made on pancreata that had concurrent histologic pancreatitis in addition to the carcinoma. Thus, the sensitivity of SpARC (85%) (Table 5.3, row 2) is well above that of EUS-FNA (54%) [31] at distinguishing adenocarcinoma from pancreatitis in the setting of pancreatitis, which is an unmet clinical need in pancreatic cancer detection. The receiver operating curves (ROC) for A vs. (P and N) (area 0.901 ± 0.043) and A vs. P (area 0.874 ± 0.047) classification using the SpARC algorithm were calculated using SPSS software and are shown in Figure 5.1. The blue line suggests that in achieving a specificity of close to 100%, the A vs. P sensitivity would be comparable to EUS-FNA. Thus, employing an optical technique to guide EUS-FNA could improve the sensitivity of pancreatic adenocarcinoma detection in the setting of pancreatitis.

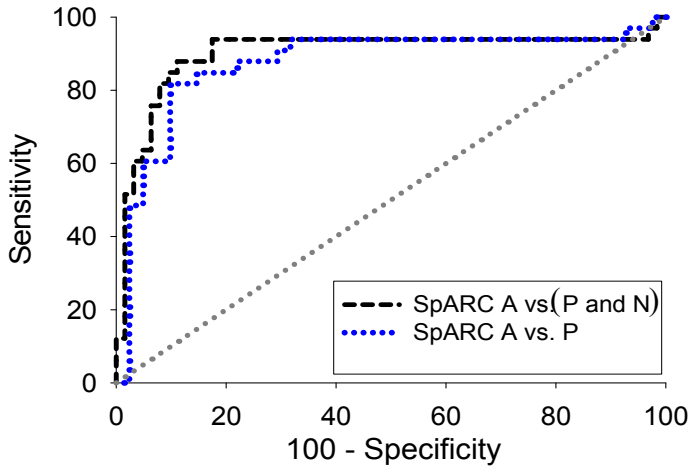

Figure 5.1 The receiver operating curves (ROC) for A vs. (P and N) (black, dashed line) and A vs. P classification (blue, dotted line) using the SpARC algorithm, where the areas under the ROCs were 0.901 ± 0.043 and 0.874 ± 0.047, respectively [70]. The gray dotted line indicates the line of no discrimination.

Although the SpARC algorithm is simple to implement, its performance may be limited because it utilizes information at only select wavelengths. Section 5.3 describes the development and classification performance of a PCA algorithm that employed diagnostically relevant information at all wavelengths for classification.

5.3 Principal component analysis (PCA) algorithm

In this algorithm, principal component analysis (PCA) was used to identify the diagnostic features in the spectra and then LDA was employed to classify the data based on these features. PCA and LDA analyses were also conducted on a subset of the data that included time-resolved fluorescence decay measurements in addition to spectral measurements (subset defined in Section 4.2.1).

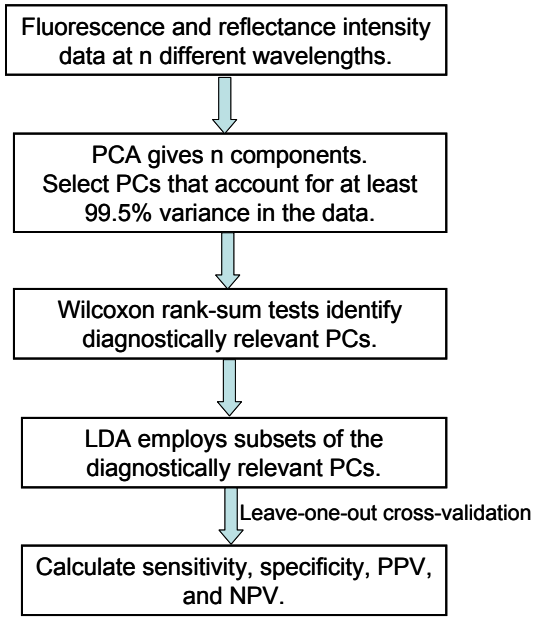

Figure 5.2 Steps in the PCA tissue classification algorithm development [73]. (PCA: principal component analysis; PC: principal component; LDA: linear discriminant analysis; PPV: positive predictive value; NPV: negative predictive value)

Figure 5.2 illustrates the steps involved in the tissue classification algorithm development. The acquired spectra were first analyzed using PCA. The principal components (PCs) that accounted for at least 99.5% of the variance in the data were then identified. Wilcoxon rank-sum tests were performed on the fit-coefficients of these PCs for each tissue type to identify the diagnostically relevant PCs as described in Section 5.3.1. Linear discriminant analysis was then undertaken using various subsets of the diagnostically relevant PCs (Section 5.3.2) to classify the spectral data employing leave-one-out cross validation. These procedures are detailed below.

5.3.1 Principal component analysis of the spectra

PCA was employed to express each measured spectrum as a linear combination of a set of orthogonal basis vectors (or principal components (PC)) [4, 7, 19, 21, 78, 79]. The spectra $\bar{s}_i \in R^{n\times 1}$ (i = 1 to m) for different tissue types were grouped together and arranged row-wise in a matrix $S \in R^{m\times n}$ as shown below:

$$S = \begin{bmatrix} \bar{s}_1^T \\ \bar{s}_2^T \\ \vdots \\ \bar{s}_m^T \end{bmatrix} = \begin{bmatrix} \bar{s}_1^T \\ \vdots \\ \bar{s}_p^T \\ \vdots \\ \bar{s}_{p+q}^T \\ \vdots \\ \bar{s}_{p+q+r}^T \end{bmatrix}, \qquad \textbf{- 5.2}$$

Where, p, q and r (p+q+r=m) are the number of spectra for adenocarcinoma, chronic pancreatitis and normal pancreatic tissue, respectively. Using PCA, n-dimensional data

set (corresponding to the *n* measured wavelengths) with *m* total spectra was represented as a linear combination of *n* basis vectors as shown below:

$$S^T = CX, \qquad \textbf{- 5.3}$$

Where, T is the transpose operator, $C \in R^{n \times n}$ is the matrix of the *n* principal components, and *X* is a matrix of the fit-coefficients.

$$X = \begin{bmatrix} x_{11} & x_{12} & \cdots & & x_{1m} \\ x_{21} & \ddots & & & \vdots \\ \vdots & & \ddots & & \\ x_{n1} & \cdots & \cdots & \cdots & x_{nm} \end{bmatrix}, \qquad \textbf{- 5.4}$$

Where, an element x_{ji} is the fit-coefficient of the j^{th} component for the i^{th} spectrum.

The principal component matrix *C* was obtained from *S* by employing the *princomp* function in MATLAB. The *princomp* function first calculates matrix S_0 by subtracting the column mean vector from each row of *S*. Then singular value decomposition is used to calculate the principal components as the eigenvectors of the sample covariance matrix ($(m-1)^{-1} S_0^T S_0$). The *princomp* command also calculates the eigenvalues corresponding to each principal component. The columns of *X* were estimated by fitting the principal components to the spectra using an ordinary least squares method (the backslash operator in MATLAB). The vectors of estimated fit-coefficients for each spectrum (*i.e.* the columns of *X*) were then separated into three groups based on the tissue type. This analysis was done separately for both fluorescence ($n = 492$) and reflectance spectra ($n = 521$). Figure 5.3a and Figure 5.3b plot select fluorescence and reflectance PCs extracted from the spectral data.

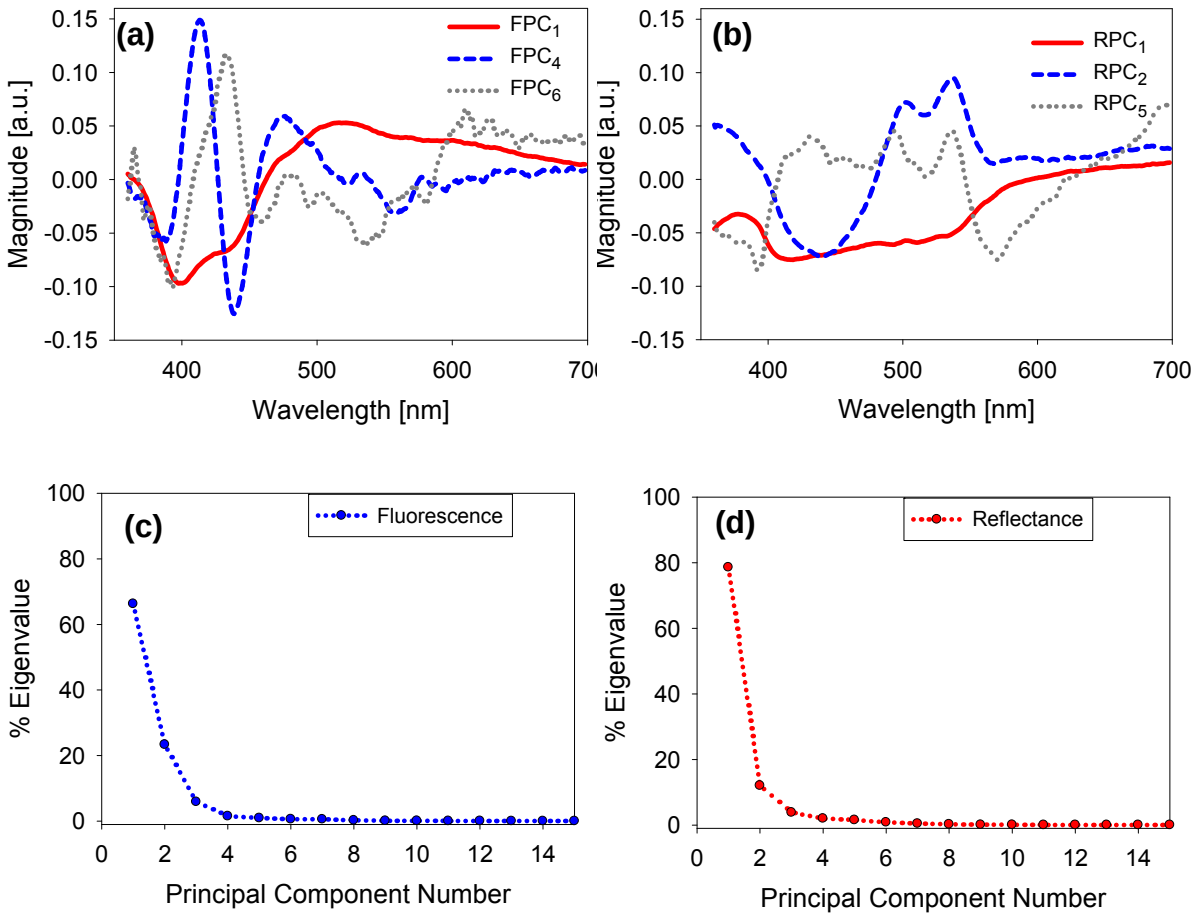

Figure 5.3 Select PCs extracted from (a) fluorescence and (b) reflectance spectra of pancreatic adenocarcinoma, chronic pancreatitis, and normal tissues. The percent eigenvalues of the extracted PCs for (c) fluorescence and (d) reflectance spectra [73].

5.3.2 LDA of diagnostically relevant principal components (PCs)

Key spectral features of the data were captured by only a few of these PCs (having higher eigenvalues), while the vectors corresponding to lower eigenvalues typically represented noise in the data**.** Figure 5.3c and Figure 5.3d plot the percent eigenvalues (or percent variance) of the fluorescence and reflectance PCs. The higher the percent value, the more the corresponding PC explained the variance in the data. However, not all the key

features of the spectra are diagnostically relevant (*i.e.* enabling differentiation between the tissue types). Wilcoxon rank-sum tests were employed to identify the PCs whose fit-coefficients showed differences between tissue types and were thus diagnostically relevant.

The PCs for which the fit-coefficients were significantly different between the tissue types were determined based on a two-sided Wilcoxon rank-sum test ($p < 0.05$). This test was done for the PCs that accounted for at least 99.5% of the variance in the data (Figure 5.3c and Figure 5.3d). The first 11 fluorescence PCs accounted for at least 99.5% of the variance in fluorescence data and the first 8 reflectance PCs accounted for at least 99.5% variance in the reflectance data. Four Wilcoxon rank-sum tests were performed for the fit-coefficients of these PC. The hypothesis tested was that the median fit-coefficients were significantly different for the principal component of: (1) adenocarcinoma (A) vs. the rest of the tissue types; (2) A vs. chronic pancreatitis (P); (3) A vs. normal pancreatic tissue (N); (4) P vs. N. The PCs for which the *p*-values of the Wilcoxon rank-sum tests were less than 0.05 were considered diagnostically relevant. This analysis was done for both fluorescence and reflectance spectra separately to determine the PCs whose fit-coefficients would be used for classification of tissue types: RPC, diagnostically relevant reflectance PC; FPC, diagnostically relevant fluorescence PC. The PCs plotted in Figure 5.3a and Figure 5.3b are some of the diagnostically relevant RPC and FPC we identified in this study.

LDA was employed using SPSS software to distinguish between tissue types using the fit-coefficients of the diagnostically relevant RPC and FPC as classification variables. The analysis was undertaken by employing the fit-coefficients of three different sets of

diagnostically relevant PCs: reflectance PC only, fluorescence PC only, or a combination of the reflectance and fluorescence PC variables. In the latter case, a stepwise DA (P-to-enter ≤ 0.05; P-to-remove value ≥ 0.25) was performed using minimization of Wilks' Lambda (Λ) criterion to assess the discriminating power of the variables and to select the best set of variables from diagnostically relevant RPC and FPC for classification.

A leave-one-out cross-validation was undertaken to test the performance of each of the proposed tissue classification algorithms. For each algorithm, the data were divided into training and test data where each pair of reflectance and fluorescence spectra were considered as test data one at a time, while the remaining spectra were treated as training data. The classifiers were then employed to classify the test data using LDA. Each algorithm was implemented 96 times and sensitivity, specificity, NPV, and PPV were calculated.

5.3.3 PCA and LDA employing time-resolved fluorescence measurements

As described in Section 4.2.1, analysis of the time-resolved fluorescence decay measurements was restricted to a limited data set comprising of 35 chronic pancreatitis and 18 normal tissue measurements. Figure 5.4a plots on a logarithmic scale the mean of the normalized measured time-resolved fluorescence decay curves from these pancreatitis and normal tissue sites. PCA was employed on the normalized time-resolved fluorescence decays of this limited data set with the premise that the shape of the decay curve should reflect changes in decay time for different tissue types, assuming the temporal instrument response did not change. PCA was also employed on the

fluorescence and reflectance spectral data for the same subset of chronic pancreatitis and normal tissue data.

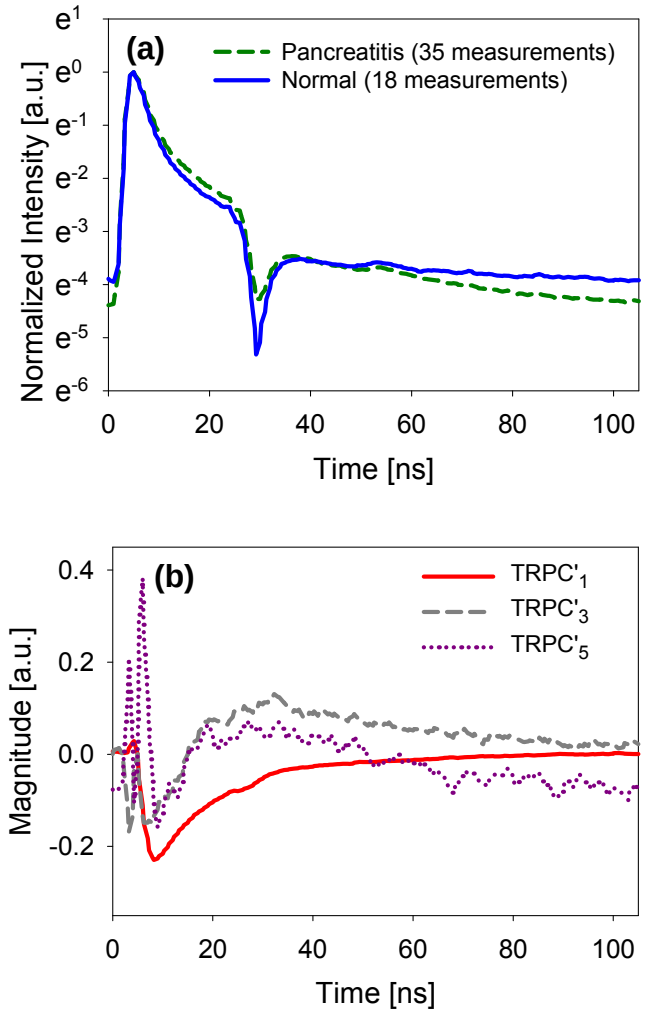

Figure 5.4 (a) The plot of mean normalized time-resolved fluorescence decay, measured from chronic pancreatitis (green dashed line) and normal (blue solid line) pancreatic tissue sites on a logarithmic scale. (b) Select PCs extracted from these time-resolved fluorescence decays [73].

The first 12 fluorescence spectral PCs and first 5 time-resolved fluorescence PCs accounted for at least 99.5% of the variance in the spectral and time-resolved fluorescence data, respectively. The first 7 reflectance PCs accounted for at least 99.5% variance in the reflectance data. The diagnostically relevant spectral fluorescence,

spectral reflectance, and time-resolved fluorescence PCs (FPC′, RPC′, and TRPC′, respectively) were determined as before using Wilcoxon rank-sum tests on these PCs that explained at least 99.5% variance of this limited data set. (The ′ symbol denotes PCs extracted from the limited data set).

A stepwise LDA (*P*-to-enter = 0.09; *P*-to-remove = 0.1) was performed on the fit-coefficients of these diagnostically relevant FPC′s, RPC′s, and TRPC′s, to distinguish between chronic pancreatitis and normal tissue sites. The analysis was undertaken by employing three different sets of diagnostically relevant PCs: only fluorescence and reflectance spectral data PCs, only time-resolved data PCs, or a combination of the spectral and time-resolved data PCs. A leave-one-out cross validation was implemented for each of these sets of PCs and sensitivity, specificity, NPV, and PPV were calculated. Figure 5.4b plots some of the diagnostically relevant TRPC′s extracted from the time-resolved fluorescence data.

5.3.4 Classification performance of the PCA algorithm

5.3.4.1 Classification using fluorescence and/or reflectance spectra

Three different set of classification variables were employed to develop the chemometric tissue classification algorithm: diagnostically relevant fluorescence PCs only, reflectance PCs only, or a combination of the fluorescence and reflectance spectra PCs. Classification results are summarized below.

Classification using fluorescence parameters

Table 5.4 lists the performance of the chemometric algorithm for classifying tissue types using only the diagnostically relevant fluorescence PC. The diagnostically relevant PCs

were identified by Wilcoxon rank-sum tests as described in Section 5.3.2. For example, for distinguishing adenocarcinoma from chronic pancreatitis and normal tissue FPC1, FPC4, FPC6, and FPC11 (some of which are shown in Figure 5.3a) were employed and sensitivity, specificity, NPV, and PPV of 82%, 78%, 89%, and 66%, respectively were achieved.

Table 5.4. Pancreatic tissue classification using fluorescence spectra PCs [73]

Tissue Type	Sensitivity (%)	Specificity (%)	NPV (%)	PPV (%)	Components
A vs. P & N	82	78	89	66	FPC1, FPC4, FPC6, FPC11
A vs. P	79	73	81	70	FPC1, FPC2, FPC11
A vs. N	88	91	83	94	FPC1, FPC4, FPC6,FPC8, FPC9
P vs. N	56	73	47	79	FPC7, FPC8, FPC9

A: adenocarcinoma (33 spectra); N: normal (22 spectra); P: pancreatitis (41 spectra)

Table 5.5. Pancreatic tissue classification using reflectance spectra PCs [73]

Tissue Type	Sensitivity (%)	Specificity (%)	NPV (%)	PPV (%)	Components
A vs. P & N	94	84	96	76	RPC1, RPC2
A vs. P	79	88	83	84	RPC1, RPC2, RPC7, RPC8
A vs. N	94	86	90	91	RPC1, RPC2
P vs. N	78	82	67	89	RPC1, RPC3, RPC5, RPC7, RPC8

A: adenocarcinoma (33 spectra); N: normal (22 spectra); P: pancreatitis (41 spectra)

Classification using reflectance parameters

Table 5.5 lists the sensitivity, specificity, NPV and PPV for classifying tissue types using only the diagnostically relevant reflectance PCs. For example, for distinguishing adenocarcinoma from chronic pancreatitis and normal tissue, LDA was performed on the

fit-coefficients of RPC1, and RPC2 (shown in Figure 5.3b). The classification performance of the algorithm using reflectance PCs only was found to be better at classifying the tissue types than the algorithm using fluorescence PCs only.

Classification using fluorescence and reflectance parameters

The third set of classification variables was comprised of the diagnostically relevant PCs from both fluorescence and reflectance spectra. Table 5.6 lists the sensitivity, specificity, NPV, and PPV for classifying tissue types using both diagnostically relevant fluorescence PCs and reflectance PCs, where a stepwise LDA was performed (as described in Section 5.3.2) to further select classification variables from all the diagnostically relevant fluorescence and reflectance PC listed in Table 5.4 and Table 5.5. The last column in Table 5.6 indicates the PCs selected by the stepwise LDA for the classification procedure. Figure 5.3a and Figure 5.3b show some of the diagnostically relevant PC used for this classification. The results in Table 5.6 indicate that a combination of reflectance and fluorescence PCs has the best sensitivity and specificity for identifying pancreatic adenocarcinoma.

Table 5.6. Pancreatic tissue classification using fluorescence and reflectance spectra PCs [73]

Tissue Type	Sensitivity (%)	Specificity (%)	NPV (%)	PPV (%)	Components
A vs. P & N	91	90	95	83	RPC1, RPC2, FPC1, FPC4, FPC6
A vs. P	82	85	85	82	RPC1, RPC2, RPC8, FPC1
A vs. N	94	86	90	91	RPC1, RPC2
P vs. N	83	86	73	92	RPC1, RPC5, RPC7

A: adenocarcinoma (33 spectra); N: normal (22 spectra); P: pancreatitis (41 spectra)

The receiver operating curves (ROCs) for A vs. (P and N) (area 0.923 ± 0.040) and A vs. P (area 0.908 ± 0.036) classification using the PCA algorithm employing both fluorescence and reflectance parameters were calculated using SPSS software and are shown in Figure 5.5.

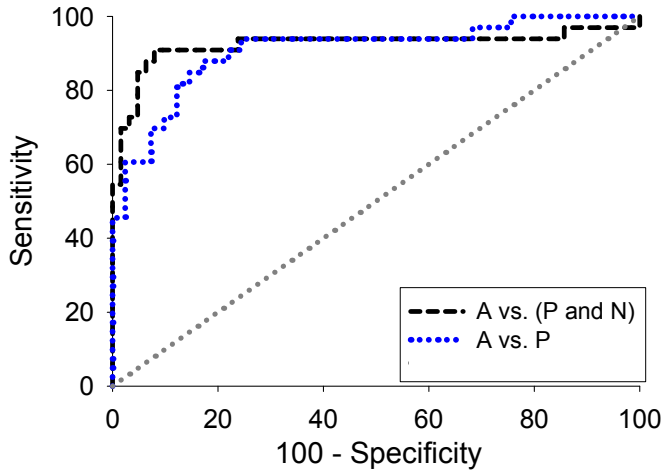

Figure 5.5 The receiver operating curves (ROC) for A vs. (P and N) (black, dashed line) and A vs. P classification (blue, dotted line) using the PCA algorithm, where the areas under the ROCs were 0.923 ± 0.040 and 0.908 ± 0.036, respectively. The gray dotted line indicates the line of no discrimination [73].

5.3.4.2 Inclusion of time-resolved fluorescence data

The effect of including diagnostically relevant time-resolved fluorescence data PCs was evaluated on the limited data set of 18 normal and 35 pancreatitis tissue measurements, as described in Section 4.2.1. Table 5.7 lists the sensitivity, specificity, NPV, and PPV for classifying chronic pancreatitis vs. normal tissue types employing stepwise LDA on: diagnostically relevant fluorescence and reflectance spectral data PCs only (results in row 1), time-resolved data PCs only (row 2), or a combination of the spectral and time-resolved data PCs (row 3). For example, for distinguishing chronic pancreatitis from normal tissue using time-resolved data PCs only, the stepwise LDA employed the fit-

coefficients of TRPC′1, TRPC′3, and TRPC′5 (shown in Figure 5.4b). The results of this analysis on the limited data set indicated that using a combination of both spectral and temporal information (results in row 3 of Table 5.7) significantly improved the classification performance of the chemometric algorithm for distinguishing pancreatitis from normal pancreatic tissue (compared to row 4 of Table 5.6).

Table 5.7. Chronic pancreatitis vs. normal pancreatic tissue classification using spectral and/or temporal PCs [73]

Tissue Type	Sensitivity (%)	Specificity (%)	NPV (%)	PPV (%)	Components
P vs. N	80	83	68	90	RPC′1, RPC′5, RPC′7, FPC′9
P vs. N	80	89	70	93	TRPC′1, TRPC′3, TRPC′5
P vs. N	89	100	82	100	RPC′1, RPC′5, RPC′7, FPC′9, TRPC′5

N: normal (18 measurements); P: pancreatitis (35 measurements)

5.3.4.3. Framework for automated clinical detection of pancreatic disease using optical spectroscopy and the PCA algorithm

The results in Table 5.6 showed that a combination of reflectance and fluorescence parameters had the best sensitivity, specificity, and PPV for identifying adenocarcinoma. In addition, the NPV of 95% was nearly identical to 96% for algorithm employing RPCs only. Based on these results, data from an unknown tissue site could be classified in a two-step chemometric algorithm as illustrated in Figure 5.6. First, the test data could be classified by employing RPC1, RPC2, FPC1, and FPC4, FPC6 into ‘adenocarcinoma’ or ‘not adenocarcinoma’. If the data is classified as ‘not adenocarcinoma’ then, if needed, RPC1, RPC5, and RPC7 could be employed to further classify the data into ‘normal’ or ‘chronic pancreatitis’. Employing PCA and LDA on the limited time-resolved

fluorescence data set indicated improved classification of chronic pancreatitis vs. normal tissue with the use of both spectral and time-resolved data. If this result holds true in a larger data set, as well, then time-resolved fluorescence PCs could also be included in the classification algorithm.

Our results suggest that using the optical technique in conjunction with EUS-FNA could significantly improve the sensitivity of pancreatic adenocarcinoma detection in the setting of chronic pancreatitis. In a clinical setting, such a chemometric classification procedure could be undertaken in a few seconds, giving a quick, automated classification scheme either to guide EUS-FNA procedures or to improve tumor margin detection during pancreatic surgery.

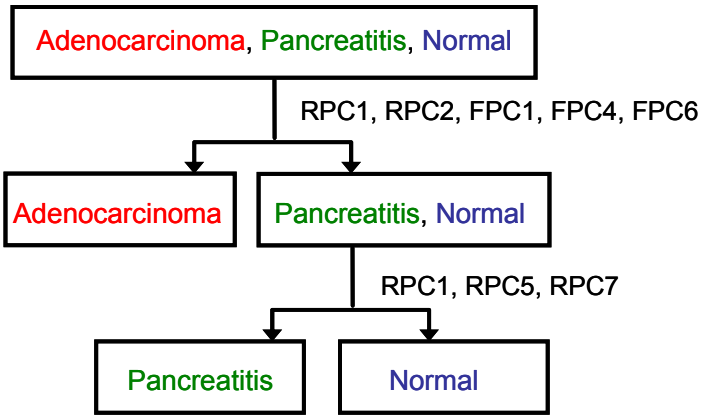

Figure 5.6 The proposed tissue classification algorithm schematic for unknown data.

5.3.4.4 Comparison of the developed PCA algorithm with current diagnostic standard, EUS-FNA

As mentioned previously, EUS-FNA has median (range) values of 83% (54 -95%) sensitivity, 100% (71-100%) specificity, 72% (16-92%) NPV, and 100% (92-100%) PPV, for adenocarcinoma identification according to a recent meta-analysis of 28 studies that employed EUS-FNA [30]. The maximum sensitivity, specificity, NPV, and PPV of

the developed optical tissue classification PCA algorithm for correctly identifying adenocarcinoma were 91%, 90%, 95%, and 83%, respectively. Thus, the classification performance of the developed optical algorithms for adenocarcinoma identification is comparable to the reported performance of EUS-FNA. In the setting of pancreatitis, *i.e.* when the patient has both adenocarcinoma and chronic pancreatitis, EUS-FNA has a reported sensitivity, specificity, NPV, and PPV of 54%, 100%, 91%, and 100% respectively [31] for distinguishing adenocarcinoma from chronic pancreatitis. The sensitivity is unacceptably low, being only slightly better than the outcome of a coin toss. All adenocarcinoma measurements in the study reported here were also made on pancreata that had concurrent histologic pancreatitis in addition to the carcinoma. For distinguishing adenocarcinoma from chronic pancreatitis, the PCA algorithm had a sensitivity, specificity, NPV, and PPV of 82%, 85%, 85%, and 82% respectively. Thus, the sensitivity of the optical PCA algorithm is well above that of EUS-FNA, indicating a decreased likelihood of obtaining false negative results. Our results suggest that using the optical technique in conjunction with EUS-FNA could significantly improve the sensitivity of pancreatic adenocarcinoma detection in the setting of chronic pancreatitis. In a clinical setting, such a classification procedure could be undertaken in a few seconds, giving a quick, automated classification scheme either to guide EUS-FNA procedures or to improve tumor margin detection during pancreatic surgery.

Chapter 6

Non-invasive characterization of tissue engineered devices using optical spectroscopy

Tissue engineered constructs are functional biologic devices employed for grafting wounds or replacing diseased tissue. Non-invasive methods are required to assess the viability of these engineered constructs. In this chapter, the prospect of employing the developed optical spectroscopy instrumentation and previously developed Monte Carlo (MC) simulations to non-invasively and quantitatively investigate endogenous optical signals from tissue engineered devices was assessed. The methods developed in this chapter have the significant advantage of being safe for clinical human use as they employ endogenous contrast.

In Section 6.1, a method to non-invasively and quantitatively characterize thick biological tissues by combining experimental and computational approaches in tissue optical spectroscopy was developed and validated on porcine articular cartilage (AC) tissue samples [13, 56]. This work and the methods developed here should aid in the future study of AC tissue constructs. To the best of our knowledge, this study is the first to couple non-invasive reflectance and fluorescence spectroscopic measurements on freshly harvested tissues with MC computational modeling of time-resolved propagation of both excitation light and multi-fluorophore emission. Section 6.1.1 describes the

histology and sample preparation of the porcine AC samples measured in this study. Sections 6.1.2 and 6.1.3 describe the fluorescence and reflectance spectra and time-resolved fluorescence decay measurements made on porcine AC. Section 6.1.4 describes the extraction of tissue optical properties of AC and Section 6.1.5 describes the MC simulations that were run using these tissue optical properties. Section 6.1.6 then presents the results of the optical measurements and simulations and introduces a method to couple the two for non-invasive assessment of tissues using endogenous contrast agents.

Section 6.2, presents the work done in this dissertation to optimize non-invasive optical assessment of cell viability in *ex vivo* produced oral mucosa equivalent (EVPOME) constructs [80]. In this work, fluorescence spectral measurements and Monte Carlo simulations were executed for the first time to characterize the optical signatures in EVPOME and to optimize fluorescence signal form the cellular component of EVPOME in order to assess the viability of the constructs pre- and post- implantation into patients. Section 6.2.1 describes the manufacturing procedure and histology of EVPOME constructs and Section 6.2.2 discusses the expected fluorescence optical signatures in an EVPOME construct. Section 6.2.3 describes the MC simulations of photon transport in EVPOME constructs executed at 355 nm and 450 nm excitation for different source-detector fiber geometries. The Section also describes the tissue optical properties and fluorophore optical properties employed as inputs to the MC simulations. Section 6.2.5 describes measurement of EVPOME constructs employing the reflectance and fluorescence lifetime spectrometer (RFLS). Section 6.2.6 presents the results of the MC simulations and experimental measurements. Section 6.2.7 concludes the chapter with a discussion of the results obtained and possible future directions for the study.

6.1 Porcine articular cartilage (AC): towards the assessment of AC constructs

6.1.1 Porcine knee articular cartilage (AC) sample preparation

Hyaline AC is found in the synovial joints and is composed of chondrocytes surrounded by extracellular matrix, which is mainly composed of tissue fluid (80% water) and a macromolecular framework composed of collagens (mainly collagen type II, 90% – 95%), proteoglycans, and non-collagenous proteins and glycoproteins [45]. Figure 6.1 shows a micrograph of porcine knee AC tissue made by using an antibody based immunochemical stain (C7510-20F, United States Biological, Swampscott, MA) that specifically stains collagen type II in brown color. Cells and remaining tissue components not containing collagen type II appeared green in the figure.

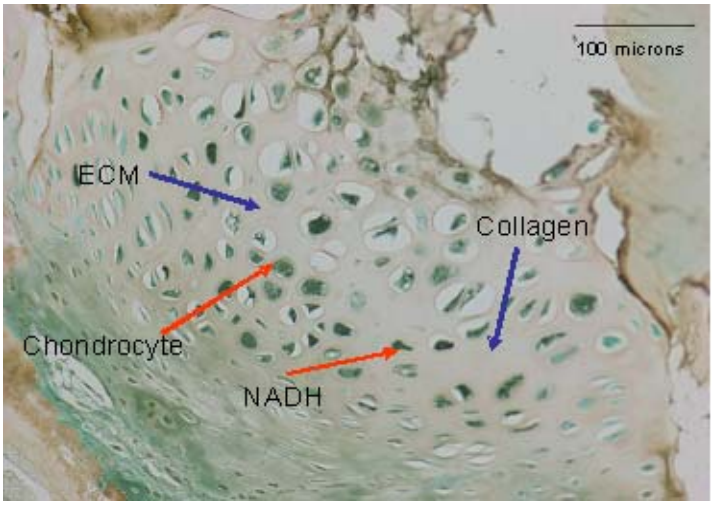

Figure 6.1 Immunohistochemical staining for collagen type II (brown) found in the extracellular matrix (ECM) (blue arrows) of porcine knee articular cartilage (AC) [56]. Red arrows indicate cells (chondrocytes) where NADH is found.

Sixteen porcine knee AC samples (approximately 1-2 mm in thickness) were either freshly harvested (with measurements done 1-2 hours after harvesting) or cultured in culture media composed of Dulbecco's modified Eagle's medium (11995-065, Gibco/Invitrogen, Carlsbad, CA) + 10% fetal bovine serum (16000-044, Gibco/Invitrogen) + 1% penicillin/streptomycin (15140-122, Gibco/Invitrogen) for 1 week before measurements were taken. These two groups of samples were employed to determine whether culturing would affect tissue optical response. No marked differences were observed between the two groups. All samples were washed in phosphate-buffered saline (Cat. No.110010-023, Invitrogen) to remove traces of blood and cell culture media, placed on 0.88 mm thick quartz microscope slides (01018-AB, Structure Probe Inc., West Chester, PA) and sealed inside imaging chamber gaskets (C-18160, Invitrogen) for experimental measurements. Two of the samples (cultured) were used to extract tissue scattering and absorption coefficients via integrating sphere (IS) measurements (described in Section 6.1.4). The remaining fourteen samples were employed for steady-state and time-resolved fluorescence measurements. Reflectance measurements were performed on eleven out of these fourteen samples and a fluorescence excitation-emission matrix (EEM) was acquired using one of the other three samples (as described in Section 6.1.2).

6.1.2 Spectrofluorimetry

A spectrofluorometer (SPEX® FL3-22 Fluorolog-3, Jobin-Yvon Horiba, Japan) was employed to measure the EEM for AC tissue. Details of the Fluorolog-3 spectrofluorometer can be found in Section 4.1.3. The AC sample was front illuminated to obtain the EEM for 25 excitation wavelengths between 320 and 450 nm while

monitoring the emission between 340-650 nm (at 1 nm increments). Data acquisition time was approximately 6 minutes.

6.1.3 Reflectance, steady-state fluorescence and fluorescence lifetime spectrometer measurements

The Reflectance and Fluorescence Lifetime Spectrometer (RFLS) described in Chapter 3 was employed to measure reflectance and fluorescence spectra and time-resolved fluorescence decays from AC tissues. Light from the fluorescence laser and reflectance lamp sources were delivered to the sample via two identical optical fibers (fluorescence and reflectance source fibers) (SFS600/660N, Fiberguide Industries, Stirling, NJ) of 600 μm core diameter and 0.22 numerical aperture (NA). At the distal end, the fiber probe was comprised of these two source fibers and a third, identical detector fiber placed adjacent to each other in a triangular geometry (as shown for the probe in Figure 3.1). Fluorescence and reflectance measurements were acquired sequentially.

For reflectance measurements, the LP and ND2 filters in Figure 3.1 were removed and the optical signal from the sample was sent via the detector fiber and focusing optics directly to the spectrograph-coupled ICCD camera. The ICCD camera was run in its internal mode (i.e. the gate was open throughout data acquisition) and room lights were turned off to minimize background signal.

For fluorescence and reflectance measurements, a background spectrum was acquired with the sources blocked and was subtracted from the detected sample spectrum. Background subtracted data were then corrected to give distortion free spectra in units of photon numbers by calibrating the wavelength and correcting for the spectral instrument response of the RFLS. Details of these calibration procedures were described earlier in

Section 3.4 of Chapter 3 [67]. Reflectance spectra were also corrected for the intensity spectrum of the lamp. First, the lamp spectrum was measured by placing a ND filter of OD 0.03 (03FNQ002, Melles Griot, Rochester, NY) in lieu of the tissue sample. Next, the background subtracted and instrument response corrected tissue sample reflectance spectrum (R_{sample}) was divided by the background subtracted and instrument response corrected lamp spectrum (R_{lamp}), to give the reflectance spectrum (R) from each AC tissue sample (i.e. $R = R_{sample} / R_{lamp}$).

In this study, all measurements were taken with the fiber optic probe oriented normal to, and at a slight distance (0.5-1.0 cm) above, the AC tissue surface to mimic likely experimental conditions for studies on sterile samples. Reflectance spectra were measured keeping the ICCD gate open for 380 μs and steady-state fluorescence spectra were measured by averaging over 1600 pulses (1.6 s integration time). For fluorescence measurements, laser pulse energy was attenuated using an ND1 filter of optical density (OD) 1.0 (03FNQ015, Melles Griot).

Three set of time-resolved fluorescence measurements were made on each sample: one full spectrum measurement (using the LP filter) and two wavelength-selected measurements (using BP filters (centered at 400 and 540 ± 10 nm) in place of the LP filter). All time-resolved fluorescence measurements were collected by averaging over 50 pulses. All measured fluorescence decays *M(t)* were interpreted as a convolution of the intrinsic fluorescence decay, *f(t)*, and the instrument response function, *I(t)* [67], where *f(t)* was modeled as a double exponential decay: $f(t) = \sum c_i \exp(-t/\tau_i)$, ($i$ = 1,2) because the AC tissue was considered to be composed of a long-lived (collagen) and a short-lived

(NADH) fluorophore. The average decay time τ, was calculated as $\tau = [(c_{1*} \tau_1^2 + c_{2*} \tau_2^2)/(c_{1*} \tau_1 + c_{2*} \tau_2)]$.

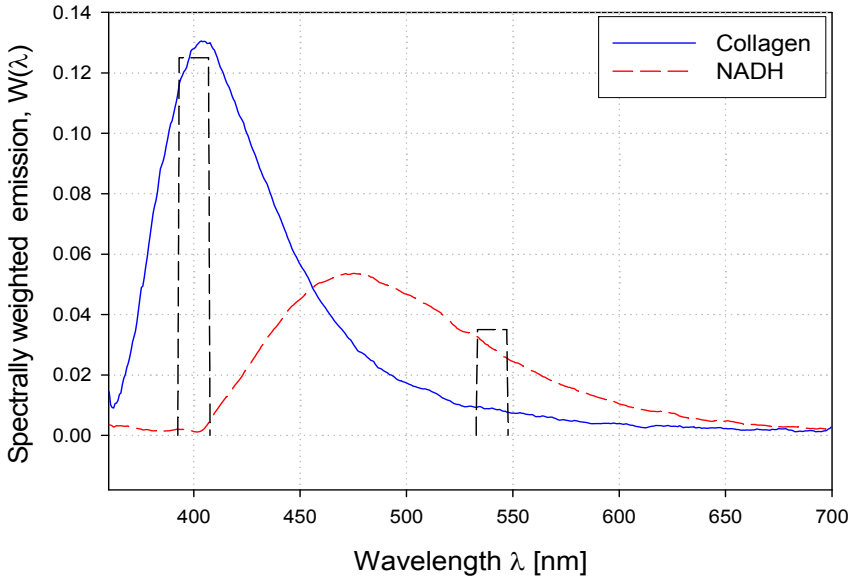

Figure 6.2 Spectrally weighted fluorescence emission *W(λ)* (see text) for two fluorophores in the AC tissue [56]. These spectra were measured on the RFLS for powdered collagen II (blue line) and for 70 μM NADH in DI-H_2O (red dashed line). The black dashed lines indicate the spectral position of band-pass filters that were employed for obtaining time-resolved fluorescence measurements from porcine AC samples.

Figure 6.2 shows the spectral positions of the BP filters (black dashed lines) relative to the spectrally weighted fluorescence emission *W(λ)* of collagen (blue line, solid) and NADH (red line, dashed). These fluorescence emission spectra were acquired on the RFLS from NADH (N-8129, Sigma Aldrich) in DI-H_2O (70 μM) and collagen type II (C-1188, Sigma Aldrich) in powder form. In order to calculate *W(λ)* each measured fluorescence spectrum was normalized by setting the maximum fluorescence emission intensity to unity (thus getting rid of fluorophore concentration effects), then scaled such that area under each curve was unity, and finally multiplied by the quantum yield (Φ_{QY})

of the corresponding fluorophore (0.15 for collagen and 0.1 for NADH obtained from literature [36, 81, 82]). As seen in Figure 6.2, at BP 400 nm, collagen dominated the fluorescence emission relative to NADH, while at BP 540 nm, this was reversed. Thus, the effects of the changes in the measured fluorescence decays from a medium containing these two fluorophores (NADH and Collagen II), obtained via these two BP filters could be quantitatively modelled using a Monte Carlo model (described below in Section 6.1.5 below).

6.1.4 Integrating sphere measurements

Tissue scattering and absorption coefficients (μ_s and μ_a, respectively) were determined using an integrating sphere (IS) and the inverse adding-doubling (IAD) method [83]. The adding-doubling method models random scattering events in a planar sample by approximating the sample as a discrete number of scattering layers and scattering angles. The IAD method used iteration to fit the measurements, and was implemented using IAD software available online [84]. The method required separate measurements of diffuse reflectance, diffuse transmittance, and collimated transmittance as illustrated in Figure 6.3. A CW tungsten halogen lamp (LS-1, Ocean Optics) emitting light between 360-2000 nm with a 200 micron fiber coupling was used for all measurements.

Two cultured AC tissue samples, each with overall thickness 1.2 mm, were measured. For diffuse reflectance measurements, the light source was attached to the reflectance port (Port 3) of an integrating sphere (Avasphere-30, Avantes, Boulder, CO) (Figure 6.3a). The sample was placed at the sample port (Port 1, 8 mm diameter) and the collimated light formed a spot size approximately 5 mm in diameter on the sample. The sum of intensity of diffuse and specular reflected light was measured using a

spectrometer (USB-2000, Ocean Optics) coupled to the IS with a 600 micron core fiber at the detection port (Port 2). Integration times varied from 4-60 seconds. Reflectance measurements were calibrated using a 75% reflectance standard (SRS-75-010, Labsphere, North Sutton, New Hampshire).

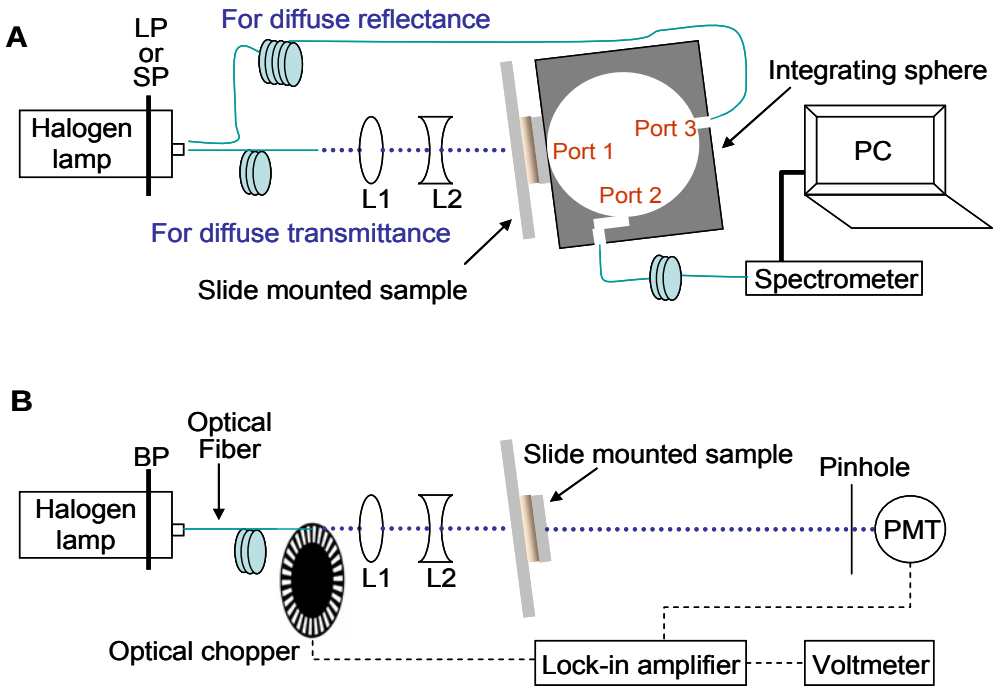

Figure 6.3 (a) Schematic for diffuse reflectance and transmittance measurements using an integrating sphere. (b) Schematic for collimated transmittance measurements. (L- Lens; LP – long-pass filter; SP – short-pass filter; BP – band-pass filter; PMT – photomultiplier tube; Port 1 – sample port; Port 2 – detection port; Port 3 – reflectance port) [56].

Diffuse transmittance measurements (Figure 6.3a) were taken by collimating the fiber coupled light source by a lens pair (L1 and L2) to form a spot size approximately 4 mm in diameter at the sample. For this measurement, the IS was tilted to prevent collimated transmitted light from falling on the uncoated portion of the sphere at the reflectance port. Two set of diffuse reflectance and transmittance spectra were taken - for source

wavelengths less than, and greater than 420 nm - by placing appropriate filters (SP or LP) in front of the lamp. This reduced the number of photons hitting the spectrograph detector and avoided saturation of the detector.

For collimated transmittance measurements (Figure 6.3b) the IS and spectrometer were removed and a photomultiplier tube (PMT) (R928, Hamamatsu) was employed for light detection. A pinhole placed in front of the PMT limited the acceptance angle to 0.17 degrees to eliminate fluorescent and diffuse light. An optical chopper (SR540, Stanford Research Systems) and lock-in amplifier (LIA-MV-150, Femto, Berlin, Germany) were employed to increase sensitivity. Measurements were taken for 9 wavelengths by placing narrowband (nominally 10 nm full width at half maximum) band-pass (BP) filters at the source (Table 6.1). Transmittance measurements were calibrated using ND filters of OD 1.0 (03FNQ015, Melles Griot) and OD 3.0 (03FNQ027, Melles Griot).

6.1.5 Monte Carlo model for photon migration simulations

An MC transport code [16] was used to simulate both time-resolved reflectance and fluorescence from an AC tissue model (Figure 6.4). The AC tissue model was a bulk medium (0.12 cm thickness) containing two uniformly distributed fluorophores (intracellular NADH and collagen type II in the extracellular matrix). 2.5×10^7 photons were launched into the tissue model normal to the surface, at the air-tissue interface via a source optical fiber of specified numerical aperture (0.22) and diameter (600 microns core). Reflectance and fluorescence escaping the tissue per unit time was collected at surface within detector annuli concentric with the source fiber. The spacing between consecutive (detection) rings was identical and set equal to source fiber diameter. As described in Section 2.2, photon trajectories (black lines, Figure 6.4) were constructed by

stochastic sampling of scattering angles (specified by the anisotropy coefficient, g) and path lengths (specified by the scattering coefficient, μ_s). Each photon entered the tissue medium with a weight of unity, which was attenuated exponentially as given by Beer's law for the absorption coefficient μ_a of the medium. After each scattering step, a new direction for the photon trajectory was calculated via the scattering phase function (the Henyey-Greenstein function [62]), which is specified by the anisotropy coefficient (g) of the tissue. The flight of the photon ended when it left the tissue (by crossing the tissue-air interface) or when its weight fell below a threshold minimum value (set to $1x10^{-5}$), as determined by a Russian roulette routine [62]. At the end of its travel in the tissue, the time, t, spent by the photon within the medium was given by $t = L/nc$, where L is the total path-length of the photon, c is the speed of light in vacuum, and n is the refractive index of the medium [63].

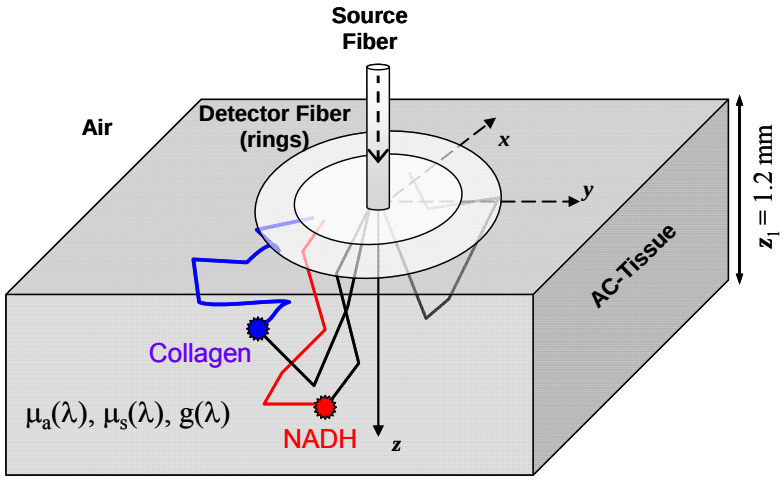

Figure 6.4 Model for articular cartilage tissue showing fluorescence from two uniformly distributed fluorophores (intracellular NADH and extracellular collagen) relative to the excitation-detection fiber probes, as simulated by the MC code) [56].

For the two-fluorophore AC tissue model studied here, the simulation supported tissue models containing $N_f = 2$ fluorophores (emitting at N_f different wavelengths) that were considered to be uniformly distributed in the tissue medium [85]. The incident excitation could be absorbed by any one of the N_f fluorophores. After each scattering event of the excitation photon, fluorescence absorption was sampled using a rejection technique, as governed by a cumulative fluorescence absorption coefficient M_{af}. Here, M_{af} was the sum of the fluorescence absorption coefficients (μ_{afx}) of all N_f fluorophores specified in the tissue model, i.e. $M_{af} = \Sigma^i \mu_{afx}$ ($1 \leq i \leq N_f$). Once it was determined that the photon had been absorbed to produce a fluorescence photon, the wavelength of the remitted fluorescence photon was selected by a MC routine, where the probability of absorption of the excitation photon by one of the N_f fluorophores was equal to the ratio ${}^i\mu_{afx} / M_{af}$ ($1 \leq i \leq N_f$) [85]. Upon successful fluorescence absorption, the excitation photon was relabeled a fluorescence photon, its new direction of travel was determined by an isotropic scattering event, and its weight was multiplied by the fluorescence quantum yield, ${}^i\Phi_{QY}$. This newly created fluorescence photon then continued to propagate from the point of its spatial origin (blue lines - collagen type II, red lines – NADH in Figure 6.4), as governed by the scattering, absorption, and anisotropy coefficients of the medium at the fluorescence emission wavelength. After each successful fluorescence absorption event, the simulation added a sampled decay time, t_d, to the photon's total time of flight to include the effect of a finite fluorophore lifetime (τ_0).

To simulate the experimental procedure of placing the fiber probe above the AC sample surface, the reflectance and fluorescence photons were collected within an annulus of inner radius = 0.15 cm and outer radius = 0.33 cm (relative to source fiber center). The

simulation required input values of μ_a and μ_s, which were obtained from IS experimental measurements while the anisotropy was kept at a literature value of g = 0.9 [86], as described in Section 6.1.6.2. In this study, separate codes were run for two fluorescence emission wavelengths (400 nm and 540 nm) to simulate experimental data. Wavelength dependence of fluorescence emission characteristics of the two fluorophores were introduced by using the spectrally weighted fluorescence emission *W(λ)* described in Section 6.1.3 in lieu of the quantum yield coefficients ${}^{i}\Phi_{QY}$. The tissue thickness z_1 was the same as those for the samples used in Section 6.1.4. Fluorophore lifetime for bound NADH was set to 1.5 ns [11, 36]. The input values for the fluorescence lifetime of collagen and the relative fluorophore absorption coefficients ${}^{i}\mu_{afx}$ (for collagen and NADH) were matched to simulate experimental measurements (described in Section 6.1.6.4).

Table 6.1. Scattering and absorption coefficients for AC tissue (g = 0.9)

Wavelength (nm)	μ_a (cm^{-1})	μ_s (cm^{-1})
400	0.50 ± 0.05	300 ± 75
420	0.56 ± 0.02	285 ± 57
460	0.45 ± 0.16	220 ± 61
480	0.47 ± 0.09	188 ± 48
500	0.44 ± 0.23	168 ± 46
520	0.65 ± 0.06	133 ± 67
540	0.46 ± 0.21	199 ± 32
560	0.49 ± 0.21	125 ± 27
600	0.50 ± 0.20	106 ± 20

6.1.6 Results and discussion

6.1.6.1 Fluorescence excitation-emission matrix (EEM)

Figure 6.5a shows EEM data for AC tissue sample #12 (Table 6.2). The EEM fluorescence intensity pattern was consistent with endogenous tissue fluorescence from extracellular collagen and intracellular NADH [5, 8-10, 25, 54, 55]. Figure 6.5b shows this EEM data around excitation wavelength 355 nm, which was the wavelength employed for excitation in RFLS studies. These EEM tissue data were consistent with measurements on pure collagen and NADH at 355 nm excitation (Figure 6.2), further confirming the hypothesis that these two fluorophores represent the primary components of AC tissue autofluorescence in RFLS studies. Thus, the AC tissue model developed for computational simulations of these measurements was composed of these two endogenous tissue fluorophores.

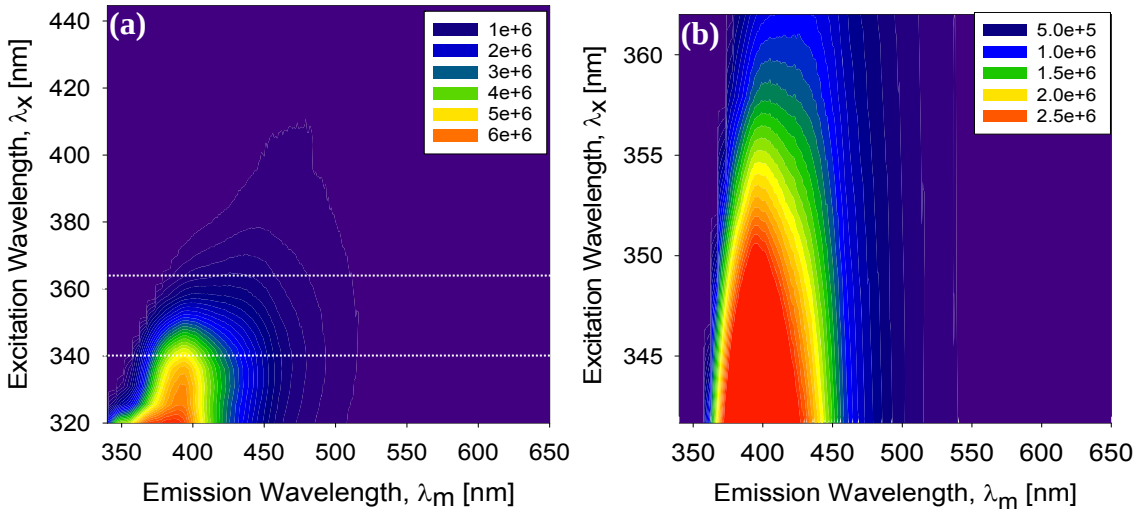

Figure 6.5 (a) Measured EEM of articular cartilage (AC) tissue showing fluorescence emission primarily associated with extracellular collagen and intracellular NADH [56]. (b) Same EEM expanded to highlight the area between white dotted lines in (a) [56]. RFLS excitation occurred at 355 nm. The EEM data was measured on the Fluorolog-3 spectrofluorometer.

6.1.6.2 Porcine AC tissue optical coefficients

AC Tissue optical absorption (μ_a) and scattering (μ_s) coefficients at nine wavelengths were calculated from IS measurements by employing the IAD software and an anisotropy value of $g = 0.9$ [86] (Table 6.1). For each coefficient, the table lists the mean ± standard deviation over data obtained on two AC tissue samples. The μ_s values decreased with increasing wavelength indicating lower wavelengths were scattered more by the tissue. There was no such specific trend for μ_a values. MC simulations were run using the two sets of μ_a and μ_s that were calculated using data from both tissue samples.

6.1.6.3 Reflectance spectroscopy: experimental measurements and computational modeling

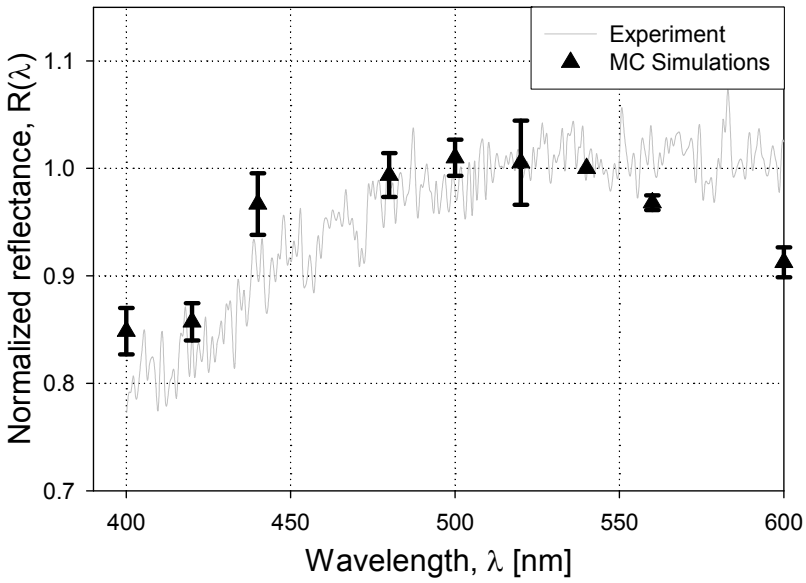

Figure 6.6 Average, measured (gray, solid line) and simulated (black, triangles) normalized reflectance spectra from porcine AC [56]. The normalization was done by setting reflectance at 540 nm to unity. The model inputs at each indicated wavelength were obtained from integrating sphere measurements. The error bars represent the results of the variations in the optical properties (see Table 6.1) input to produce the simulations.

Reflectance from 11 AC tissue samples (samples # 1-11, Table 6.2) varied over the wavelength spectrum and increased between 400 nm and 540 nm. The gray line in Figure 6.6 shows the measured average normalized reflectance as a function of wavelength between 400 and 600 nm. The normalization procedure set the reflectance at 540 nm to unity. Table 6.2 lists details of sample preparation for all samples, as well as the percentage increase (ΔR), in reflectance at 540 nm (R_{540}) vs. reflectance at 400 nm (R_{400}). Thus, $\Delta R = [R_{540} - R_{400}]*100/ (R_{540})$. The average measured ΔR value was found to be 23 (±7) %.

Table 6.2. Porcine articular cartilage (AC) sample preparation, experimental and, computational results [56].

AC Tissue Sample #	Sample Preparation	Measured ΔR[$]	Measured average fluorescence decay time (ns)		Simulated fluorescence decay time (ns) at BP 540 nm	Extracted η[%]
			BP[!] 400 nm	BP 540 nm		
1	Freshly harvested	25 %	4.3	4.0	4.04	25.00
2	Freshly harvested	17 %	5.4	5.3	5.25	60.00
3	Freshly harvested	29 %	4.8	4.1	4.13	12.00
4	Freshly harvested	22 %	4.9	4.1	4.13	10.54
5	Freshly harvested	11 %	5.1	4.5	4.49	15.00
6	Cultured*	28 %	5.4	4.0	3.98	5.45
7	Cultured*	28 %	5.3	4.8	4.81	20.33
8	Cultured	22 %	5.2	4.6	4.60	16.00
9	Cultured	13 %	5.1	4.0	4.00	7.00
10	Cultured	29 %	5.1	4.6	4.59	18.53
11	Cultured	27 %	5.2	4.4	4.42	11.50
12	Freshly harvested	-	5.2	4.2	4.21	8.52
13	Freshly harvested	-	5.3	4.2	4.21	7.59
14	Cultured	-	6.4	3.0	3.00	1.38
15	Freshly harvested	-	5.1	4.5	4.49	15.00
	Average value	*23± 7 %*	*5.2 ±0.4*	*4.3±0.5*		

* Measurements taken on different sites of an elongated tissue sample.

$ ΔR = percentage increase in reflectance at 540 nm (R_{540}) vs. reflectance at 400 nm (R_{400})

! BP = band-pass filter

% η = ratio of the fluorescence absorption coefficients of collagen to NADH

A set of nine simulations were run to study the radially resolved reflectance at nine excitation wavelengths between 400-600 nm (listed in Table 6.1). At each wavelength, two simulations were run using two sets of μ_a and μ_s values, obtained as described in Section 6.1.6.2. Figure 6.6 shows mean normalized reflectance (black triangles) calculated by the MC simulations. The error bars represent the standard deviation between outcomes at each wavelength. The MC simulation predictions matched well with the average experimental data over the entire spectral range with a maximum residual error of 11% and predicted a ΔR of 15 (±2) %. This corroboration between experiment and simulation for reflectance gave us confidence in our estimation of the wavelength dependence of the tissue optical properties of porcine AC. A similar study has been done to assess bovine cartilage thickness using MC simulations [87]. This study did not consider any wavelength dependence of the absorption and scattering coefficients.

6.1.6.4 Fluorescence and fluorescence lifetime spectroscopy: experimental measurements and computational modeling

Figure 6.7a shows a representative normalized intrinsic fluorescence spectrum from (sample # 15, Table 6.2) porcine knee AC tissue measured using the RFLS (black line). The fluorescence emission peaked near 400 nm, and was attributed to collagen dominated emission. The measured average decay time for the entire spectrum (i.e. with no BP filter employed) was observed to be 5.4 ± 0.5 ns, which was consistent with collagen dominated emission [88]. Figure 6.7a also shows the band-pass filters centered at 400 nm (dashed blue box) and at 540 nm (dashed red box), employed to take time-resolved measurements as described in Section 6.1.3. These representative, normalized time-

resolved data obtained from the same AC tissue (sample # 15, Table 6.2) are shown in Figure 6.7b for the BP at 400 nm (solid blue line) and for BP at 540 nm (dashed red line).

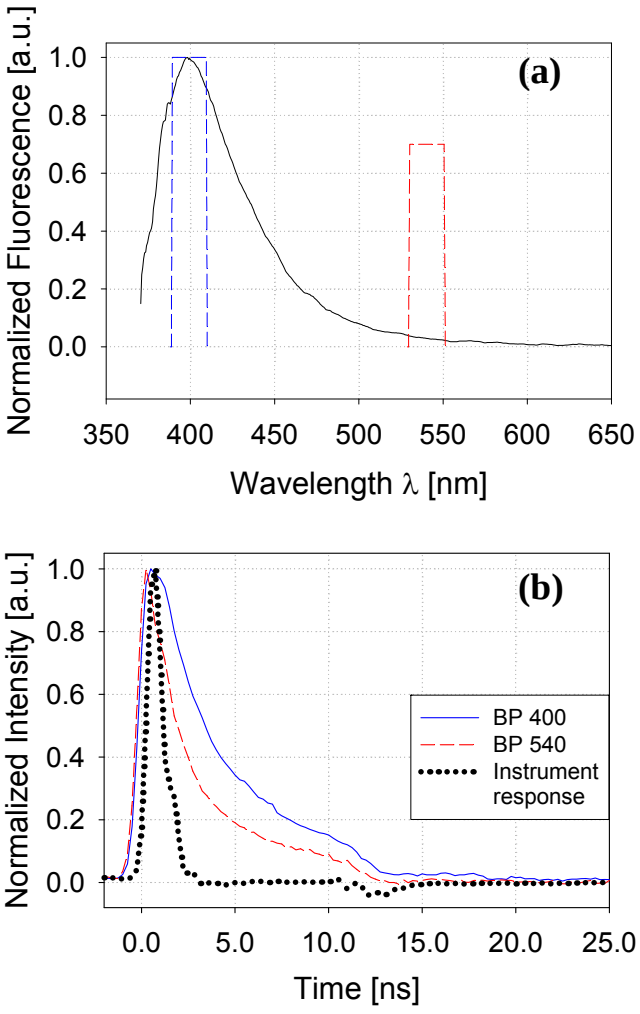

Figure 6.7 (a) Autofluorescence spectrum of AC tissue (black line) acquired on the RFLS. Blue and red boxes indicate band-pass (BP) filters placed at 400 and 540 nm to measure fluorescence decay times for photons from those parts of the spectrum [56]. (b) Time-resolved fluorescence of the tissue with a BP filter of 400 nm (solid blue line) and a BP filter of 540 nm (dashed red line). The black dotted line shows the excitation pulse temporal profile (instrument response) [56].

The dotted black line in Figure 6.7b shows the temporal profile of the excitation laser pulse. As can be seen in Figure 6.7b, the blue curve (BP 400) decayed slower than the red curve (BP 540). This trend was seen consistently amongst all the 15 measured samples

(Table 6.2). A one sided, unequal variances, Student t-test for the mean values of decay time at 400 nm and 540 nm wavelengths, yielded a P-value of 1.21×10^{-5}, indicating that the mean decay times were different from each other at the two band-pass filter locations.

As mentioned earlier, collagen type II and NADH were considered to be the two major fluorophores in the porcine AC tissue sample. The time-resolved fluorescence decays from each AC tissue sample at the two emission wavelengths (with BP filters centered at 400 nm and 540 nm) were simulated via two different tissue models to account for the differences in the optical transport coefficients at these two wavelengths. These simulated decays were analyzed by a bi-exponential model and an average decay time parameter was determined [36].

For each tissue model the tissue optical transport coefficients required at the central wavelength of each BP were obtained from the IS measurements as discussed in Section 6.1.6.2 (Table 6.1). The spectrally weighted fluorescence emission $W(\lambda)$ (Figure 6.2) at the corresponding central wavelength of the BP filter were used in lieu of the fluorophore quantum yields. These spectrally weighted fluorescence emission coefficients were 1.35×10^{-3} and 1.35×10^{-5}, for collagen and NADH, respectively, for the 400 nm BP tissue model while at 540 nm they were 8.64×10^{-5} and 2.80×10^{-4} for collagen and NADH, respectively.

Given these inputs for the fluorophore quantum yield coefficients, the simulations predicted that average decay time for the fluorescence signal at 400 nm using the bi-exponential model collapsed to the original input lifetime of collagen in the tissue model (irrespective of the exact values of the lifetimes of either fluorophore), if (η) the ratio of the fluorophore absorption coefficient of collagen to that of NADH was greater than 0.1,

which included the most physically plausible values for these fluorophores [36]. This behavior was anticipated in these simulations, since the weight of remitted fluorescence photons from collagen was on average 100 (approximately the ratio of the *W(λ)* inputs of collagen to NADH at 400 nm) times larger than weight of remitted fluorescence photons from NADH. This result, however, meant, that each measured average decay time with the 400 nm BP filter would have to be interpreted as the lifetime of collagen for each particular sample. The variability seen amongst samples could be attributed to changes in the environment of the fluorophore.

Hence, in the 540 BP tissue model, for each sample, the input lifetime of collagen was set to the average decay time measured (for the same sample) via the 400 nm BP while holding the lifetime of NADH at 1.5 ns. The model was then used to extract the fluorescence absorption coefficients (μ_{afx}) of both fluorophores by matching (to within 1%) the simulated average decay time at 540 nm to the experimentally measured fluorescence decay time measured via the 540 nm BP. Table 6.2 shows the values for η, the ratio of the fluorescence absorption coefficient of collagen to that of NADH for each measured AC tissue sample. Also shown are the predicted values of the simulated decay times using the η values specified. The extracted η values were found to vary by a large amount. One source of this variation could be the high variability in biological samples which can not be accounted for by simulations. It is thought that by repeating this study for a large number of samples the expected range of η values for naturally occurring AC tissues could be extracted. Then comparison of η values for artificially constructed AC tissue with this range could serve as a check of the viability of the

construct. In addition, this method of extracting η values could be used to monitor the development of an AC tissue construct over time, in a non-invasive manner.

Previous fluorescence lifetime imaging studies of what appear to be fixed and sectioned slices of porcine AC did not explain the biological origins of the detected fluorescence nor the statistical significance of the obtained data [89].

6.1.7 Summary and conclusions

In conclusion, a method for noninvasive, quantitative characterization of fresh tissues using reflectance and fluorescence measurements was applied to porcine knee AC. To the best of our knowledge, the work described in this report is the first study of endogenous fluorescence from unfixed and untreated porcine knee AC, where the biological origins of the measured fluorescence and reflectance are explained in the context of a quantitative model for photon transport in AC tissue.

MC simulations of photon propagation in a single layer, two – fluorophore (extracellular collagen type II and cellular NADH) tissue model were used to quantitatively explain experimentally measured fluorescence and reflectance signals from AC tissue. The concept of a spectrally weighted fluorescence emission $W(\lambda)$ was introduced to account for the wavelength dependence of fluorescence emission characteristics of the two fluorophores. The experimental and computational results agreed to within 11% of the mean reflectance spectra (from 11 samples), which provided the wavelength dependent tissue optical properties (μ_a and μ_s) for porcine AC tissue models. For fluorescence measurements, a combination of experimental measurements and computational simulation was used to extract a quantitative description of the samples. For each AC tissue sample, the MC simulations for fluorescence used the measured decay time at BP

400 nm as an input to extract the ratio of fluorescence absorption coefficients (η) of the constituent fluorophores such that simulated average decay time at 540 nm were made to match to within 1%, the experimentally measured fluorescence decay time.

Although the AC tissue models used the optical transport coefficients determined via the IS-estimated average, it is to be noted that the reflectance spectrum from each sample could be inverted via MC simulations (guided by the IS values) to obtain the sample's transport coefficients. Estimation of μ_a and μ_s using MC simulations vs. IS, for tissue models that had identical η values but modeled extreme variations of the transport coefficients, yielded average decay times (at 540 nm) that were within 1% of the decay time determined via using the IS estimates.

The approach presented here attributes a single fluorescence decay time to each constituent fluorophore in a tissue. A further refinement to this approach could include changes in fluorophore lifetime with emission wavelength. Although future systematic studies on pure substances should resolve conflicting reports existing in the literature regarding lifetime variations with wavelength (for example, for collagen [88]), it remains problematic to use data acquired on pure substances to describe those molecules in complex environments, such as biological tissues. An alternate and more biologically relevant approach would be to employ optical molecular imaging (via, e.g., fluorescence lifetime imaging microscopy) to characterize spatially-resolved endogenous fluorophores in their tissue environment. These studies are ongoing and should prove useful to enhance the ability to quantitatively interpret experimental measurements on tissues.

Hyaline AC is found in the synovial joints and is an important contributor to the functional capacities of these joints. If a chondral defect or lesion occurs, it does not heal

on its own. Thus methods are being developed to make tissue constructs that would mimic true AC. Pre- and post implantation testing of the viability of these constructs can potentially be done by analyzing the optical signal from them. Towards this goal, a first step has been taken to optically characterize porcine knee AC. This work and the methods developed here should aid in the future study of AC tissue constructs. For example, monitoring the change in η value for a sample over time would help detect changes in the sample's biological make-up by giving a measure of changes in relative concentrations of the constituent fluorophores. Furthermore, since the method would be non-destructive, it would allow repeated assessment of a given sample over time to follow intervention, thereby significantly speeding up lengthy and expensive protocols requiring multiple samples.

6.2 Oral mucosa constructs

6.2.1 Engineering oral mucosa constructs

Ex vivo produced oral mucosa equivalent (EVPOME) constructs are manufactured by seeding human oral keratinocytes onto an acellular dermal matrix namely, AlloDerm® (LifeCell, Branchburg, NJ, USA). AlloDerm is non-immunogenic human cadaver skin from which the cellular component has been removed to leave a matrix composed mainly of collagen. Details of the EVPOME manufacturing process can be found in [43, 46, 90]. Briefly, the dry AlloDerm® is first cut into a 1 cm diameter circle and immersed thrice in phosphate buffer saline (PBS) solution for 30 minutes to re-hydrate the dermal matrix and to remove any antibiotics injected to preserve the matrix. The re-hydrated AlloDerm® is then immersed overnight in a solution of PBS and collagen-IV to enhance

the attachment of keratinocytes. The harvested keratinocytes are then seeded on to the AlloDerm® on what is referred to as day 0 of the manufacturing process. The keratinocytes and AlloDerm® composite is then cultured submerged in cell culture media for four days. On day 4, the composite is raised to the air-liquid interface with an increase in calcium concentration to encourage stratification and is cultured in this manner until day 11. By this stage, the cell-matrix composite has undergone keratinocyte differentiation and stratification with formation of a keratinized layer, and the EVPOME construct is ready for implantation. Figure 6.8 shows the histology of a typical day 11 EVPOME construct consisting of keratin (layer 1), keratinocytes (layer 2), and AlloDerm® scaffold (layer 3).

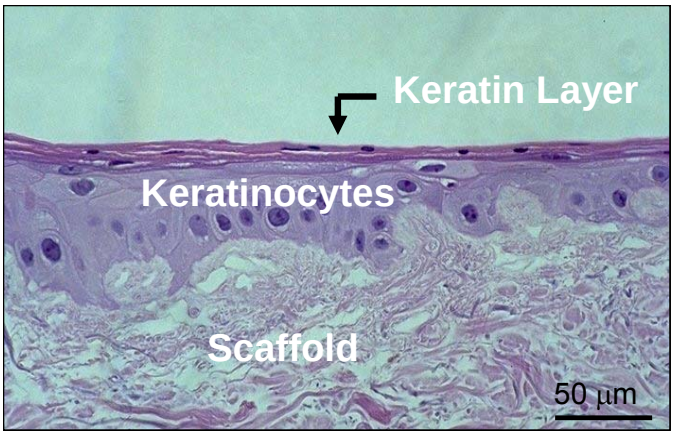

Figure 6.8 Cross-sectional histology of a day 11 EVPOME construct showing the three layers of the construct – keratinized layer, keratinocytes and AlloDerm® scaffold.

6.2.2 Optical signatures in EVPOME constructs

In order to investigate the sources of fluorescence in the cellular layer of EVPOME constructs, fluorescence spectroscopy measurements were made on oral keratinocytes by

employing the spectrofluorometer Fluorolog-3 (described in Section 4.1.3) at 355 nm excitation which is the excitation wavelength of the RFLS.

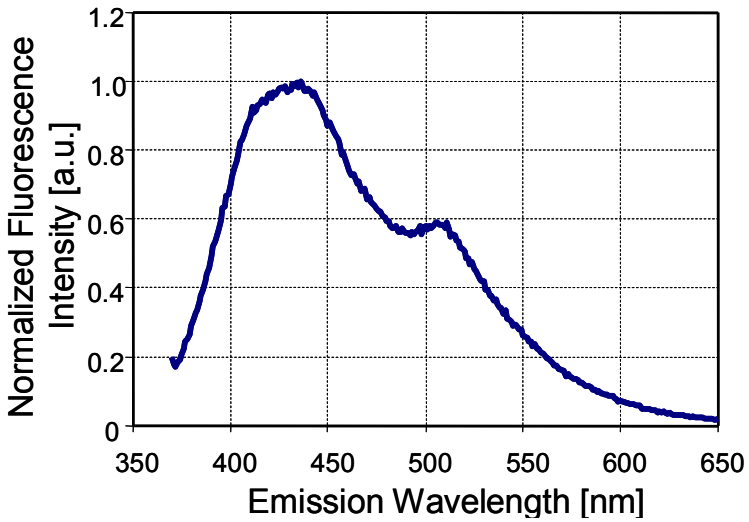

Figure 6.9. Plot of normalized fluorescence intensity measured from oral keratinocytes at 355 nm excitation. The data was measured on the Fluorolog-3 spectrofluorometer**.**

Figure 6.9 plots the normalized fluorescence intensity measured from oral keratinocytes. The observed fluorescence peaks were associated with NAD(P)H and FAD fluorescence [9]. As stated in Section 6.2.1, AlloDerm® is composed mainly of collagen. The constituent fluorophores in a day 11 EVPOME could thus be assumed to be the acellular keratin in the first layer, NAD(P)H and FAD in the second layer where the oral keratinocyte cells reside, and collagen in the third layer. Hence, it could be conjectured that assessment of the biological viability of the EVPOME constructs should be achievable by using fluorescence spectroscopy to target the fluorophores in the cellular component of the EVPOME namely, NAD(P)H and FAD. Previous studies done by us on the autofluorescence of oral keratinocytes of increasing size suspended in saline solution

indicated that cell size correlates positively with flavoprotein autofluorescence intensity [91]. The stem cell population has been found to reside in the small cell population while more mature differentiated cells are larger in size [92]. Thus, we expect the fluorescence intensity owing to FAD to increase as the cells mature and become larger in size i.e. as the EVPOME graft goes through its manufacturing process, with an increase in cell stratification. This provides a possible tool for sensing changes (hence viability), non-invasively, in the cellular component of EVPOME from day 0 to day 11 of the manufacturing process.

The cells in an EVPOME construct are present in a relatively thin layer buried between highly scattering and fluorescent keratin and collagen layers (Figure 6.8). This poses a significant challenge to the measurement of cellular autofluorescence. In the remaining text, we describe the Monte Carlo (MC) simulations and experiments executed to optimize detection of cellular autofluorescence in EVPOME constructs. Fluorescence simulations and measurements were executed for a 355 nm excitation wavelength (preferential excitation of NAD(P)H) and simulations were also implemented at 450 nm excitation wavelength (preferential excitation of FAD) for different optical probe designs to arrive at an optimum experimental set up for cellular autofluorescence detection.

6.2.3 Monte Carlo simulation of photon transport in EVPOME constructs at 355 nm and 450 nm excitation

A previously validated multi-fluorophore, multi-layer MC code of light propagation in tissue [15, 56, 61] was employed to simulate fluorescence in a day 11 EVPOME construct model. The EVPOME construct model was considered to be a three layer model with the fluorophore keratin in acellular layer 1, cells with NAD(P)H and FAD in

layer 2, and collagen in layer 3 (Figure 6.10). Simulations were executed at 355 nm and 450 nm excitation to predict (as a function of source detector fiber separation) the contributions to the detected fluorescence, from the fluorophores in different layers of the EVPOME. The simulations at 355 nm excitation were executed with optical fiber diameters of 100 μm. Simulations at 450 nm were executed for two optical fiber diameters, 50 μm and 100 μm. The tissue optical properties and fluorophore optical properties required as inputs to the MC codes are described in Section 6.2.4.

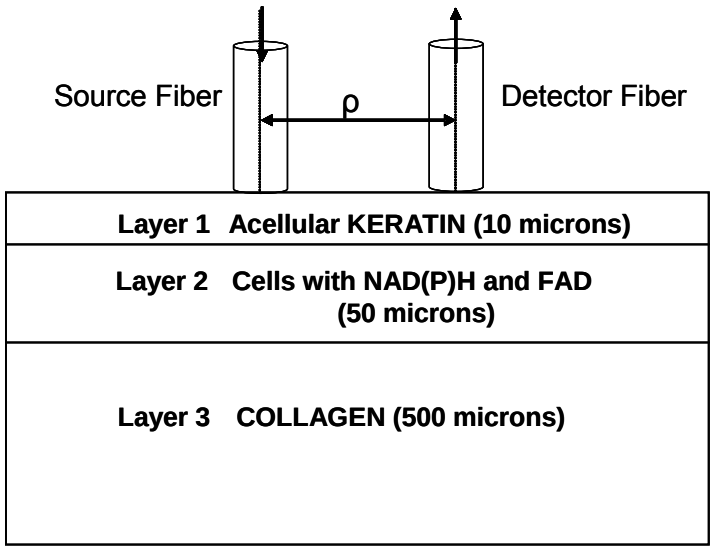

Figure 6.10 Schematic of the layers in an EVPOME construct on day 11 of the manufacturing process. Modeling was done for excitation wavelengths 355 nm and 450 nm assuming keratin (acellular), NAD(P)H and FAD in cells, and collagen to be the fluorophores localized in the layers as shown in the figure.

For each simulation, excitation photons were launched from a source fiber normal to the tissue surface. The photons per unit time exiting the tissue surface were collected by annuli of detectors placed around the source fiber at radii increasing in steps equal to the source fiber diameter. Photons entered the tissue with a weight of unity which was attenuated as governed by the absorption coefficient (μ_a) of the medium. The trajectory

of the photon in the medium was based on the scattering coefficient (μ_s) and anisotropy coefficient (g) of the medium. The different layers of the tissue were represented by a change in tissue optical properties (μ_a, μ_s, and g) and the path of the photons as they traversed between layers was governed by the Snell's laws and any refractive index (n) mismatch. The flight of the photon ended when it left the tissue (by crossing the tissue-air interface) or when its weight fell below a threshold minimum value (set to 1x10-5), as determined by a Russian roulette routine [62].

In any layer, the absorption of the excitation photon by a fluorophore was governed by the sum of the fluorophore absorption coefficients (μ_{afx}) of all fluorophores (N_f in number; = 1, 2, and 1 for layers 1, 2, and 3 respectively) in that layer. Where, each fluorophore was assumed to emit at a distinct emission wavelength (λ_m). The probability that the i^{th} fluorophore ($1 \leq i \leq N_f$) in a layer absorbed the excitation photon was equal to the ratio ${}^{i}\mu_{afx} / \Sigma^{i}\mu_{afx}$ ($1 \leq i \leq Nf$). Once absorbed by the i^{th} fluorophore in a layer, the excitation photon was marked as a fluorescence photon having wavelength ${}^{i}\lambda_m$ and was scattered isotropically. The weight of the photon was scaled by the quantum yield (${}^{i}\phi$) of that fluorophore and the trajectory was now governed by the scattering, absorption, and anisotropy coefficients of the medium at the fluorescence emission wavelength. The code kept an account of fluorescence weight per unit time of photons exiting the tissue surface at all emission wavelengths. These weights were integrated over time to give the steady state fluorescence detected at each detector due to each fluorophore.

6.2.4 Inputs to the Monte Carlo codes

In order to implement the MC simulations, it was necessary to specify the thickness and refractive index of each layer, tissue optical properties ($\mu_a(\lambda)$, $\mu_s(\lambda)$, and g) of each of the excitation (λ_x) and emission wavelengths (λ_m) in each layer, and the fluorophore optical properties (μ_{afx} , ϕ, and τ) for all the fluorophores.

Tissue optical properties of EVPOME

The thickness of the layers were set to be 10 μm, 50 μm, and 500 μm, to model a typical day 11 EVPOME (shown in Figure 6.10). The refractive index was set to 1.4 for all layers and the anisotropy (g) was set to 0.9, 0.85, 0.7 for layers, 1, 2, and 3, respectively [81]. Table 6.3 and Table 6.4 list the absorption (μ_a) and scattering coefficients (μ_s) used for simulations at 355 nm and 450 nm excitation, respectively. These were obtained from an algorithm [93] for extracting $\mu_a(\lambda)$ and $\mu_s(\lambda)$ for layers in skin, but with blood content set to zero.

Table 6.3. Tissue absorption(μ_a) & scattering coefficients(μ_s) used for MC simulations at an excitation wavelength of 355 nm [80].

λ (Fluorophore) (nm)	Layer 1		Layer 2		Layer 3	
	μ_a cm^{-1}	μ_s cm^{-1}	μ_a cm^{-1}	μ_s cm^{-1}	μ_a cm^{-1}	μ_s cm^{-1}
355 (Excitation)	6.95	729	3.88	486	3.88	486
420 (Keratin)	3.99	618	2.27	412	2.27	412
450 (NADH)	3.17	577	1.81	385	1.81	385
530 (FAD)	1.83	490	1.06	327	1.06	327
430 (Collagen)	3.69	604	2.1	403	2.1	403

Table 6.4. Tissue absorption(μ_a) & scattering coefficients(μ_s) used for MC simulations at an excitation wavelength of 450 nm

λ (Fluorophore) (nm)	Layer 1		Layer 2		Layer 3	
	μ_a cm^{-1}	μ_s cm^{-1}	μ_a cm^{-1}	μ_s cm^{-1}	μ_a cm^{-1}	μ_s cm^{-1}
450 (Excitation)	3.17	577	1.81	385	1.81	385
520 (Keratin)	1.95	499	1.13	333	1.13	333
525 (NADH)	1.87	494	1.09	329	1.09	329
530 (FAD)	1.83	490	1.06	327	1.06	327
500 (Collagen)	2.22	519	1.28	346	1.28	346

Fluorophore optical properties of EVPOME

The fluorophore optical properties employed for the MC codes at 355 nm and 450 nm excitation are shown in Table 6.5. These values were chosen based on literature as well as experiments performed by us (described below).

Table 6.5. Fluorophore properties used for Monte Carlo simulations of light propagation in EVPOME constructs at 355(450) nm excitation.

	Keratin	NAD(P)H	FAD	Collagen
Emission (nm)	420 (520)	450 (525)	530 (530)	430 (500)
Decay Time (ns)	4.0 (4.0)	1.5 (1.5)	3.0 (3.0)	5.0 (5.0)
Quantum Yield	0.25 (0.01)	0.05 (0.005)	0.03 (0.03)	0.4 (0.04)
μ_{afx} (cm^{-1})	0.5 (0.5)	0.6 (0.01)	0.9 (1.6)	0.9 (0.9)

The decay times of the fluorophores were assumed independent of the emission and excitation wavelengths. The values for keratin and FAD were obtained from [94] while for NADH and collagen were obtained from [36].

Fluorophore absorption coefficients and emission wavelengths for keratin were obtained from literature [95, 96]. The peak emission wavelengths and intensities at an excitation of 355 nm and 450 nm for NADH, FAD and collagen were measured on a spectrofluorometer (SPEX® FL3-22 Fluorolog-3, Jobin-Yvon Horiba, Japan). Solutions of 0.005 mg/ml of NADH (N-8129, Sigma Aldrich, St. Louis, Missouri) in water, 0.06 mg/ml of FAD (F6625, Sigma Aldrich) in water, and 1mg/ml of collagen (C5483, Sigma Aldrich) in acetic acid were used for the measurements. The absorbance of the same NADH, FAD, and collagen solutions were measured at the two excitation wavelengths using a spectrophotometer (DU® 800, Beckman Coulter, Inc., Fullerton, CA). The fluorophore absorption coefficients were then derived from the measured absorbance using the Beer-Lambert Law.

The quantum yields (ϕ) at 355 nm and 450 nm excitation were obtained from literature for keratin and FAD [81, 95, 97]. The values at 355 nm excitation for NADH and collagen were also obtained from literature [36]. In order to obtain an estimate of any order of magnitude change in the quantum yield of collagen and NADH at 450 nm excitation we considered the equation for calculation of quantum yield of an unknown sample [11]

$$\phi(\lambda_x) = \phi_R \frac{I(\lambda_x)}{I_R(\lambda_x)} \frac{A_R(\lambda_x)}{A(\lambda_x)} \frac{n^2}{n_R^2} \qquad \textbf{- 6.1}$$

Where, I denotes the integrated intensity, n denotes the refractive index, and A denotes the absorbance of the fluorophore at λ_x excitation wavelength. The subscript R refers to reference fluorophore of known quantum yield and ϕ_R was considered independent of the

excitation wavelength. A 1 μM solution of Rhodamine 6G (83697, Sigma Aldrich) in ethanol was employed as the reference fluorophore [11].

Thus, the ratio of $\phi(\lambda_{450x})$ / $\phi(\lambda_{355x})$ for a fluorophore could be expressed as

$$\frac{\phi_{450x}}{\phi_{355x}} = \frac{I(\lambda_{450x})}{I(\lambda_{355x})}\frac{A(\lambda_{355x})}{A(\lambda_{450x})}\frac{I_R(\lambda_{355x})}{I_R(\lambda_{450x})}\frac{A_R(\lambda_{450x})}{A_R(\lambda_{355x})} \qquad \textbf{- 6.2}$$

Measurements on Rhodamine 6G indicated

$$\frac{I_R(\lambda_{355x})}{I_R(\lambda_{450x})}\frac{A_R(\lambda_{450x})}{A_R(\lambda_{355x})} \propto 1 \text{ (order of magnitude)} \qquad \textbf{- 6.3}$$

Thus, $\phi(\lambda_{450x})/\ \phi(\lambda_{355x})$ for a fluorophore could be approximated as

$$\frac{\phi_{450x}}{\phi_{355x}} \propto \frac{I(\lambda_{450x})}{I(\lambda_{355x})}\frac{A(\lambda_{355x})}{A(\lambda_{450x})} \qquad \textbf{- 6.4}$$

Measured integrated emission intensity and absorbance at the 355 nm and 450 nm excitation for both collagen and NADH indicated order of magnitude ratios of quantum yield equal to

$$\frac{\phi_{450x}^{collagen}}{\phi_{355x}^{collagen}} \propto 10^{-1} \quad \text{and} \quad \frac{\phi_{450x}^{NADH}}{\phi_{355x}^{NADHn}} \propto 10^{-1} \qquad \textbf{- 6.5}$$

Estimates for quantum yields of NADH and collagen at 450 nm excitation were thus obtained by scaling the quantum yield values at 355 nm excitation (Table 6.5) by a factor of 10.

6.2.5 Steady-state fluorescence measurements at 355 nm excitation

A portable, fiber-optic coupled Reflectance and Fluorescence Lifetime Spectrometer (RFLS) (described in Chapter 3) was employed for steady-state fluorescence spectra measurements from a day 11 EVPOME and from an acellular AlloDerm® kept under similar conditions, as a control. Prior to data acquisition, the EVPOME and Alloderm® were dipped in PBS to wash away any cell culture media. The excitation light was delivered to the sample via a source optical fiber of 100 μm diameter and the emitted fluorescence was collected via a separate 100μm diameter collection fiber placed adjacent to the source fiber at the distal end (same fiber probe configuration as in the MC simulations at 355 nm excitation). For each spectrum, a background spectrum was acquired with the source blocked and was subtracted from the detected sample spectrum. Background subtracted data were then corrected for the spectral instrument response of the RFLS. The calibrated spectra were then normalized by scaling the peak intensity to unity. Details of these calibration procedures are described in Chapter 3.

6.2.6 Results of the MC simulations and experiment

Figure 6.11 shows the simulated fractional contributions from layers 1, 2, and 3 (black squares, red circles, and blue triangles, respectively) of a day 11 EVPOME to the detected fluorescence signal at 355 nm excitation as a function of source-detector separations (ρ). The simulations indicated that detected signal would be dominated by fluorescence from layer 3 i.e. collagen, at all ρ, thus making it difficult to assess changes occurring in layer 2 where the cells reside. Thus, while 355 nm excitation would preferentially excite NAD(P)H in the cells, collagen would emit at a much higher

quantum yield. As a result, that fluorescence collected at the tissue surface would be dominated by collagen emission.

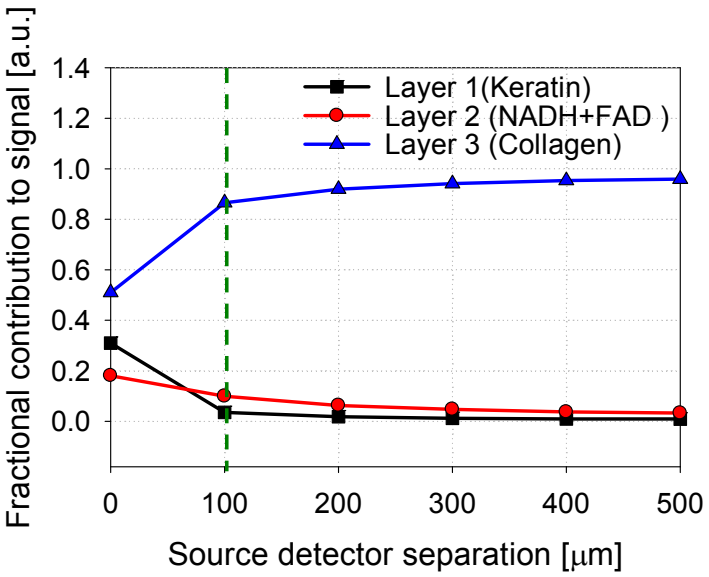

Figure 6.11. Results of MC simulations executed for day 11 EVPOME Model - Plot of simulated fractional contributions to the detected fluorescence signal from layer 1 (keratin : black squares), layer 2 (NADH+FAD : red circles), and layer 3 (Collagen : blue triangles) of a Day 11 EVPOME construct at 355 nm excitation for different source-detector separations. The green dashed line indicates the source-detector fiber separation during experiments [80].

Figure 6.12 shows the measured normalized fluorescence intensity (normalized by setting the peak intensity to unity) from AlloDerm® (blue dashed line) and EVPOME (red solid line) on day 11 at 355 nm excitation. The source detector separation was 100 microns (green dashed line in Figure 6.11). The measured signal from EVPOME could be associated predominantly with fluorescence from AlloDerm® alone (Layer 3). This confirmed the simulated results at 355 nm excitation. The variation in the measured spectra was within the variation seen among measured spectra from different batches of AlloDerm® tested.

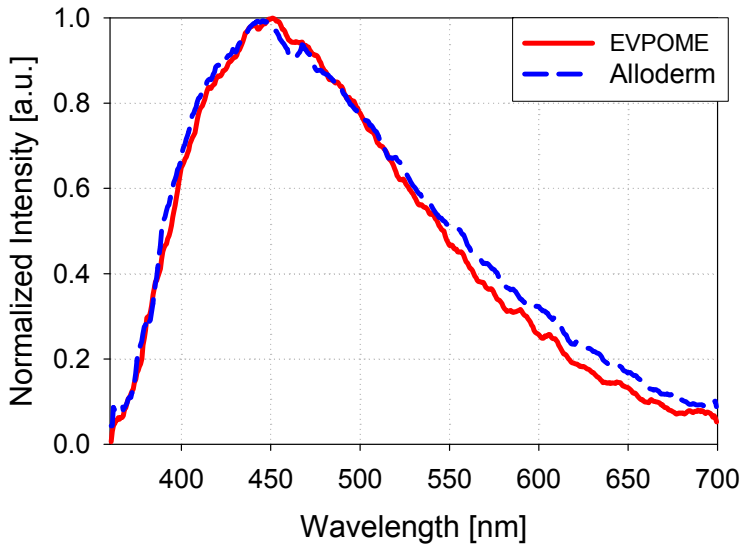

Figure 6.12. Plot of the measured normalized steady-state fluorescence from an EVPOME construct on Day 11 (red line), and from AlloDerm® kept under similar conditions (blue dashed line). Measurements were made at 355 nm excitation employing the Reflectance and Fluorescence Lifetime Spectrometer (RFLS); source and detector fiber diameters were 100 µm for simulations and experiment (dashed green line in Figure 6.11).

Figure 6.13 shows results of MC simulations at 450 nm excitation for two fiber diameters 100 µm (Figure 6.13a) and 50 µm (Figure 6.13b). The results indicated that employing 450 nm excitation and ρ = 0 would preferentially excite the FAD in the cells while decreasing the emission from collagen in layer 3. However, while the relative contribution form cellular autofluorescence would be increased, the emission from layer 3 would still be quite dominant.

Comparing different fiber sizes indicated better extraction of cellular signal for the smaller (50 µm) diameter fibers. However, as the fiber probe diameter is decreased, while the relative contribution of the cellular layer to the detected fluorescence could be increased, the over-all signal strength would decrease.

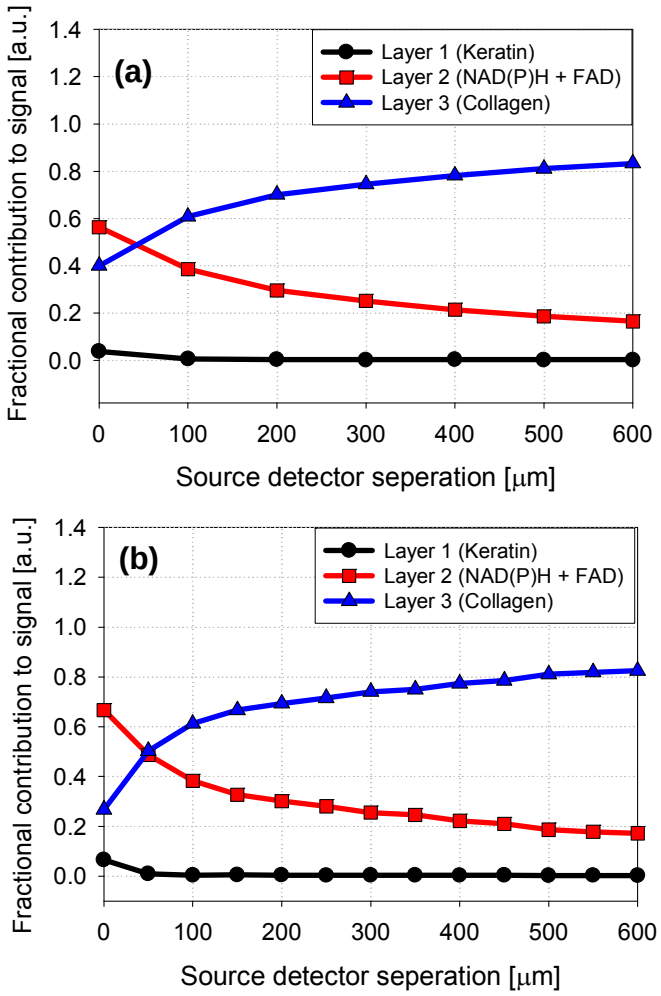

Figure 6.13. The simulated fractional contribution from Layer 1 (Keratin – black circles), Layer 2 (NAD(P)H + FAD – red squares), and Layer 3 (Collagen – blue triangles) to the detected fluorescence at 450 nm excitation for different source-detector separations. Simulations were run with fiber diameters set to 100 μm (a) and 50 μm (b).

6.2.7 Conclusion and discussion

In conclusion, Monte Carlo simulations and fluorescence experiments were employed to optimize non-invasive characterization of cell viability in tissue engineered oral mucosa constructs. Monte Carlo simulations were executed to simulate fluorescence of day 11 EVPOME constructs due to 355 nm and 450 nm excitations.

Fluorescence spectra measured at 355 nm excitation from day 11 AlloDerm® and EVPOME constructs validated the predictions of the simulations at 355 nm excitation. Both simulations and experiment indicated that the measured fluorescence signal from EVPOME constructs could be associated predominantly with fluorescence from AlloDerm® alone (layer 3) at 355 nm excitation.

The simulations at 450 nm indicated that the relative fluorescence contribution from the cellular component of the engineered construct could be increased by employing 450 nm excitation light and a single fiber geometry for light delivery and detection. However, while the relative contribution to the detected signal from cellular autofluorescence would be increased, the emission from collagen in layer 3 would still be quite dominant. Simulations implemented at different fiber diameters showed a further increase in relative contribution from cellular autofluorescence with decrease in fiber diameters. However, while employing a 450 nm excitation wavelength and decreasing the size of the fibers would amplify the relative contribution to detected fluorescence from the cellular layer, the reduction in over all signal intensity would be a limiting factor.

Thus, the results of this study indicate the need to investigate alternative solutions including different fiber probe geometries that might decrease collagen contribution while at the same time maximize fluorescence from the cellular layer in EVPOME. Angled fiber probes have been shown to be useful at selective excitation and collection of fluorescence from select areas of tissue samples [98]. Preliminary studies undertaken by us using MC codes at varying angles between source and detector fibers have shown promise at improving selective cellular fluorescence excitation and detection [99]. Another potential solution would be the use of fiber-optic coupled confocal microscopy

for selectively studying cellular autofluorescence. Chapter 7 shows preliminary measurements obtained from EVPOME constructs by employing confocal microscopy.

Chapter 7

Conclusions and Future Directions

7.1 Summary and conclusions

The primary goal of this dissertation was to develop and employ optical spectroscopic techniques for non-invasive sensing of (a) *human pancreatic tissues* to detect pancreatic adenocarcinoma and (b) *engineered tissue constructs* to assess the viability of the constructs during their manufacturing process.

Chapter 3 discussed the design of a clinically compatible reflectance and fluorescence lifetime spectrometer (RFLS) developed as a part of this dissertation work. The RFLS is a portable, fiber-optic coupled instrument capable of measuring reflectance and fluorescence spectra and time-resolved fluorescence decays. The instrument employs a pulsed 355 nm excitation laser for fluorescence excitation and a continuous wave lamp emitting between 360 to 2000 nm as the reflectance source. The detectors are optimized for optical detection in the 380 to 800 nm wavelength range.

In **Chapter 4**, we investigated whether optical spectroscopy could potentially aid in the detection of human pancreatic adenocarcinoma. Reflectance and fluorescence spectroscopies including time-resolved fluorescence decays were employed for the first time to probe freshly excised human pancreatic tissues and *in vivo* human pancreatic

cancer xenografts in mice. A total of 96 fluorescence and 96 reflectance spectra were considered from 50 tissue sites (including human pancreatic adenocarcinoma, chronic pancreatitis (inflammation), and normal tissues) on 9 patients. Measured optical spectra and fluorescence decays were correlated with tissue morphological and biochemical properties. Good correspondence was observed between spectra from human adenocarcinoma tissues and cancer xenografts grown in mice. In human pancreatic tissues, measurements were associated predominantly with endogenous fluorophores NAD(P)H and collagen, as well as tissue optical properties, with larger relative collagen content detected in adenocarcinoma and chronic pancreatitis than normal. Reflectance data indicated that adenocarcinoma had higher reflectance in the 430 to 500 nm range compared to normal and chronic pancreatitis tissues. The measured spectral features and decay times correlated well with expected pathological differences in normal, chronic pancreatitis and adenocarcinoma tissue states.

Thus, the ability of multi-modal optical spectroscopy to detect signals from pancreatic tissue was demonstrated by studying human pancreatic cancer xenografts in mice and freshly excised human pancreatic tumor tissue.

In **Chapter 5,** we presented the development of the first algorithms for pancreatic tissue classification using data from optical spectroscopy and assessed their diagnostic accuracy. The developed approach would be compatible with minimally-invasive diagnostic procedures for early cancer detection in the pancreas. Two classification algorithms using linear discriminant analysis were developed to distinguish among

tissues and leave-one-out cross validation was employed to assess the algorithms' performance.

The SpARC (Spectral Areas and Ratios Classifier) algorithm employed a combination of reflectance and fluorescence data and had sensitivity, specificity, negative predictive value, and positive predictive value for correctly identifying adenocarcinoma of 85%, 89%, 92%, and 80%, respectively. The performance of the SpARC algorithm for adenocarcinoma distinction from normal tissue and chronic pancreatitis was comparable to that of, and in some cases better than, the reported performance of EUS-FNA [30], the currently accepted diagnostic standard. In the setting of pancreatitis, i.e. when the patient has adenocarcinoma and chronic pancreatitis, the sensitivity of SpARC (85%) was well above that of EUS-FNA (54%) [31] for distinguishing adenocarcinoma from chronic pancreatitis, which is an unmet clinical need in pancreatic cancer detection. Although the SpARC algorithm is simple to implement, its performance may be limited because it utilizes information at select wavelengths only. Towards this end, a chemometric algorithm employing principal component analysis (PCA) and linear discriminant analysis of fluorescence and reflectance spectra was developed for pancreatic tissue classification.

The PCA algorithm that employed a combination of both reflectance and fluorescence classification variables performed the best and a maximum sensitivity, specificity, NPV, and PPV for correctly identifying pancreatic adenocarcinoma of 91%, 90%, 95%, and 83%, respectively, was achieved. The algorithm's performance was comparable and in some cases significantly better than that of EUS-FNA for pancreatic adenocarcinoma. Also, in the specimens where cancer was present along with chronic pancreatitis, the

sensitivity of the optical chemometric algorithm (82%) was well above that reported in other studies for EUS-FNA (54%) for distinguishing between adenocarcinoma and chronic pancreatitis [31], indicating a significantly decreased likelihood of obtaining false negative results. PCA and LDA of a limited data set of chronic pancreatitis and normal tissue measurements indicated that inclusion of time-resolved fluorescence data in the analysis could improve the classification performance of the developed tissue classification algorithms.

While the diagnostically relevant PCs cannot be linked to morphological or biochemical changes in tissue, PCA of the spectral data considers information at all wavelengths of the fluorescence and reflectance spectra. This is an improvement over the spectral areas and ratios classifier (SpARC) algorithm, which employed information only at select spectral wavelengths for tissue classification. The sensitivity for correctly identifying adenocarcinoma using the SpARC algorithm was 85% and is less than that of the optical chemometric algorithm developed in this study (91%). We are also developing a tissue classification algorithm that employs biophysical tissue parameters extracted from optical data using a photon-tissue interaction model we reported recently [72]. Future work will also involve data acquisition *in vivo*, with the aim of deploying the fiber-optic probe through a needle for optically-guided EUS-FNA.

Thus, the developed tissue classification algorithms show promise for pancreatic tissue classification using multi-modal optical spectroscopy. In a clinical setting, such a classification procedure could be undertaken for rapid, automated tissue classification either to guide EUS-FNA procedures or to improve tumor margin detection during pancreatic surgery.

In **Chapter 6,** the prospect of employing developed optical spectroscopy instrumentation and previously developed Monet Carlo (MC) simulations to non-invasively and quantitatively investigate endogenous optical signals from tissue engineered devices was assessed. The methods developed have the significant advantage of being safe for clinical human use as they employed endogenous contrast.

Porcine articular cartilage

A method to non-invasively and quantitatively characterize thick biological tissues by combining both experimental and computational approaches in tissue optical spectroscopy was developed and validated on fifteen porcine articular cartilage (AC) tissue samples. To the best of our knowledge, this study is the first to couple non-invasive reflectance and fluorescence spectroscopic measurements on freshly harvested tissues with Monte Carlo computational modeling of time-resolved propagation of both excitation light and multi-fluorophore emission. The experimental and computational results agreed to within 11% of the mean reflectance spectra. Fluorescence data and simulations were used to extract the ratio of the absorption coefficients of constituent fluorophores for each measured AC tissue sample. This ratio could be used to monitor relative changes in concentration of the constituent fluorophores over time. The samples studied possessed the complexity and variability not found in artificial tissue-simulating phantoms and served as a model for future optical molecular sensing studies on tissue engineered AC constructs intended for use in human therapeutics. An optical technique that could non-invasively and quantitatively assess soft tissue composition or physiologic status would represent a significant advance in tissue engineering. Moreover, the general approach described here for optical characterization should be broadly applicable to

quantitative, non-invasive molecular sensing applications in complex, three-dimensional biological tissues.

Oral mucosa constructs

Monte Carlo simulations and fluorescence experiments were employed to optimize non-invasive characterization of cell viability in tissue engineered oral mucosa constructs. Monte Carlo simulations were executed to simulate fluorescence of EVPOME constructs due to 355 nm and 450 nm excitation. Fluorescence spectra measured at 355 nm excitation from AlloDerm® and EVPOME constructs validated the predictions of the simulations at 355 nm excitation. Both simulations and experiment indicated that the measured signal from EVPOME could be associated predominantly with fluorescence from AlloDerm® alone (Layer 3) at 355 nm excitation. The simulations at 450 nm indicated that the relative fluorescence contribution from the cellular component of the engineered construct could be increased by employing 450 nm excitation light and a single fiber geometry for light delivery and detection. However, while the relative contribution to the detected signal from cellular autofluorescence would be increased, the emission from collagen in layer 3 would still be quite dominant. Simulations implemented at different fiber diameters showed a further increase in relative contribution from cellular autofluorescence with decrease in fiber diameters. However, while employing a 450 nm excitation wavelength and decreasing the size of the fibers would amplify the relative contribution to detected fluorescence from the cellular layer, the reduction in over all signal intensity would be a limiting factor. Thus, the results of this study indicated the need to investigate alternative solutions including different fiber probe geometries that might decrease extracellular contributions to the detected

fluorescence while at the same time maximize fluorescence detection from the cellular layer in EVPOME.

The major contributions of this dissertation can be summarized as follows:

- We designed and developed a clinically compatible, fiber optic coupled, reflectance and fluorescence lifetime spectrometer that could be employed for measuring reflectance and fluorescence spectra and time-resolved fluorescence decay curves from biological tissues.
- We developed a graphical-user-interface for remote and fully automated detection of optical spectra in a clinical setting employing the RFLS.
- We made the first *in vivo and ex vivo* measurements of reflectance and fluorescence spectra from human pancreatic xenografts in mice and correlated optical measurements with expected histopathology.
- We made the first *ex vivo* measurements of reflectance and fluorescence spectra and time-resolved fluorescence decays from human pancreatic tissues resected during pancreatic surgeries.
- We presented the first assessment of the diagnostic accuracy of algorithms developed for pancreatic tissue classification using data from optical spectroscopy by employing two tissue classification algorithms: the SpARC (Spectral Areas and Ratios Classifier) algorithm and the principal component analysis (PCA) algorithm.
- We presented a novel method coupling non-invasive reflectance and fluorescence spectroscopic measurements on freshly harvested tissues with Monte Carlo computational modeling of time-resolved propagation of both excitation light and

multi-fluorophore emission and applied the developed methods to assess untreated, unfixed porcine articular cartilage using endogenous contrast.

- We employed Monte Carlo simulations and fluorescence experiments for the first time to optimize the detection of cellular autofluorescence in *ex vivo* produced oral mucosa equivalent (EVPOME) constructs using endogenous contrast.

The work in this dissertation has been presented and documented as cited below:

Chapter 4

- M. Chandra, J. Scheiman, D. Heidt, D. Simeone, B. McKenna, and M.-A. Mycek, "Probing Pancreatic Disease using Tissue Optical Spectroscopy," *J. of Biomedical Optics*, 12 (6), 060501, 2007 (3 pages).
- M. Chandra, D. Heidt, D. Simeone, B. McKenna, J. Scheiman, and M.-A. Mycek, "Pancreatic Tissue Assessment using Fluorescence and Reflectance Spectroscopy," *Diagnostic Optical Spectroscopy in Biomedicine IV*, Dietrich Schweitzer, Maryann Fitzmaurice, Editors, Proc. SPIE Int. Soc. Opt. Eng. 6628, 66281R, 2007 (8 Pages).
- R. H. Wilson, M. Chandra, J. Scheiman, D. Heidt, D. Simeone, B. McKenna, and M.-A. Mycek, "Modeling Reflectance and Fluorescence Spectra of Human Pancreatic Tissues for Cancer Diagnostics," in *OSA Frontiers in Optics*, *Technical Digest (CD)*, 2008, Optical Society of America, FTuK5, 2008, (1 page).
- R. H. Wilson, M. Chandra, J. Scheiman, D. Simeone, B. McKenna, J. Purdy, and M.-A. Mycek, "Mathematical modeling of reflectance and intrinsic fluorescence for early cancer detection in human pancreatic tissue," Proc. SPIE 7187, 71870H, 2009 (9 pages).

- R. H. Wilson, M. Chandra, J. Scheiman, D. Simeone, B. McKenna, J. Purdy, and M.-A. Mycek, "Optical spectroscopy detects histological hallmarks of pancreatic cancer," *Optics Express* 17, 17502, 2009 (15 pages).

Chapter 5

- M. Chandra , R. H. Wilson, J. Scheiman, D. Simeone, B. McKenna, J. Purdy, and M.-A. Mycek, "Optical spectroscopy for clinical detection of pancreatic cancer", Proc. of SPIE, 7368, 73681G, 2009 (6 pages).
- M. Chandra, J. Scheiman, D. Simeone, B. McKenna, J. Purdy, and M.-A. Mycek, "Spectral Areas and Ratios Classifier (SpARC) algorithm for pancreatic tissue classification using optical spectroscopy," (submitted for journal publication).
- M. Chandra , William R. Lloyd, R. H. Wilson, J. Scheiman, D. Simeone, J. Purdy, B. McKenna, and M.-A. Mycek, "Principal component analysis of tissue optical response: a framework for automated clinical detection of pancreatic cancer," (submitted for journal publication).
- R. H. Wilson, M. Chandra, William R. Lloyd, J. Scheiman, D. Simeone, J. Purdy, B. McKenna, and M.-A. Mycek, "Photon-tissue interaction model for quantitative optical analysis of disease in the pancreas without histopathology," (journal manuscript in preparation).
- M. Chandra , R. H. Wilson, William R. Lloyd, J. Scheiman, D. Simeone, J. Purdy, B. McKenna, and M.-A. Mycek, "A hybrid approach to pancreatic tissue classification using multi-modal optical spectroscopy: an *ex vivo* study," (journal manuscript in preparation).

Chapter 6

- M. Chandra, K. Vishwanath, G. D. Fichter, E. Liao, S. J. Hollister, and M.-A. Mycek, "Quantitative molecular sensing in biological tissues: an approach to non-invasive optical characterization," *Optics Express* 14, 6157, 2006 (15 pages).
- M. Chandra, K. Vishwanath, G. D. Fichter, E. Liao, S. J. Hollister, and M.-A. Mycek, "Noninvasive, quantitative fluorescence sensing in 3D tissues: an approach to *in vivo* molecular characterization of engineered tissue constructs," in *Biomedical Optics 2006 Technical Digest*, ME59 (3pages).
- K. Vishwanath, K. Izumi, M. Chandra, Stephen E. Feinberg, and M.-A. Mycek, "Quantitative, Noninvasive Optical Sensing in Tissue Engineered Oral Mucosal Constructs," in *Biomedical Optics 2006 Technical Digest*, ME75 (3 pages).
- W.-L. Lo, K. Vishwanath, M. Chandra, Kenji Izumi, S. E. Feinberg, C.L. Marcelo, M.-A. Mycek, "Cell size correlates with flavoprotien endogenous fluorescence in cultured human oral keratinocytes," in The 9th International Conference on Optics Within Life Sciences, Taipei, Taiwan, 2006 (1 page).
- M. Chandra, R. H. Wilson, W.-L. Lo, K. Vishwanath, K. Izumi, S. E. Feinberg, and M.-A. Mycek, "Sensing Metabolic Activity in Tissue Engineered Constructs," *Diagnostic Optical Spectroscopy in Biomedicine IV*, Dietrich Schweitzer, Maryann Fitzmaurice, Editors, Proc. SPIE Int. Soc. Opt. Eng. 6628, 66280B, 2007 (7pages).
- R. H. Wilson, M. Chandra, W.-L. Lo, K. Vishwanath, K. Izumi, S. E. Feinberg, and M.-A. Mycek, "Simulated Fiber-Optic Interrogation of Autofluorescence from

Superficial Layer of Tissue-Engineered Construct," in *OSA Frontiers in Optics, Technical Digest (CD)*, Optical Society of America, FTuK6, 2008 (1page).

7.2 Future directions

7.2.1 Changes to the RFLS instrumentation

While certain changes to the spectrometer instrumentation including, laser excitation wavelength and fiber probe geometry, would depend on the biological system being studied, other changes can be made to improve the working of the RFLS. Some of these changes will be useful during data acquisition in an *in vivo* setting as they could result in lower data acquisition times.

As discussed in Section 3.2.2, a 30 μs ICCD gate width is required for fluorescence spectral acquisitions due to the temporal jitter in the emitted laser pulses. While this gate delay was not an issue in the present work, if data acquisition requires reduction of the gate width size due to fast changes in the background lights (say inside an endoscope during *in vivo* data acquisition) then this issue would need to be addressed. In principle, an optical trigger from the photodiode in Figure 3.2 could be used for the ICCD instead of the electrical trigger from the T/C board. However, the gate delay can be set to only 85 ns or higher employing the present Delay Generator, while the approximate time between the optical trigger and the time taken for the fluorescence to travel from the specimen via the optics and the fiber probe to the ICCD camera was found to be only ~ 20 ns. Thus, the fluorescence pulse will always be missed even when the gate delay is set to the minimum (as it would actually be 85 ns). A possible solution would be the use of longer fiber probes. This would artificially introduce a delay between the emitted laser pulse and

the time taken for the fluorescence to travel from the specimen via the optics and the fiber probe to the ICCD camera. For example, a 20 m long silica fiber would introduce an approximately 100 ns delay in light propagating through it thus, allowing the electronics to catch up.

Newer, more sensitive detectors including the WTM (wavelength – time matrix) technology from Fluorescence Innovations Inc. (Bozeman, Montana) can be incorporated into the RFLS for fluorescence detection. The WTM technology would enable the rapid acquisition of spectrally resolved time-resolved data, thus allowing a more thorough optical investigation of biological systems.

The ICCD camera is run in external trigger mode to synchronize the data acquisition with emitted laser pulses during fluorescence acquisitions (Section 3.2.2). For reflectance spectra acquisitions, this is not necessary and the ICCD can be run in an internal trigger mode. In the present ICCD camera, a switch between external and internal trigger modes has to be done manually. As a result, for reflectance measurements as well, the external trigger mode is being used in the interest of time and leads to the need for longer integration times. A quick switch to the internal trigger mode remotely using LabVIEW would lead to shorter integration times for reflectance data acquisition. Thus, an ICCD where one can change between external and internal trigger modes remotely could reduce reflectance acquisition times.

The Biomedical Engineering Unit affiliated with the Institutional Review Board at the University of Michigan has recommended the use of an enclosed cart with larger wheels (for ease during transport) for housing the RFLS in a clinical setting.

7.2.2 Detection of pancreatic adenocarcinoma

Further analysis of acquired optical spectroscopy data

This dissertation work employed linear discriminant analysis and principal component analysis for tissue classification algorithm development. Other chemometric approaches can also be investigated to see if further improved classification can be achieved. Some of these techniques include multiple linear regression analysis, neural network analysis, logistic discrimination, partial least squares, multivariate linear regression, and support vector machine [4, 7, 19-23].

We are presently working on the analysis of additional multi-modal optical spectroscopy data measured *ex vivo* from human pancreatic cancer tissues during the course of this dissertation work. This includes data measured from 66 sites on 10 additional patients. The developed tissue classification algorithms will be tested on the larger data set of optical spectroscopy data.

Another future work would be the classification of the optical data measured from sites that were excluded due to their histopathology in Section 4.2.1. These include serous cystadenomas, metastatic breast adenocarcinoma, intraductal papillary mucinous neoplasm, pancreatic intraepithelial neoplasia (a precursor to adenocarcinoma), scar or fat tissue, or a hybrid tissue site having two or more pathologies.

In vivo optical measurements from human pancreatic tissues

We are now poised for conducting i*n vivo* optical studies, pending IRB approval. The first *in vivo* experiments would be undertaken during pancreatic surgery by employing a sterilized fiber optic probe with the same dimensions and design as the probe used in the *ex vivo* studies. Apart from ensuring the manufacturing of a sterilizable fiber probe by a

vendor employing current good manufacturing practices defined by the Food and Drug Administration (FDA), the following two precautions *must* be taken to comply with the IRB requirements for this study: (i) a short-pass filter that cuts- off around 750-800 nm should be employed in front of the reflectance lamp source. This precaution is necessary to prevent any possible heating of the tissue due to light emitted in the NIR and IR region by the lamp. (ii) The laser and lamp lights should be blocked prior to data acquisition and should be opened only during acquisition of fluorescence and reflectance data from the tissues to minimize the amount of source light incident on the tissues.

The eventual aim of the pancreas project would be to employ fiber probes that can fit through the EUS needle to obtain multi-modal optical spectroscopy data *in vivo* during EUS-FNA studies. The EUS needle (Echo-Tip 19, G31520, Wilson Cook Medical, Winston-Salem, NC) is 19 gauge and has an inner diameter of ~680 μm (outer diameter of ~ 1.07 mm). The size of the fibers employed in the optical probe would have to be reduced to fit through the needle. Monte Carlo simulations could be undertaken to design the optimum fiber probe configuration which would provide the desired collection sensitivity and specificity to extract relevant structural and biochemical information from pancreatic tissues measurements during EUS-FNA procedures.

Measurements of mouse models for pancreatic cancer

Controlled experimentation and larger data sets can be achieved by studying animal models. In this dissertation work, human pancreatic xenografts were studied in mice with immunodeficiency. As a result, the mouse models did not mimic the increased fibrosis associated with adenocarcinoma in humans. Future studies could involve the measurement of mice models that more closely mimic progression of the disease in

humans, such as the models being developed in Prof. M. Pasca di Magliano's laboratory at the University of Michigan.

Tissue optical properties of pancreatic tissue

The tissue optical properties of pancreatic tissue are needed for MC simulations. An experiment could be designed for extracting these properties for adenocarcinoma, pancreatitis, and normal pancreatic tissues by employing Integrating Sphere measurements (as described in Section 6.1.4).

7.2.3 Assessment of articular cartilage constructs

In this study, a large variation was seen in the extracted η values (ratio of the absorption coefficients of constituent fluorophores) for different samples. By repeating the study for a larger number of samples, the expected range of η values for naturally occurring AC tissues could be extracted. Thus, future work could include undertaking the above study for a larger set of porcine AC tissue to extract η values in the same manner as in the preliminary study reported here.

The developed methods could then be applied to extract η values of tissue engineered AC constructs and a comparison could be made of η values for artificially constructed AC tissue with the range of η values for naturally occurring AC tissues. This could serve as a check of the viability of the construct. In addition, this method of extracting η values could be used to monitor the development of an AC tissue construct over time, in a non-invasive manner.

The approach presented here attributes a single fluorescence decay time to each constituent fluorophore in a tissue. A further refinement to this approach could include changes in fluorophore lifetime with emission wavelength. Although future systematic

studies on pure substances should resolve conflicting reports existing in the literature regarding lifetime variations with wavelength (e.g., for collagen [88]), it remains problematic to use data acquired on pure substances to describe those molecules in complex environments, such as biological tissues. An alternate and more biologically relevant approach would be to employ optical molecular imaging (via, e.g., fluorescence lifetime imaging microscopy [100]) to characterize spatially-resolved endogenous fluorophores in their tissue environment.

7.2.4 Assessment of cellular viability in EVPOME constructs

More detailed optical characterization of EVPOME

In this study, an initial attempt was made to obtain the tissue and fluorophore optical properties of EVPOME constructs. Alloderm® should be characterized further by measuring tissue optical properties using an integrating sphere as described in Section 6.1.4. In addition, the presence of other fluorophores like elastin in the matrix should also be considered.

Angled fiber optic probes for selectively exciting and detecting cellular fluorescence

A conclusion of the study on EVPOME constructs was the need for alternative solutions to decrease acellular contributions to detected fluorescence while maximizing fluorescence from the cellular layer in EVPOME. Preliminary studies undertaken by us using Monte Carlo codes at varying angles between source and detector fibers have shown promise at improving selective cellular fluorescence excitation and detection [99]. Future work could involve measurements of EVPOME constructs employing fiber optic probes designed with optimal angles between source and detector fibers as dictated by the

MC simulations. One potential problem with this approach could be the manufacturing of such probes. The preliminary angled fiber MC simulations have indicated the need for > 50^{o} angles between source and detector fibers which could be a design issue.

Confocal microscopy for selectively exciting and detecting cellular fluorescence

Another possible solution could be employing confocal microscopy for selectively measuring fluorescence from the cellular layer. We conducted preliminary experiments in which measurements from EVPOME constructs were made employing the Zeiss LSM510 Confocal fluorescence images were measured from a healthy Day 11 EVPOME construct at 364 nm and 458 nm excitation, to selectively detect NADH and FAD related fluorescence emission from these cells, respectively. Figure 7.1a and Figure 7.1b show the combined NADH and FAD emission from a non-stressed (NS) EVPOME construct, where Figure 7.1b is a zoomed in version. The haze in the images could be attributed to scattering of light from keratin and collagen layers. Thus, by employing confocal microscopy we could detect signals from the cellular layer in EVPOME.

Employing redox ratios for assessment of tissue viability

Metabolic activity in living cells and tissues has been assessed via optical measurements of the redox ratio of NADH and FAD, two cellular metabolic co-factors involved in the oxidative phosphorylation pathway in mitochondria. In their reduced and oxidized states, NADH and FAD are endogenous cellular fluorophores, respectively [101-117]. This method has been applied successfully to measure metabolic changes in mesenchymal stem cells placed in stem cell-supporting or osteogenic medium and found to report on stem-cell differentiation, cell density, and cell contact [108].

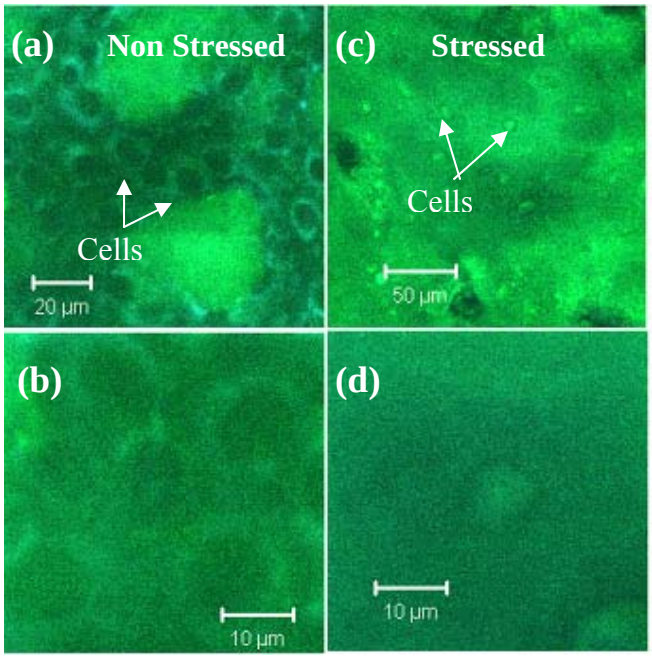

Figure 7.1. Confocal microscopy image of the combined NADH and FAD emission from keratinocytes in a healthy non-stressed (**a** – zoomed out, **b** – zoomed in) and stressed (**a** – zoomed out, **b** – zoomed in) day 11 EVPOME construct

A preliminary attempt was made to calculate redox ratios from the healthy (non-stressed) and "stressed" day 11 EVPOME constructs. The stressed constructs simulated non-viable EVPOME constructs and were stressed by increasing incubation temperature of the constructs from 37^0C to 43^0C with 5% CO_2, for 24 hours. Figure 7.1c and Figure 7.1d are confocal images from a stressed EVPOME sample. The cells were found to be smaller in the stressed case compared to the healthy case. Redox ratio defined as signal from FAD at 450 nm excitation divided by signal from NADH at 355 nm excitation was calculated from the cellular regions of the acquired images. The redox ratio was found to increase from the non – stressed (0.58 ± 0.06) to the stressed (0.99 ± 0.1) EVPOME constructs by

72 ± 29 %. Thus, redox ratio measurements could be a feasible tool to detect differences between healthy and non-viable EVPOME constructs.

7.3 Potential applications

The instrument developed in this dissertation work is a versatile research instrument that can be easily optimized for non-invasive optical assessment via reflectance and fluorescence spectroscopy of a variety of biological systems in a laboratory or clinical setting. Some of the aspects that can be changed include fiber probe design (size and source-detector fiber geometry), spectroscopy at select wavelengths by the application of long-pass, short-pass or band-pass filters, and use of different excitation wavelengths for fluorescence spectroscopy.

The algorithms developed in this dissertation work for pancreatic tissue classification could also be generally applied to classifying optical data obtained from other biological tissues, be it to differentiate healthy vs. stressed tissue engineered constructs or to differentiate between healthy and diseased biological tissues in animal models or humans.

The general approach developed in this thesis for optical characterization by combining experimental and computational approaches in tissue optical spectroscopy should be broadly applicable to quantitative, non-invasive molecular sensing applications in complex, three-dimensional biological tissues.

References

1. A. J. Welch, M. J. C. van Gemert, W. Star, and B. Wilson, "Definitions and overview of tissue optics," in *Optical thermal response of laser irradiated tissue*, A. J. Welch and M. J. C. van Gemert, eds. (Plenum Press, New York, 1995), pp. 15-46.

2. B. Wilson and S. Jacques, "Optical reflectance and transmittance of tissues: principles and applications," IEEE J Quantum Electron **26**, 2186-2199 (1990).

3. Z. Volynskaya, A. S. Haka, K. L. Bechtel, M. Fitzmaurice, R. Shenk, N. Wang, J. Nazemi, R. R. Dasari, and M. S. Feld, "Diagnosing breast cancer using diffuse reflectance spectroscopy and intrinsic fluorescence spectroscopy," J Biomed Opt **13**, 024012 (2008).

4. G. Salomon, T. Hess, A. Erbersdobler, C. Eichelberg, S. Greschner, A. N. Sobchuk, A. K. Korolik, N. A. Nemkovich, J. Schreiber, M. Herms, M. Graefen, and H. Huland, "The Feasibility of Prostate Cancer Detection by Triple Spectroscopy," Eur Urol **55**, 376-384 (2008).

5. I. Bigio and J. Mourant, "Ultraviolet and visible spectroscopies for tissue diagnostics: fluorescence spectroscopy and elastic-scattering spectroscopy," Phys Med Bio **42**, 803-814 (1997).

6. M. Chandra, J. Scheiman, D. Heidt, D. Simeone, B. McKenna, and M.-A. Mycek, "Probing pancreatic disease using tissue optical spectroscopy," J Biomed Opt **12**, 060501 (2007).

7. A. Dhar, K. S. Johnson, M. R. Novelli, S. G. Bown, I. J. Bigio, L. B. Lovat, and S. L. Bloom, "Elastic scattering spectroscopy for the diagnosis of colonic lesions: initial results of a novel optical biopsy technique," Gastrointest Endosc **63**, 257-261 (2006).

8. S. Andersson-Engels, C. Klinteberg, K. Svanberg, and S. Svanberg, "In vivo fluorescence imaging for tissue diagnostics," Phys Med Biol **42**, 815-824 (1997).

9. R. Richards-Kortum and E. Sevick-Muraca, "Quantitative optical spectroscopy for tissue diagnosis," Annu Rev Phys Chem **47**, 555-606 (1996).

10. M.-A. Mycek and B. W. Pogue, eds., *Handbook of Biomedical Fluorescence* (Marcel Dekker, Inc., New York, 2003).

11. J. R. Lakowicz, *Principles of Fluorescence Spectroscopy,* 2nd ed. (Kluwer Academic/Plenum, New York, 1999).

12. P. J. Tadrous, "Methods for imaging the structure and function of living tissues and cells: 2. fluorescence lifetime imaging," Journal of Pathology **191**, 229-234 (2000).

13. M. Chandra, K. Vishwanath, G. D. Fichter, E. Liao, S. J. Hollister, and M.-A. Mycek, "Noninvasive, quantitative fluorescence sensing in 3D tissues: an approach to in vivo molecular characterization of engineered tissue constructs," in *Biomedical Optics, Technical Digest (CD)*, (Optical Society of America, 2006), ME 59.

14. P. V. Butte, K. Vishwanath, B. K. Pikul, M.-A. Mycek, and L. Marcu, "Effects of tissue optical properties on time-resolved fluorescence measurements from brain tumors: an experimental and computational study," in *SPIE International Symposium on Biomedical Optics*, 2003), 600-608.

15. K. Vishwanath and M.-A. Mycek, "Time-resolved photon migration in bi-layered tissue models," Optics Express **13**, 7466-7482 (2005).

16. K. Vishwanath, B. W. Pogue, and M.-A. Mycek, "Quantitative fluorescence lifetime spectroscopy in turbid media: comparison of theoretical, experimental and computational methods," Phys Med Bio **47**, 3387-3405 (2002).

17. A. J. Welch, C. Gardner, R. Richards-Kortum, E. Chan, G. Criswell, J. Pfefer, and S. Warren, "Propagation of fluorescence light," Laser Surg Med **21**, 166-178 (1997).

18. C. Wang, C. Chen, C. Chiang, S. Young, S. Chow, and H. Chiang, "Partial least-squares discriminant analysis on autofluorescence spectra of oral carcinogenesis," Applied Spectroscopy **52**, 1190-1196 (1998).

19. N. Ramanujam, M. Follen Mitchell, A. Mahadevan, S. Thomsen, A. Malpica, T. Wright, N. Atkinson, and R. Richards-Kortum, "Development of a multivariate statistical algorithm to analyze human cervical tissue fluorescence spectra acquired in vivo," Laser Surg Med **19**, 46-62 (1996).

20. Z. F. Ge, K. T. Schomacker, and N. S. Nishioka, "Identification of colonic dysplasia and neoplasia by diffuse reflectance spectroscopy and pattern recognition techniques," Applied Spectroscopy **52**, 833-839 (1998).

21. G. M. Palmer, C. Zhu, T. M. Breslin, F. Xu, K. W. Gilchrist, and N. Ramanujam, "Comparison of Multiexcitation Fluroescence and Diffuse Reflectance Spectroscopy for the Diagnosis of Breast Cancer," IEEE Transactions on Biomedical Engineering **50**, 1233-1242 (2003).

22. S. K. Chang, Y. N. Mirabal, E. N. Atkinson, D. Cox, A. Malpica, M. Follen, and R. Richards-Kortum, "Combined reflectance and fluorescence spectroscopy for in vivo detection of cervical pre-cancer," J Biomed Opt **10**, 024031 (2005).

23. S. C. Chu, T. C. R. Hsiao, J. K. Lin, C. Y. Wang, and H. H. K. Chiang, "Comparison of the performance of linear multivariate analysis methods for normal and dyplasia tissues differentiation using autofluorescence spectroscopy," IEEE Transactions on Biomedical Engineering **53**, 2265-2273 (2006).

24. K. T. Schomacker, J. K. Frisoli, C. C. Compton, T. J. Flotte, J. M. Richter, N. S. Nishioka, and T. F. Deutsch, "Ultraviolet laser-induced fluorescence of colonic tissue: basic biology and diagnostic potential," Laser Surg Med **12**, 63-78 (1992).

25. K. T. Schomacker, J. K. Frisoli, C. C. Compton, T. J. Flotte, J. M. Richter, and T. F. Deutsch, "Ultraviolet laser-induced fluorescence of colonic polyps," Gastroenterology **102**, 1155-1160 (1992).

26. G. Zonios, L. T. Perelman, V. Backman, R. Manoharan, M. Fitzmaurice, J. Van Dam, and M. S. Feld, "Diffuse reflectance spectroscopy of human ademonatous colon polyps *in vivo*," Applied Optics **38**, 6628 (1999).

27. I. Georgakoudi and M. S. Feld, "The combined use of fluorescence, reflectance, and light-scattering spectroscopy for evaluating dysplasia in Barrett's esophagus," Gastrointestinal Endoscopy Clinics of North America **14**, 519-537 (2004).

28. I. J. Bigio, S. G. Brown, G. Briggs, C. Kelley, S. Lakhani, D. Picard, P. M. Ripley, I. G. Rose, and C. Saunders, "Diagnosis of breast cancer using elastic-scattering spectroscopy: preliminary clinical results," J Biomed Opt **5**, 221-228 (2000).

29. "Cancer Statistics 2009" (American Cancer Society, 2009), retrieved www.cancer.org.

30. W. Hartwig, L. Schneider, M. K. Diener, F. Bergmann, M. W. Buchler, and J. Werner, "Preoperative tissue diagnosis for tumours of the pancreas," British Journal of Surgery **96**, 5-20 (2009).

31. A. Fritscher-Ravens, L. Brand, W. T. Knofel, C. Bobrowski, T. Topalidis, F. Thonke, A. de Werth, and N. Soehendra, "Comparison of endoscopic ultrasound-guided fine needle aspiration for focal pancreatic lesions in patients with normal parenchyma and chronic pancreatitis," Am J Gastroenterol **97**, 2768-2775 (2002).

32. S. C. Abraham, R. E. Wilentz, C. J. Yeo, T. A. Sohn, J. L. Cameron, J. K. Boitnott, and R. H. Hruban, "Pancreaticoduodenectomy (Whipple Resections) in Patients Without Malignancy: Are They All `Chronic Pancreatitis'?," The American Journal of Surgical Pathology **27**, 110-120 (2003).

33. G. Zonios, L. T. Perelman, V. Backman, R. Manoharan, M. Fitzmaurice, J. V. Dam, and M. S. Feld, "Diffuse reflectance spectroscopy of human adenomatous colon polyps in vivo," Applied Optics **38**, 6628-6637 (1999).

34. S. K. Chang, N. Marin, M. Follen, and R. Richards-Kortum, "Model-based analysis of clinical fluorescence spectroscopy for in vivo detection of cervical intraepithelial dysplasia," J. Biomed. Opt. **11**, 024008 (2006).

35. M.-A. Mycek, K. Schomacker, and N. Nishioka, "Colonic polyp differentiation using time resolved autofluorescence spectroscopy," Gastrointestinal Endoscopy **48**, 390-394 (1998).

36. K. Vishwanath and M.-A. Mycek, "Do fluorescence decays remitted from tissues accurately reflect intrinsic fluorophore lifetimes?," Optics Letters **29**, 1512-1514 (2004).

37. P. A. Testoni, A. Mariani, B. Mangiavillano, P. G. Arcidiacono, S. Di Pietro, and E. Masci, "Intraductal optical coherence tomography for investigating main pancreatic duct strictures," Am J Gastroenterol **102**, 269-274 (2007).

38. P. A. Testoni, B. Mangiavillano, L. Albarello, P. G. Arcidiacono, A. Mariani, E. Masci, and C. Doglioni, "Optical coherence tomography to detect epithelial lesions of the main pancreatic duct: an Ex Vivo study," Am J Gastroenterol **100**, 2777-2783 (2005).

39. V. R. Kondepati, J. Zimmermann, M. Keese, J. Sturm, B. C. Manegold, and J. Backhaus, "Near-infrared fiber optic spectroscopy as a novel diagnostic tool for the detection of pancreatic cancer," J Biomed Opt **10**, 054016 (2005).

40. H. Subramanian, P. Pradhan, Y. Liu, I. R. Capoglu, J. D. Rogers, H. K. Roy, R. E. Brand, and V. Backman, "Partial-wave microscopic spectroscopy detects subwavelength refractive index fluctuations: an application to cancer diagnosis," Opt Lett **34**, 518-520 (2009).

41. V. Turzhitsky, Y. Liu, N. Hasabou, M. Goldberg, H. K. Roy, V. Backman, and R. Brand, "Investigating population risk factors of pancreatic cancer by evaluation of optical markers in the duodenal mucosa," Dis Markers **25**, 313-321 (2008).

42. Y. Liu, R. E. Brand, V. Turzhitsky, Y. L. Kim, H. K. Roy, N. Hasabou, C. Sturgis, D. Shah, C. Hall, and V. Backman, "Optical markers in duodenal mucosa predict the presence of pancreatic cancer," Clin Cancer Res **13**, 4392-4399 (2007).

43. K. Izumi, J. Song, and S. E. Feinberg, "Development of a tissue-engineered human oral mucosa: from the bench to the bed side," Cells Tissues Organs **176**, 134-152 (2004).

44. A. J. Welch and M. J. C. van-Gemert, *Optical-Thermal Response of Laser-Irradiated Tissue* (Plenum Press, New York, 1995).

45. J. A. Buckwalter and H. J. Mankin, "Instructional Course Lectures,The American Academy of Orthopaedic Surgeons - Articular Cartilage. Part I: Tissue Design and Chondrocyte-Matrix Interactions," Journal of Bone and Joint surgery (American Vol.) **79**, 600-611 (1997).

46. K. Izumi, H. Terashi, C. L. Marcelo, and S. E. Feinberg, "Development and characterization of a tissue-engineered human oral mucosa equivalent produced in a serum-free culture system," J Dent Res **79**, 798-805 (2000).

47. K. Badizadegan, V. Backman, C. W. Boone, C. P. Crum, R. R. Dasari, I. Georgakoudi, K. Keefe, K. Munger, S. M. Shapshay, E. E. Sheets, and M. S. Feld,

"Spectroscopic diagnosis and imaging of invisible pre-cancer," Faraday Discussions **126**, 265-279 (2004).

48. L. Lovat and S. Bown, "Elastic scattering spectroscopy for detection of dysplasia in Barrett's esophagus," Gastrointestinal Endoscopy Clinics of North America **14**, 507-517 (2004).

49. N. Ramanujam, M. F. Mitchell, A. Mahadevan, S. Warren, S. Thomsen, E. Silva, and R. Richards-Kortum, "In vivo diagnosis of cervical intraepithelial neoplasia using 337-nm-excited laser-induced fluorescence.," Proceedings of the National Academy of Science, USA **91**, 10193-10197 (1994).

50. M. G. Muller, T. A. Valdez, I. Georgakoudi, V. Backman, C. Fuentes, S. Kabani, N. Laver, Z. Wang, C. W. Boone, R. R. Dasari, S. M. Shapshay, and M. S. Feld, "Spectroscopic detection and evaluation of morphologic and biochemical changes in early human oral carcinoma," Cancer **97**, 1681-1692 (2003).

51. V. Backman, M. B. Wallace, L. T. Perelman, J. T. Arendt, R. Gurjar, M. G. Müller, Q. Zhang, G. Zonios, E. Kline, T. McGillican, S. Shapshay, T. Valdez, K. Badizadegan, J. M. Crawford, M. Fitzmaurice, S. Kabani, H. S. Levin, M. Seiler, R. R. R. R. Dasari, I. I. Itzkan, J. J. Van Dam, and M. S. M. S. Feld, "Detection of preinvasive cancer cells," Nature **406**, 35-36 (2000).

52. T. Vo-Dinh, ed., *Biomedical photonics handbook* (CRC Press, New York, 2003), Vol. 1.

53. S. Prahl, "Optical Absorption of Hemoglobin" (Oregon Medical Laser Center, 1999), retrieved http://omlc.ogi.edu/spectra/hemoglobin/index.html.

54. G. Zonios, R. Cothren, J. Arendt, J. Wu, J. Van Dam, J. Crawford, R. Manoharan, and M. Feld, "Morphological model of human colon tissue fluorescence," IEEE Transactions on Biomedical Engineering **43**, 113-122 (1996).

55. R. Drezek, K. Sokolov, U. Utzinger, I. Boiko, A. Malpica, M. Follen, and R. Richards-Kortum, "Understanding contributions of NADH and collagen to cervical tissue fluorescence spectra: Modeling, measurements, and implications," J Biomed Opt **6**, 385-396 (2001).

56. M. Chandra, K. Vishwanath, G. D. Fichter, E. Liao, S. J. Hollister, and M.-A. Mycek, "Quantitative molecular sensing in biological tissues: an approach to non-invasive optical characterization," Optics Express **14**, 6157-6171 (2006).

57. S. Chandrasekhar, *Radiative Transfer* (Dover, N.Y., 1960).

58. J. Wu, M. Feld, and R. Rava, "Analytical model for extracting intrinsic fluorescence in turbid media," Applied Optics **32**, 3585-3595 (1993).

59. M. S. Patterson and B. W. Pogue, "Mathematical model for time-resolved and frequency-domain fluorescence spectroscopy in biological tissues," Applied Optics **33**, 1963-1974 (1994).

60. W. M. Star, J. P. A. Marijnissen, and M. J. C. van-Gemert, "Light Dosimetry in optical phantoms in tissues: I. Multiple flux and transport theory," Phys. Med. Biol **33**, 437-454 (1988).

61. K. Vishwanath, "Computational modeling of time-resolved fluorescence transport in turbid media for noninvasive clinical diagnostics," (University of Michigan, Ann Arbor, 2005).

62. L. Wang, S. L. Jacques, and L. Zheng, "MCML - Monte Carlo modeling of photon transport in multi-layered tissues," Computer Methods and Programs in Biomedicine **47**, 131-146 (1995).

63. S. L. Jacques, "Time resolved propagation of ultrashort laser pulses within turbid tissue.," Applied Optics **28**, 2223-2229 (1989).

64. H. Zeng, C. MacAulay, D. I. McLean, and B. Palcic, "Reconstruction of in vivo skin auto fluorescence spectrum from microscopic properties by Monte-Carlo simulation," Journal of Photochemistry and Photobiology B **38**, 234-240 (1997).

65. B. Pogue and T. Hasan, "Fluorophore quantitation in tissue simulating media with confocal detection," IEEE Journal of Selected Topics in Quantum Electronics **2**, 959-964 (1996).

66. U. Utzinger and R. Richards-Kortum, "Fiber optic probes for biomedical optical spectroscopy," J Biomed Opt **8**, 121-147 (2003).

67. J. D. Pitts and M.-A. Mycek, "Design and development of a rapid acquisition laser-based fluorometer with simultaneous spectral and temporal resolution.," Review of Scientific Instruments **72**, 3061-3072 (2001).

68. N. Boens, W. Qin, N. Basaric, J. Hofkens, M. Ameloot, J. Pouget, J. P. Lefevre, B. Valeur, E. Gratton, M. vandeVen, N. D. Silva, Jr., Y. Engelborghs, K. Willaert, A. Sillen, G. Rumbles, D. Phillips, A. J. Visser, A. van Hoek, J. R. Lakowicz, H. Malak, I. Gryczynski, A. G. Szabo, D. T. Krajcarski, N. Tamai, and A. Miura, "Fluorescence lifetime standards for time and frequency domain fluorescence spectroscopy," Anal Chem **79**, 2137-2149 (2007).

69. M. Chandra, D. Heidt, D. Simeone, B. McKenna, J. Scheiman, and M.-A. Mycek, "Pancreatic tissue assessment using fluorescence and reflectance spectroscopy," in *Diagnostic Optical Spectroscopy in Biomedicine IV*, (Proceedings of SPIE, 2007), 66281R.

70. M. Chandra, J. Scheiman, D. Simeone, B. McKenna, J. Purdy, and M.-A. Mycek, "Spectral Areas and Ratios Classifier (SpARC) algorithm for pancreatic tissue classification using optical spectroscopy," (submitted for journal publication).

71. T. Crnogorac-Jurcevic, E. Efthimiou, P. Capelli, E. Blaveri, A. Baron, B. Terris, M. Jones, K. Tyson, C. Bassi, A. Scarpa, and N. R. Lemione, "Gene expression profiles of pancreatic cancer and stromal desmoplasia," Oncogene **20**(2001).

72. R. H. Wilson, M. Chandra, J. Scheiman, D. Simeone, B. McKenna, J. Purdy, and M.-A. Mycek, "Optical spectroscopy detects histological hallmarks of pancreatic cancer," Optics Express **17**, 17502-17516 (2009).

73. M. Chandra, W. R. LLoyd, R. H. Wilson, J. Scheiman, D. Simeone, J. Purdy, B. McKenna, and M.-A. Mycek, "Principal component analysis of tissue optical response: a framework for automated clinical detection of pancreatic cancer," (submitted for journal publication).

74. M. Chandra, R. H. Wilson, J. Scheiman, D. Simeone, B. McKenna, J. Purdy, and M.-A. Mycek, "Optical spectroscopy for clinical detection of pancreatic cancer," in *Clinical and Biomedical Spectroscopy*, (Proceedings of SPIE, 2009), 73681G.

75. W. R. Klecka, *Discriminant Analysis* (Sage Publications, Inc., 1980).

76. R. O. Duda, P. E. Hart, and D. G. Stork, *Pattern Classification,* 2nd ed. (Wiley-Interscience, 2000).

77. B. G. Tabachnik and L. S. Fidell, *Using Multivariate Statistics,* 5th ed. (Allyn & Bacon, 2006).

78. A. D. Joshi, J. A. Fessler, and R. A. Koeppe, "Improving PET receptor binding estimates from Logan plots using principal component analysis," Journal of Cerebral Blood Flow and Metabolism **28**, 852-865 (2008).

79. J. J. Faraway, *Linear models with R* (CRC Press, 2005).

80. M. Chandra, R. H. Wilson, W.-L. Lo, K. Vishwanath, K. Izumi, S. E. Feinberg, and M.-A. Mycek, "Sensing metabolic activity in tissue engineered constructs," in *Diagnostic Optical Spectroscopy in Biomedicine IV*, (Proceedings of SPIE, 2007), 66280B

81. D. Y. Churmakov, I. V. Meglinski, S. A. Piletsky, and D. A. Greenhalgh, "Analysis of skin tissues spatial fluorescence distrubution by the Monte Carlo simulation," Journal of Physics D: Applied Physics **36**, 1722-1728 (2003).

82. L. Lindqvist, B. Czochralska, and I. Grigorov, "Determination of the mechanism of photo-ionization of NADH in aqueous solution on laser excitation at 355 nm," Chemical Physics Letters **119**, 494-497 (1985).

83. S. A. Prahl, M. J. C. van Gemert, and A. J. Welch, "Determining the optical properties of turbid media by using the adding-doubling method," Applied Optics **32**, 559-568 (1993).

84. S. Prahl, "Inverse Adding-Doubling", retrieved http://omlc.ogi.edu/staff/prahl.html.

85. K. Vishwanath, "Computational modeling of time-resolved fluorescence transport in turbid media for non-invasive clinical diagnostics," Ph.D. Thesis (University of Michigan, Ann Arbor, 2005).

86. J. F. Beek, P. Blokland, P. Posthumus, M. Aalders, J. W. Pickering, H. J. C. M. Sterenborg, and M. J. C. van Gemert, "In vitro double-integrating-sphere optical properties of tissues between 630 and 1064 nm," Phys. Med. Biol. **42**, 2255-2261 (1997).

87. P. Å. Öberg, T. Sundqvist, and A. Johansson, "Asessment of cartilage thickness utilising reflectance spectroscopy," Medical & Biological Engineering & Computing **42**, 3-8 (2004).

88. L. Marcu, D. Cohen, J.-M. I. Maarek, and W. S. Grundfest, "Characterization of Type I, II, III, IV and V collagens by time-resolved laser-induced fluorescence spectroscopy," in *Optical Biopsy III*, (Proceedings of SPIE, 2000), 93-101.

89. C. B. Talbot, R. K. P. Benninger, P. de Beule, J. Requejo-Isidro, D. S. Elson, C. Dunsby, I. Munro, M. A. Neil, A. Sandison, N. Sofat, H. Nagase, P. M. W. French, and M. J. Lever, "Application of hyperspectral fluorescence lifetime imaging to tissue autofluorescence: arthritis," in *European Conference on Biomedical Optics*, (Proceedings of SPIE, 2005), 58620T.

90. K. Izumi, G. Takacs, H. Terashi, and S. E. Feinberg, "Ex vivo development of a composite human oral mucosal equivalent," J Oral Maxillofac Surg **57**, 571-577; discussion 577-578 (1999).

91. W.-L. Lo, K. Vishwanath, M. Chandra, M.-A. Mycek, K. Izumi, C. L. Marcelo, and S. E. Feinberg, "Cell size correlates with flavoprotien endogenous fluorescence in cultured human oral keratinocytes," in *The 9th International Conference on Optics Within Life Sciences*, 2006),

92. C. S. De Paiva, S. C. Pflugfelder, and D. Q. Li, "Cell size correlates with phenotype and proliferative capacity in human corneal epithelium"," Stem Cells **24**, 368-375 (2006).

93. R. Zhang, W. Verkruysse, B. Choi, J. A. Viator, B. Jung, L. O. Svaasand, G. Aguilar, and J. S. Nelson, "Determination of human skin optical properties from spectrophotometric measurements based on optimization by genetic algorithms," J Biomed Opt **10**, 024030 (2005).

94. Y. Wu and J. Y. Qu, "Combined depth- and time-resolved autofluorescence spectroscopy of epithelial tissue," Optics Letters **31**, 1833-1835 (2006).

95. K. Vishwanath, K. Izumi, M. Chandra, S. E. Feinberg, and M.-A. Mycek, "Quantitative, Noninvasive Optical Sensing in Tissue Engineered Oral Mucosal Constructs," in *Biomedical Optics 2006 Technical Digest (CD)*, (Optical Society of America, 2006), ME75.

96. Y. Wu, P. Xi, and J. Y. Qu, "Depth-resolved fluorescence spectroscopy of normal and dysplastic cervical tissue," Optics Express **13**, 382-388 (2005).

97. P. A. W. van den Berg, J. Widengren, M. A. Hink, R. Rigler, and A. J. W. G. Visser, "Fluorescence correlation spectroscopy of flavins and flavoenzymes: photochemical and photophysical aspect," Spectrochimica Acta Part A: Molecular and Biomolecular Spectroscopy **57**, 2135-2144 (2001).

98. T. J. Pfefer, A. Agrawal, and R. A. Drezek, "Oblique-incidence illumination and collection for depth-selective fluorescence spectroscopy," J Biomed Opt **10**, 044016 (2005).

99. R. H. Wilson, M. Chandra, W.-L. Lo, K. Vishwanath, K. Izumi, S. E. Feinberg, and M.-A. Mycek, "Simulated Fiber-Optic Interrogation of Autofluorescence from Superficial Layer of Tissue-Engineered Construct," in *OSA Frontiers in Optics,Technical Digest (CD)*, (Optical Society of America, 2008), FTuK6.

100. P. K. Urayama, W. Zhong, J. A. Beamish, F. K. Minn, R. D. Sloboda, K. H. Dragnev, E. Dmitrovsky, and M.-A. Mycek, "A UV-visible fluorescence lifetime imaging microscope for laser-based biological sensing with picosecond resolution," Applied Physics B: Lasers and Optics **76**, 483-496 (2003).

101. R. Drezek, C. Brookner, I. Pavlova, I. Boiko, A. Malpica, R. Lotan, M. Follen, and R. Richards-Kortum, "Autofluorescence microscopy of fresh cervical-tissue sections reveals alterations in tissue biochemistry with dysplasia," Photochem Photobiol **73**, 636-641 (2001).

102. M. Brewer, U. Utzinger, Y. Li, E. N. Atkinson, W. Satterfield, N. Auersperg, R. Richards-Kortum, M. Follen, and R. Bast, "Fluorescence spectroscopy as a biomaker in a cell culture and in a nonhuman primate model for ovarian cancer chemopreventive agents," J. Biomed. Optics **7**, 20-26 (2002).

103. Z. Zhang, D. Blessington, H. Li, T. M. Busch, J. Glickson, Q. Luo, B. Chance, and G. Zheng, "Redox ratio of mitochondria as an indicator for the response of photodynamic therapy," J Biomed Opt **9**, 772-778 (2004).

104. V. K. Ramanujan, J. H. Zhang, E. Biener, and B. Herman, "Multiphoton fluorescence lifetime contrast in deep tissue imaging: prospects in redox imaging and disease diagnosis," J Biomed Opt **10**, 051407 (2005).

105. N. D. Kirkpatrick, W. R. Brands, C. Zou, M. A. Brewer, and U. Utzinger, "Intrinsic fluorescence biomarkers in cells treated with chemopreventive drugs," in *Imaging, Manipulation, and Analysis of Biomolecules and Cells: Fundamentals and Applications III,*, (Proceedings of SPIE, 2005), 255-262.

106. J. M. Levitt, A. Baldwin, A. Papadakis, S. Puri, J. Xylas, K. Munger, and I. Georgakoudi, "Intrinsic fluorescence and redox changes associated with apoptosis of primary human epithelial cells," J Biomed Opt **11**, 064012 (2006).

107. Y. Wu and J. Y. Qu, "Autofluorescence spectroscopy of epithelial tissues," J Biomed Opt **11**, 054023 (2006).

108. J. M. Reyes, S. Fermanian, F. Yang, S. Y. Zhou, S. Herretes, D. B. Murphy, J. H. Elisseeff, and R. S. Chuck, "Metabolic changes in mesenchymal stem cells in osteogenic medium measured by autofluorescence spectroscopy," Stem Cells **24**, 1213-1217 (2006).

109. M. Ranji, S. Kanemoto, M. Matsubara, M. A. Grosso, J. H. Gorman, 3rd, R. C. Gorman, D. L. Jaggard, and B. Chance, "Fluorescence spectroscopy and imaging of myocardial apoptosis," J Biomed Opt **11**, 064036 (2006).

110. L. M. Tiede, S. M. Rocha-Sanchez, R. Hallworth, M. G. Nichols, and K. Beisel, "Determination of hair cell metabolic state in isolated cochlear preparations by two-photon microscopy," J Biomed Opt **12**, 021004 (2007).

111. A. Mayevsky and B. Chance, "Oxidation-reduction states of NADH in vivo: From animals to clinical use," Mitochondrion (2007).

112. L. Pfeifer, K. Stein, U. Fink, A. Welker, B. Wetzl, P. Bastian, and O. Wolfbeis, "Improved Routine Bio-Medical and Bio-Analytical Online Fluorescence Measurements Using Fluorescence Lifetime Resolution," Journal of Fluorescence **15**, 423-432 (2005).

113. L. Pfeifer, I. Gruenwald, A. Welker, R. M. Stahn, K. Stein, and A. Rex, "Fluorimetric characterisation of metabolic activity of ex vivo perfused pig hearts," Biomed Tech (Berl) **52**, 193-199 (2007).

114. J. Pitts, R. Sloboda, K. Dragnev, E. Dmitrovsky, and M.-A. Mycek, "Autofluorescence characteristics of immortalized and carcinogen-transformed human bronchial epithelial cells.," J Biomed Opt **6**, 31-40 (2001).

115. A. Shiino, M. Haida, B. Beauvoit, and B. Chance, "Three-dimensional redox image of the normal gerbil brain," Neuroscience **91**, 1581-1585 (1999).

116. S. Huang, A. A. Heikal, and W. W. Webb, "Two-photon fluorescence spectroscopy and microscopy of NAD(P)H and flavoprotein," Biophys J **82**, 2811-2825 (2002).

117. M. Mokry, P. Gal, B. Vidinsky, J. Kusnir, K. Dubayova, S. Mozes, and J. Sabo, "In vivo monitoring the changes of interstitial pH and FAD/NADH ratio by fluorescence spectroscopy in healing skin wounds," Photochem Photobiol **82**, 793-797 (2006).